INSTABILITY OF HORIZONTALLY AND VERTICALLY SHEARED PARALLEL FLOW

by Mark A. Ringerud, Duane E. Stevens and Paul E. Ciesielski

Colorado State University

DEPARTMENT OF ATMOSPHERIC SCIENCE

PAPER NO. 445

INSTABILITY OF HORIZONTALLY AND VERTICALLY SHEARED PARALLEL FLOW

by

Mark A. Ringerud, Duane E. Stevens
and Paul E. Ciesielski

Department of Atmospheric Science
Colorado State University
Fort Collins, CO 80523

This research was supported by the National Science Foundation
under Grants ATM–8305759 and ATM–8352205

Atmospheric Science Paper No. 445

June 1989

Abstract

This study examines the effects of various windshears on the perturbation growths within inertially unstable regions. A primary focus is determining what type of instability is preferred, symmetric or asymmetric, through the development of a two-dimensional model using the primitive equations and a jet with horizontally and vertically sheared flow.

A necessary condition for inertial instability is when the basic state potential vorticity, $f\bar{P} < 0$. The potential vorticity can be viewed as having two influences, that due to the horizontal wind shear and vertical shear. With this in mind, I examine the relationship between the shears in inertial instability.

This study extends previous results where the basic state contained only horizontal shear, $\bar{u}(y)$. These results, obtained with a shallow water model, showed that asymmetric modes had larger growth rates than symmetric modes. By examining various jet profiles which contained both horizontal and vertical shear, the results in this more general case (i.e., $\bar{u}(y, z)$ again revealed that asymmetric instabilities are preferred.

ACKNOWLEDGEMENTS

We would like to thank Scott Fulton, Hung-Chi Kuo, Frank Crum and Maria Flatau for their valuable comments, and Gail Cordova who patiently worked through many drafts in preparing this manuscript.

This work was supported by NSF Grant No. ATM-8305759 and by the Presidential Young Investigator Award (NSF Grant No. ATM-8352205) to D. Stevens. Acknowledgement is made to the National Center for Atmospheric Research, which is sponsored by the National Science Foundation for a substantial portion of the computing resources used in this research.

TABLE OF CONTENTS

Chapter 1

INTRODUCTION

Atmospheric science is a complex web of possibilities and probabilities. We simplify and analyze bits and pieces of it to produce understandings of the overall picture. One of these "pieces" which poses significant probabilities to the dynamics of the atmosphere is the study of instabilities. In instability studies, the stability of a flow configuration is investigated to determine whether small-amplitude perturbations can spontaneously grow, gaining energy from the mean flow.

Charney (1973) documents and classifies many types of hydrodynamic instability with applicability to geophysical fluids. Barotropic and baroclinic instabilities are important types of non-axisymmetric (three-dimensional) instabilities while axisymmetric (two-dimensional) disturbances result from inertial instability of a symmetric flow. Boyd and Christidis (1982) and Dunkerton (1982) have discussed inertial instability as a mechanism for forcing nonsymmetric disturbances as well.

Stevens and Ciesielski (1986; hereafter referred to as SC) investigated the preferred instabilities for horizontally sheared flow away from the equator. For their wind profiles, they found that inertial instability has a significantly greater growth rate than barotropic instability. They proposed that their results could be applied qualitatively to more general flows – e.g. where the mean flow varies in the vertical and horizontal directions. This study follows their lead in this investigation of inertial instability.

In the case of a basic state with horizontal and/or vertical shear $[\overline{u}(y,p)]$, the basic state potential vorticity, $\overline{P}$, replaces the absolute vorticity in determining the instability criterion; cf. Stevens (1983). A necessary condition for inertial instability is then $f\overline{P} < 0$ somewhere in the fluid where $f\overline{P}$ is defined as follows for geostrophic flow

$$f\overline{P} = \overline{\theta}\overline{\rho}\left(f\frac{\partial \overline{u}}{\partial p}\right)^2\left[\frac{\overline{\eta}}{f}Ri - 1\right] \tag{1.1}$$

where

$$Ri \equiv \frac{N^2}{\left(\overline{\rho}g\frac{\partial \overline{u}}{\partial p}\right)^2} \tag{1.2}$$

Ri is the Richardson number, f is the Coriolis parameter, $\overline{\eta}$ is the absolute vorticity and $\overline{\theta}$ and $\overline{\rho}$ are the basic state potential temperature and density, respectively.

Stone (1966, 1970), found that symmetric disturbances are preferred when the inertial instability is derived solely from the vertical shear $\left(\frac{\partial \overline{u}}{\partial p}\right)$ in the mean flow, $\left(\text{i.e. } \frac{\partial \overline{u}}{\partial y} = 0\right)$. Since Stone's work, inertial instability has often been referred to as symmetric instability. This label implies that the most unstable mode of instability should occur for symmetric perturbations, i.e., for perturbations that display no structure in the direction of the basic state flow. With this assumption, the analysis of a given problem can often be simplified (Emanuel, 1979; Dunkerton, 1981).

Other studies have ignored vertical shear $\left(\frac{\partial \overline{u}}{\partial p} = 0\right)$ and used the condition for inertial instability from the horizontal shear $f\overline{\eta}$ <0. Asymmetric modes of instability may be preferred, as shown by Boyd and Christidis (1982) and Dunkerton (1983), in a basic state zonal flow near the equator with linear latitudinal shear. As an extension of these works SC investigated both symmetric and asymmetric instabilities for horizontally sheared flow away from the equator. Their results show that at finite but often rather small vertical scale (e.g., a few hundred meters), asymmetric ($s \neq 0$) instabilities are preferred over the symmetric instability. These instabilities could be readily excited in nature when dissipation stabilizes the symmetric modes of smallest vertical scale.

The results of SC's analyses contrast significantly with those of Stone. In this study, we hope to understand the connection between these works by developing a model which can accommodate both horizontal and vertical shear in the mean flow. The purpose of this paper is to extend these recent studies to investigate the preferred instabilities when a basic state zonal flow has horizontal shear, but also when the basic state zonal flow has only vertical shear and when it has vertical and horizontal shear together.

The approach we take to this problem is to first solve a relatively simple model and then, systematically advance to a primitive equation model which accomodates two-dimensional shear of a zonal flow. In Chapter 2 we develop a linearized, shallow water model with $\overline{u}(y)$ similar to SC. In their study, they used a finite difference discretization and solved their model as an eigenvalue problem to obtain the growth rates of the unstable modes. In our approach we use a time integration scheme and a spectral discretization with Chebyshev polynomials as the basis function. Time integration is used since the resolution needed eventually to represent two-dimensional shear makes the matrix eigenvalue approach impractical since the matrices would get too large. Spectral methods offer more accurate solutions with far fewer degrees of freedom than do finite difference methods (Fulton, 1984). Chapter 3 proceeds with the development of the two-dimensional model using the linearized primitive equations.

In Chapter 4.1 we show results from the primitive equation model for the case where the basic state zonal flow has only horizontal shear, $\overline{u} = \overline{u}(y)$, the results are compared with SC's work. Next we show model results for the case with a zonal flow having only vertical shear, (i.e., $\overline{u} = \overline{u}(z)$), in Chapter 4.2. These results should reduce to those of Stone (1966, 1970) and Nehrkorn (1986). Then in Chapter 4.3 we set the zonally averaged jet to have variable vertical and horizontal wind shear, using parameters from an actual physical case study of Ciesielski *et al.* (1988). Chapter 5 summarizes the principal conclusions of this study.

Chapter 2

THE SHALLOW WATER EQUATION MODEL DEVELOPMENT

The development of the primitive equation model is an involved task. In this section we develop a simple model as a step towards the larger primitive equation model. This allows us to test the basic algorithm we want to use in the primitive equation model including testing of the spectral transforms and the time integration scheme. As a check on the model, we compare our results with recent studies.

We use the shallow water equations where the basic state zonal flow is one-dimensional, $\overline{u}(y)$. As we will see later, this simple model will be the basis for the primitive equation model, since basically we need only add the vertical coordinate to the equations along with the hydrostatic and thermodynamic equations to get the primitive equations.

2.1 The numerical model

2.1.1 Basic equations

The derivation of the model begins with the nonlinear inviscid shallow water equation set (Haltiner and Williams, 1980) on an f-plane.

$$\frac{\partial u}{\partial t} + u\frac{\partial u}{\partial x} + v\frac{\partial u}{\partial y} - fv + \frac{\partial \phi}{\partial x} = 0 \tag{2.1}$$

$$\frac{\partial v}{\partial t} + u\frac{\partial v}{\partial x} + v\frac{\partial v}{\partial y} + fu + \frac{\partial \phi}{\partial y} = 0 \tag{2.2}$$

$$\phi\left(\frac{\partial u}{\partial x} + \frac{\partial v}{\partial y}\right) = -\frac{d\phi}{dt} = -\left(\frac{\partial \phi}{\partial t} + u\frac{\partial h}{\partial x} + v\frac{\partial h}{\partial y}\right) \tag{2.3}$$

where $\phi = gh$. These equations are the momentum and continuity equations, respectively. The dependent variables are u, v, ϕ, while x, y, t are the independent variables.

Each dependent variable χ is separated into a temporally and zonally averaged part $\overline{\chi}(y)$ and a perturbation quantity $\chi'(x, y, t)$. Substituting this form of the variables into the nonlinear equations and linearizing the equations, neglecting the nonlinear products of perturbation quantities, produces a linear equation set for the perturbations.

$$\frac{\partial u'}{\partial t} + \overline{u}\frac{\partial u'}{\partial x} + v'\frac{d\overline{u}}{dy} - fv' = -\frac{\partial \phi'}{\partial x} \tag{2.4}$$

$$\frac{\partial v'}{\partial t} + \overline{u}\frac{\partial v'}{\partial x} + fu' = -\frac{\partial \phi'}{\partial y} \tag{2.5}$$

$$\frac{\partial \phi'}{\partial t} + \overline{u}\frac{\partial \phi'}{\partial x} + \phi_o\left(\frac{\partial u'}{\partial x} + \frac{\partial v'}{\partial y}\right) = 0 \tag{2.6}$$

the symbols have the following definitions:

u', v'	zonal and meridional velocity perturbations
ϕ'	geopotential perturbation
f	Coriolis parameter, assumed f=constant (f-plane)
$\bar{u}$	basic state zonal jet
ϕ_o	geopotential basic state ($\equiv gH$ is constant)

The x-axis in our model is set to be in the direction of the basic state component of flow since on an f-plane it is arbitrary. We use a zonal jet for this work so the mean wind field is included only through the zonal component $\overline{u}$; $\overline{v}$ is assumed to be zero.

2.1.2 Space discretization: Spectral method

The coefficients within the set of equations are independent of x; therefore we fourier transform the equations in the x direction. Using fourier expansion, any perturbation quantity can be written as

$$\chi'(x, y, t) = Re\left(\sum_{k=0}^{\infty} \chi'_k(y, t)e^{ikx}\right) \tag{2.7}$$

where k is the assumed zonal wavenumber ($k = 2\pi/\mathrm{L}_x$ where L_x = zonal wavelength). The perturbation coefficients, χ'_k, are all considered complex.

Applying the zonal transforms to the linearized shallow water equation set we get:

$$\frac{\partial u'_k}{\partial t} + \overline{u} iku'_k + \frac{d\overline{u}}{dy} v'_k - f v'_k = -ik\phi'_k \tag{2.8}$$

$$\frac{\partial v'_k}{\partial t} + \overline{u} ikv'_k + f u'_k = -\frac{\partial \phi'_k}{\partial y} \tag{2.9}$$

$$\frac{\partial \phi'_k}{\partial t} + \overline{u} ik\phi'_k + \phi_o \left(iku'_k + \frac{\partial v'_k}{\partial y} \right) = 0 \tag{2.10}$$

The model equations are applied within a limited channel, 1665 kilometers wide (approximately 15° latitude). We assume a strong mid-latitude westerly jet. The anti-cyclonic side (the southern side) of the jet is the area of negative absolute vorticity and we expect the disturbance to grow in that region locally.

The next step is to transform this set into spectral space in the meridional direction (i.e., y) using Chebyshev polynomials as the basis functions. This is where this model differs from models using finite differencing. Spectral methods offer more accurate solutions with far fewer degrees of freedom than do finite difference methods (Fulton,1984). However, the use of these global basis functions does introduce additional complexity.

The Chebyshev transform pair is:

$$\chi'_k(y,t) = \sum_{m=0}^{N} \hat{\chi}_{km}(t) G_m(y) \tag{2.11}$$

$$\hat{\chi}_{km}(t) = \langle \chi'_k, G_m \rangle \tag{2.12}$$

where $\hat{\chi}_{km}$ is the spectral coefficient and $G_m(y)$ is the mth Chebyshev polynomial. The Chebyshev inner product, <>, is defined in Appendix A. Chebyshev is used since the rate of convergence of the expansions depends only on the smoothness of the function being expanded and not on its behavior at the boundaries. Also, Chebyshev series can be evaluated very efficiently. One disadvantage to using Chebyshev methods is that the time step is inversely proportional to the square of the number of modes where finite difference schemes are only inversely proportional to the number of modes.

Applying this meridional transform to our set of equations, we get:

$$\frac{d\hat{u}_{km}}{dt} - f\hat{v}_{km} + ik\hat{\phi}_{km} = -(\overline{u}iku'_k)_m - \left(\frac{d\overline{u}}{dy}v'_k\right)_m \tag{2.13}$$

$$\frac{d\hat{v}_{km}}{dt} + f\hat{u}_{km} + \frac{\partial}{\partial y}\hat{\phi}_{km} = -(\overline{u}ikv'_k)_m \tag{2.14}$$

$$\frac{d\hat{\phi}_{km}}{dt} + \phi_o\left(ik\hat{u}_{km} + \frac{\partial}{\partial y}\hat{v}_{km}\right) = -(\overline{u}ik\phi'_k)_m \tag{2.15}$$

The terms on the right hand side of the prognostic set of equations look similar to nonlinear terms of a nonlinear set of equations since the coefficients are a function of $y, [\overline{u}(y)]$. So in programming, we treat them like nonlinear terms and calculate them before entering spectral space. The rest of the terms are calculated in spectral space.

See Appendix A for a more detailed look at the Chebyshev spectral transform.

2.1.3 Time discretization: Time integration

Another difference with this model compared to many others is in our use of time integration versus the use of matrix eigenvalue methods. The resolution needed eventually to represent two-dimensional shear would make using the matrix eigenvalue approach non-practical since the matrices would get too large; even though eigenvalue methods are more computationally efficient. A disadvantage to the time integration scheme is that we only get the most unstable mode whereas the eigenvalue method finds all unstable modes.

There are many different time difference schemes to utilize. For various reasons one may be preferred to the next: accuracy, simplicity, stability, storage, number of steps, efficiency. For example the leapfrog scheme uses the least computer time but has a computational mode (truncation error) that usually arises. A method often used is the leapfrog along with an occasional backward scheme to eliminate the computational mode and a trapezoidal scheme to suppress noise (Young,1968).

We have chosen the Runge-Kutta fourth order method (Conti, 1965) which uses a combination of these:

$$\tilde{u}^{(n+\frac{1}{2})} = u^{(n)} + \frac{1}{2}\Delta t f^{(n)} \quad \text{; forward halfstep} \tag{2.16}$$

$$\hat{u}^{(n+\frac{1}{2})} = u^{(n)} + \frac{1}{2}\Delta t \tilde{f}^{(n+\frac{1}{2})} \quad \text{; backward halfstep} \tag{2.17}$$

$$\overset{*}{u}^{(n+1)} = u^{(n)} + \Delta t \hat{f}^{(n+\frac{1}{2})} \quad \text{; forward leapfrog} \tag{2.18}$$

$$u^{(n+1)} = u^{(n)} + \Delta t \cdot \frac{1}{6}\left[f^{(n)} + 2\tilde{f}^{(n+\frac{1}{2})} + 2\hat{f}^{(n+\frac{1}{2})} + \overset{*}{f}^{(n+1)}\right] \tag{2.19}$$

We originally used the Adams-Bashforth second order method with our shallow water model, but as the number of modes increased in spectral space, the time step needed for computational stability became relatively small making the model inefficient and impractical. The time step, Δt, is inversely proportional to the square of the number of spectral space modes used. Also, Δt is proportional to the number of steps in a time scheme (i.e., 4 for fourth order, 2 for second order schemes), so we found that using the Runge-Kutta method allowed larger time steps when using more modes than did the Adams- Bashforth method. It also showed more accurate results (Young, 1968). In determining the optimal time step, we found that due to the CFL criterion that Δt not only depends on the domain size, Δy, and wave speed, c, but also upon the number of modes used, N, and the number of computations, A, within the time difference scheme. This CFL criterion is given as

$$\frac{c\Delta t}{\Delta y}\frac{N^2}{A} \leq B \tag{2.20}$$

where B is the stability condition for the time difference scheme.

2.1.4 Boundary conditions

It is assumed that there are no fluxes of any quantity across the horizontal boundaries of the model. Therefore, on the lateral borders the meridional wind perturbations, v', are constrained to be zero. In the Chebyshev-Tau method we can apply this condition to the spectral coefficients of v'. The above equation for the Chebyshev transform is used by setting $v' = 0$ at the boundaries equal to the summation of the spectral coefficients. Then combining these two relationships we get an equation for both the Nth v' spectral coefficient and the $(N-1)th$ one with respect to the other coefficients. So the procedure is to use the prognostic equations to calculate new v' spectral coefficients and then calculate the N and $(N-1)$ coefficients to set our boundary conditions.

2.1.5 Basic state

We apply our model with basic state flows consisting of jet profiles given by

$$\bar{u}(\theta) = u_o \mathrm{sech}^2\left(\frac{\theta - \theta_o}{\theta_1}\right) \tag{2.21}$$

In this mean flow, known as the Bickley jet, u_o gives the magnitude of the jet, θ_o is the central latitude of the jet, and θ_1 is the jet halfwidth. As in SC we examine the instabilities of a midlatitude westerly jet centered at 45°N.

2.1.6 Initialization

For the purpose of testing, we have set up three possible initial conditions. One is an initial condition with simple sine waves for the real parts of the momentum variables, u' and v'. This is to test model runs with an analytical solution. The second one is with gaussian curves set up for the real parts of u' and v'. This corresponds to trying to match closely the expected solutions thereby reducing the model run time to achieve the most unstable mode. The third one is used to insure no biased conditions initially, we initialize the perturbation momentum fields as white noise (random values between 0 and 1 ms^{-1}) and let the unstable modes grow out of that. The perturbation variables are calculated from the prognostic equations.

2.1.7 Modeling procedure

For each value of ϕ_o in (2.10), a sufficient number of model runs of varying zonal wavenumber are made to define the wavenumber at which the growth rate of total energy is greatest. Beginning with an initially small ($0.0 < |u'|, |v'| < 1.0\ \mathrm{ms}^{-1}$) perturbation, the model is run until the solution converges to a single normal mode.

This mode is easy to calculate with our model. Plotting $ln(TE)$ versus time, where TE is a quantity related to the total energy over the whole domain, we will see in time the function increasing linearly when it converges to a single mode. The slope of this line will give $2\sigma_i$ (σ_i = maximum growth rate). This is because the variables can be written as $u' = \sum_j A_j e^{-i\sigma_j t}$ where A_j is a constant coefficient for each mode and σ_j is complex. The next section, 2.2, contains the details of this procedure.

2.2 Analysis Techniques

In this section we describe the techniques used to analyze our model results. The purpose is to have these procedures ready and tested for use in our primitive equation model which has a basic state flow with two-dimensional wind shear.

We want to set up the basic state so that the criteria for inertial instability is met. In the case where we have a basic state jet with horizontal and vertical wind shear, we need the potential vorticity, equation (1.1) to be negative. Our first case though is with the shallow water equations, the basic state jet has only horizontal wind shear.

Therefore (1.1) may be simplified, reducing the criteria for inertial instability to when the absolute vorticity is negative. As seen from the equation for absolute vorticity, the basic state zonal flow, $\bar{u}$, is the factor we adjust to create the needed absolute vorticity.

When the condition for inertial instability is present in a region of the atmosphere there are modes which are stable and unstable. All these modes that exist are essentially competing against one another. However many modes there are though, there will be one that is the most unstable mode in this region. This mode will have the fastest growth rate of all the modes. As time proceeds, this mode will come to dominate over all the other modes. This of course depends on the region remaining inertially unstable during this time and depending on the time the most unstable mode overcomes the other modes, the question of how physically realistic that case is comes up. Any type of instability is its own worst enemy since the atmospheric condition it creates tends to destroy the same. But the time it takes our model is not of major concern since the main phenomena we are looking for are the growth rates for the most unstable modes.

In particular, we want to look at how the growth rates, σ_i, vary with the zonal wavenumber, s. This will allow us to study the question of symmetric versus asymmetric modes when the basic state jet includes horizontal and vertical wind shear. And at this time in our model development this will allow us to run our test comparisons for our shallow water equations model with the work of SC. The model they set up with the shallow water equations used the eigenvalue approach, this is a major difference compared to our time integration method. We chose time integration because the storage requirements will be less than the eigenvalue matrix approach when we advance to the horizontal and vertical zonal jet (primitive equations). But a disadvantage is that in our approach we are only able to calculate the most unstable mode, while with the eigenvalue method, all the modes are available. So with their results, the most unstable mode can be picked out while we need a more involved method to find the most unstable mode.

In a straightforward manner, we can calculate a quantity (TE) related to the total energy of our system using the concept that the total energy is conserved in a closed system, we can calculate the growth rate of the most unstable mode. Evaluating TE will give us a domain-integrated means of determining growth rate.

We write the perturbation variables in the solution form (normal mode form):

$$u' = A \; e^{-i\sigma t} \tag{2.22}$$

where A is a constant coefficient and σ is the complex frequency. Sigma can be written as

$$\sigma = \sigma_r + i\sigma_i \tag{2.23}$$

where σ_r is the oscillatory part and σ_i is the growth rate.

It follows that TE can then be written in solution form:

$$TE = Re\{Be^{-2i\sigma t}\} \tag{2.24}$$

where B is a constant real coefficient and the factor of 2 comes from the fact that energy is quadratic in the predicted variables u', v', and ϕ'. Then

$$TE = B \ e^{2\sigma_i t} \tag{2.25}$$

Now we take the real part of the natural log of this solution to get:

$$\ell n(TE) = \ell nB + 2\sigma_i t \tag{2.26}$$

This equation is now a linear equation with slope $2\sigma_i$ and y-intercept, ℓnB. By plotting $\ell n(TE)$ versus time, t, we can calculate the slope which gives us the growth rate, σ_i. The y-intercept, ℓnB, will only shift the function, having no effect on the slope.

Total energy is calculated by adding the kinetic energy and the available potential energy over the entire domain. In the shallow water equation set, the momentum fields u and v make up the kinetic energy and the geopotential, ϕ, makes up the available potential energy.

To calculate TE we start with the linearized shallow water equation set. Multiply (2.4) by u', (2.5) by v' and (2.6) by $\frac{\phi'}{\phi_o}$ and add all three. This gives us a relation

$$\frac{\partial}{\partial t}\left(\frac{u'^2}{2} + \frac{v'^2}{2} + \frac{\phi'^2}{2\phi_o}\right) = ... \tag{2.27}$$

Integrating over y, we obain an expression for TE:

$$\frac{\partial}{\partial t}(TE) = \frac{\partial}{\partial t} Re\left[\int \left(\frac{u'^2}{2} + \frac{v'^2}{2} + \frac{\phi'^2}{2\phi_o}\right) dy\right] = ... \tag{2.28}$$

this gives us the time rate of change of the total energy.

We are only interested in the relative magnitude of the total energy since the slope of the curve of $\ell n(TE)$ versus time is what we need not its absolute magnitude. So we use only the term shown above in the energetics equation which is proportional to the total energy of our system.

Now to set this up to be programmed, we fourier transform this equation using

$$u = \sum_{\ell=-J}^{J} \hat{u}_\ell(t) e^{i\ell y} \tag{2.29}$$

and

$$u^2 = \sum_{m=-J}^{J} \sum_{\ell=-J}^{J} \hat{u}_\ell \hat{u}_m e^{iy(\ell+m)} \tag{2.30}$$

since u^2 is always real, the only time this equation is real is when $\ell = -m$ and $\hat{u}_{-m} = \hat{u}^*_m$, ($u^*$ is the complex conjugate) then

$$TE = \pi \sum_{m=0}^{J} \left(u_m u^*_m + v_m v^*_m + \frac{\phi_m \phi^*_m}{\phi_o} \right) \tag{2.31}$$

where m is each point in the physical domain. In our system of collocated points, we transform our perturbation values to evenly spaced points to get a meridional average.

We also can calculate the value of the phase speed, c_r. By taking the real part of equation (2.22), we get an oscillatory part, σ_r, which is the phase of the perturbation variable:

$$\text{phase} = -\sigma_r t \tag{2.32}$$

and then the phase speed is, $c_r = \frac{\sigma_r}{k}$.

The actual model procedure uses the above equation for total energy. At given time intervals we calculate and store the value of TE. Then we plot the $\ell n(TE)$ versus time and the resulting plot shows us what we expect. The many modes in our system are initially affecting the overall growth rate for a time as we see in Fig. 2.1a, causing the TE plot to fluctuate. But after a given time the largest growth rates associated with the most unstable modes begin to cause the TE to increase exponentially as dictated from (2.25) until the most unstable mode finally dominates (the TE line straightens out). Also, by plotting the phase of u' (at a point within the area growing with the most unstable mode) versus time, as seen in Fig. 2.1b, the slope of that line gives us the phase speeds.

2.3 Numercial results

In this section we present results from our shallow water equation model. In particular, we investigate the horizontal and vertical space scales of the instabilities, as well as their dynamical character and structure. To reiterate the purpose of this model, it is the

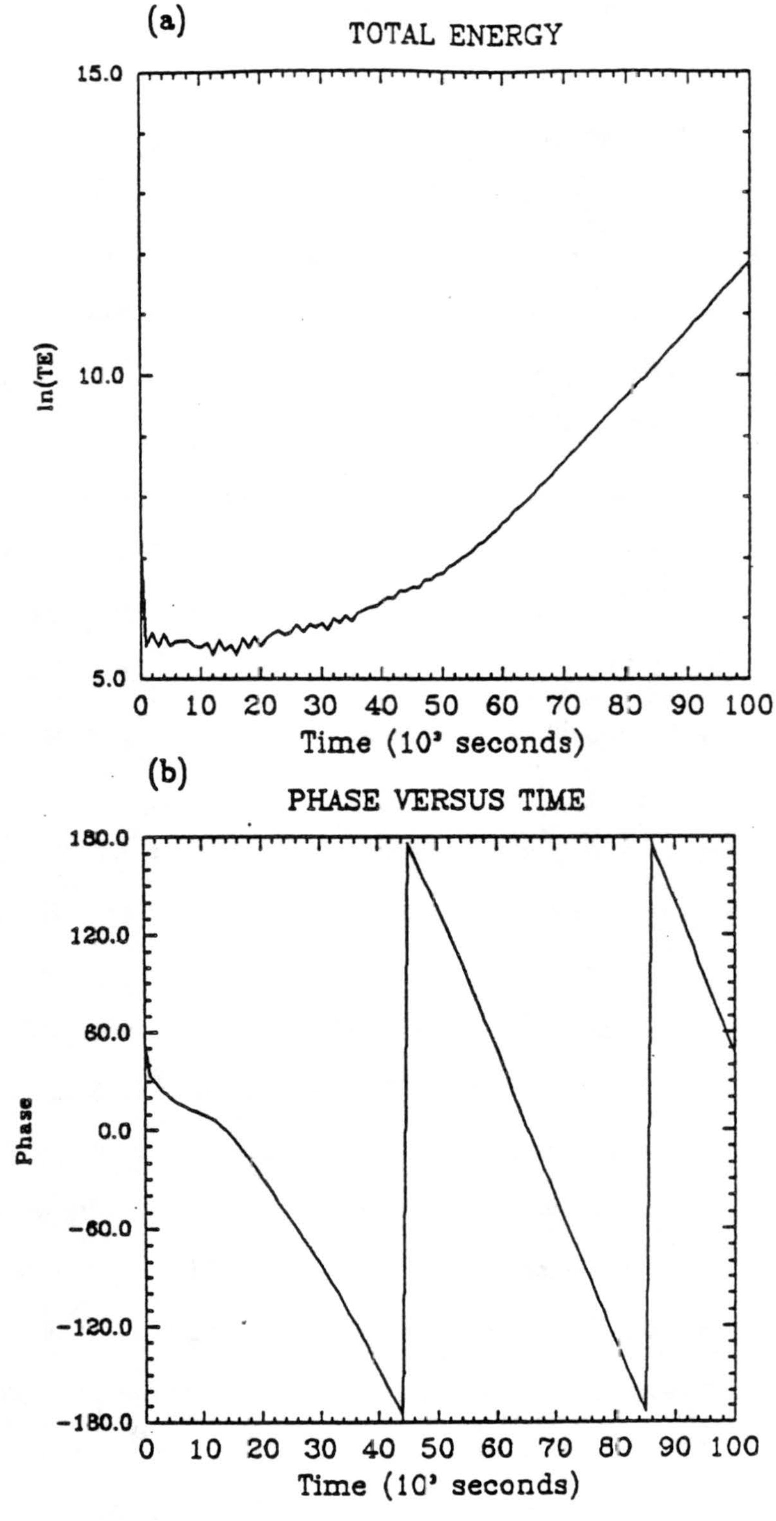

Figure 2.1: (a) Growth of log of total energy from $t = 0$ to 100,000 seconds, for shallow water equations. Meridional average of total energy. For $s = 6$, $h = 10$ m. (b) Phase of u' at 42.5°N from $t = 0$ to 100,000 seconds. For $s = 6$, $h = 10$ m.

core with the set of three dependent variables of what will become the primitive equation model. In addition it gives us a simplified equation set to test the various modeling procedures we want to use later. The algorithm to solve these three dependent variables lay the path equations needed to solve the three prognostic variables. And finally to verify that it is working properly, we compare its results to those of SC.

In the initial runs of the shallow water model we worked out the algorithm needed to utilize the Chebyshev spectral transform routines, the time difference scheme and the size of the time step.

To enable the use of the Chebyshev-Tau spectral transform routines, we need the physical perturbation variables to be designated at collocated points. To address the possible problem of aliasing, we need 3/2 more physical points than spectral coefficients. And for the purpose of making the output more readable and easier to plot, we transform the output data from spectral coefficients to evenly spaced physical points where we'll use 60 points for the domain of 15° latitude.

We will use $N = 16$ spectral coefficients, and $M = 24$ collocated physical points since we found that the results changed little when using $N = 32$ and the time step we can use for $N = 16$ is much larger.

Our shallow water model is now used to study the instabilities for the basic state examined by SC where u_o is 75 m/s and it is centered at 45°N is the jet profile shown in Fig. 2.2a. The condition for inertial instability can be seen in Fig. 2.2b which shows the profile of the absolute vorticity ($\bar{\eta}$) associated with this jet. We assume f-plane dynamics so where $\bar{\eta} < 0$ is the region that is inertially unstable. For this basic state profile, the computed growth rates (σ_i) and phase speeds (c_r) as a function of zonal wavenumber (s) are shown in Figs. 2.3a and 2.3b, respectively, for several values of equivalent depth (h). The growth rate curves have their maximum at different values of s as h varies. These results both confirm SC's work shown in Fig. 2.4 and give us confidence that our model is working correctly. The zonally symmetric mode ($s = 0$) is most unstable only at the smallest vertical scales ($h =$ 1m) we examined; even in this case, the growth rate decreases relatively slowly as s increases. As the vertical scale (h) increases, the growth rates of

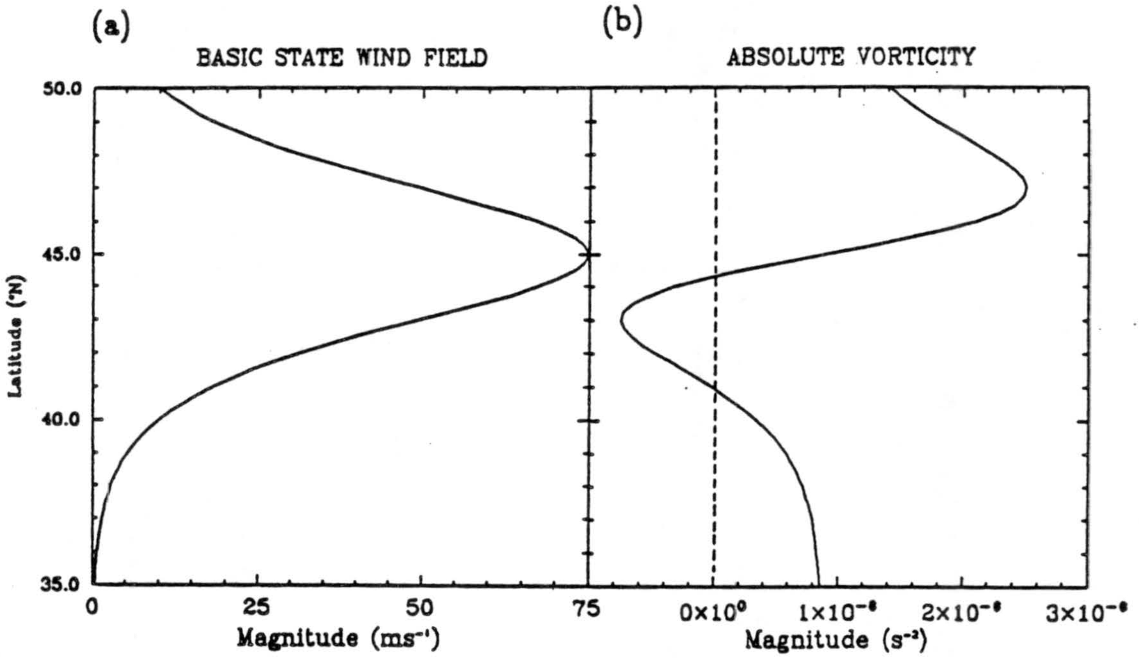

Figure 2.2: (a) Midlatitude Bickley jet (in ms^{-1}), $u_o = 75$ ms^{-1}, $Y_A = 45°N$, $Y_B = 3°$. (b) Absolute vorticity times the Coriolis parameter, $f\bar{\eta}$ (in s^{-2}). For the jet case in Fig. 2.2a. Here the condition for inertial instability is where $f\bar{\eta} < 0$.

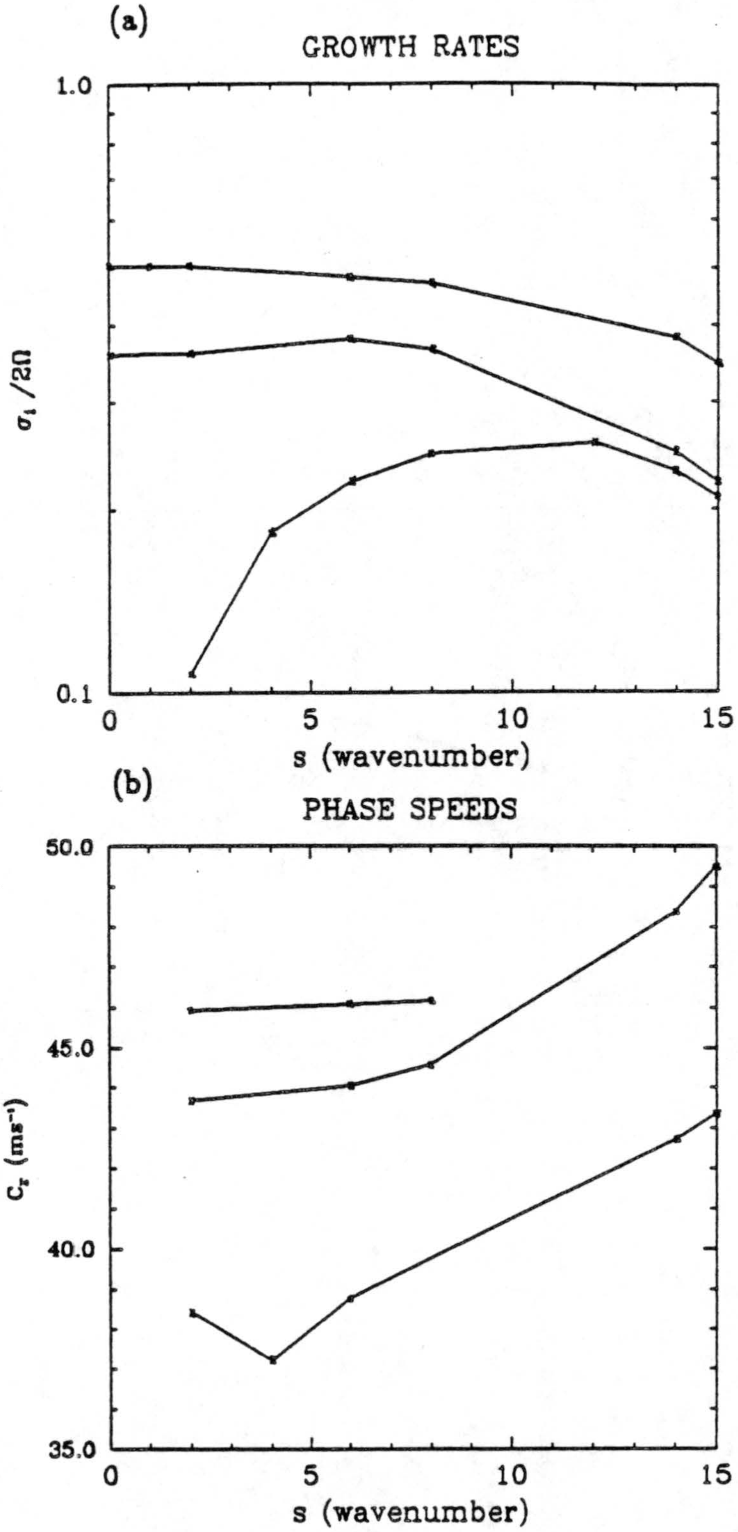

Figure 2.3: (a) Nondimensional growth rates (σ_i) as a function of wavenumber (s) for several values of equivalent depth in meters. For jet profile in Fig. 2.2a. Using the nondimensional factor, 2Ω, where $\Omega = 7.292 \times 10^{-5}\ s^{-1}$. (b) Phase speeds ($c_r$) in ms^{-1} corresponding to growth rate curves in Fig. 2.3a.

(a)

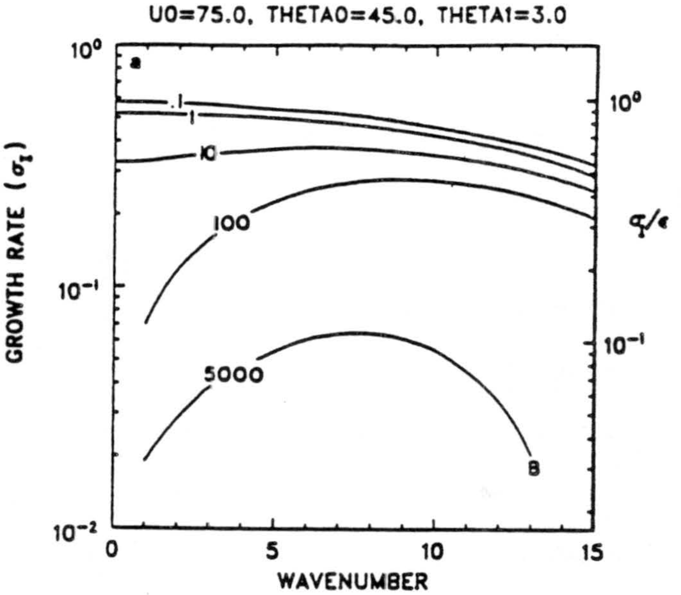

(b)

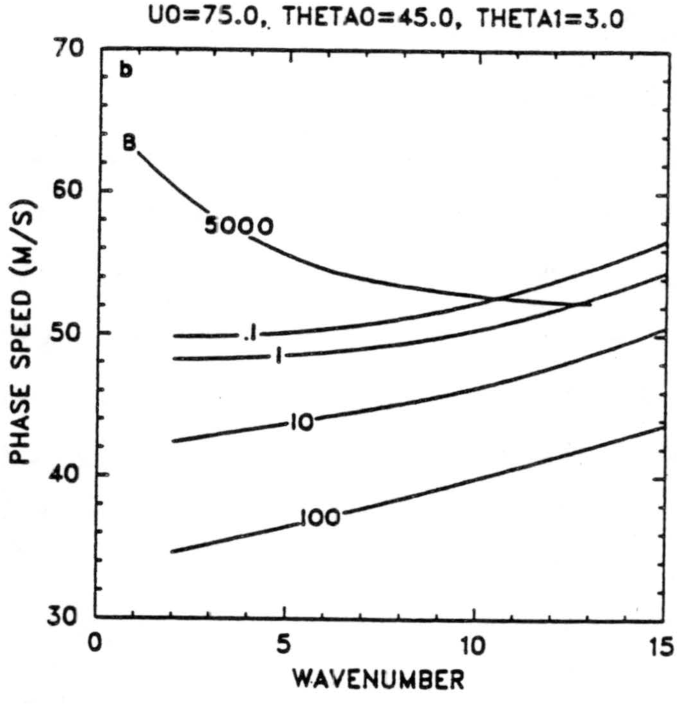

Figure 2.4: (a) Nondimensional growth rates for $u_o = 75$ ms^{-1}, $Y_A = 45°$, $Y_B = 3°$ as a function of wavenumber for several values of equivalent depth. Value along a curve represents equivalent depth in meters. Scale to the right of the plot gives the relative growth rate (σ_i), that is, in comparison with the maximum possible growth rate ϵ (where $\epsilon = 5.96 \times 10^{-1}$). B signifies barotropic instability. (b) Phase speeds (c_r) in ms^{-1} corresponding to growth rate curves in Fig. 2.4a. Taken from Stevens and Ciesielski, 1986.

the symmetric ($s = 0$) instability decreases rapidly. This stabilization occurs, as shown by Stevens (1983), because a meridional pressure gradient is established which tends to oppose the inertial instability. This stabilization process is rather ineffective, however, for asymmetric ($s \neq 0$) modes, in which the zonal pressure gradient is nonnegligible. For larger s, the fractional change in growth rate with vertical scale is asymptotically small. As a result, for all vertical scales but the shallowest, the preferred inertial instability occurs in asymmetric modes. At $h = 10$m, the maximum growth rate occurs around $s = 6$, and around $s = 8$ for $h = 100$m. These results concur with SC's. We see from Fig. 2.1a that whether it is symmetric instability or any other most unstable mode, they do not dominate (exponential growth) for quite some time which brings up the statement made earlier that a realistic instability may have destroyed itself within this time frame.

We can see in the plot of phase speed, c_r, versus wavenumber, Fig. 2.3b, that these results are relatively close to those of SC.

Figures 2.5a through 2.6c are depictions of the amplitude and phases of the perturbation variables after the most unstable mode is dominate for the case $h = 10$m and $s =$ 6. They correspond quite well with the plots of SC's Fig. 2.7. The three Figs. 2.5a, 2.5b, 2.5c of the amplitude, have been normalized to the largest value of the three variables. We see a little background noise on the outer reaches of these figures but this can be ignored since their values (on the order of 'white noise') are small compared to the main features. These noise features also produce large, noisy phase changes in Figs. 2.6a, 2.6b, 2.6c. Again these can be ignored and the main region we're interested in, 39° to 46° is of importance.

We can see the phase differences of the three maxima on the u' amplitude Fig. 2.4a and the gradual phase change of the v' perturbation variable across its maximum. And we also see the large phase change in the trough of the geopotential. Starting from the 'white noise' initial values, the momentum perturbation fields as seen in Figs. 2.5a, 2.5b have grown from the inertially unstable region shown in Fig. 2.2b, this is on the anticyclonic side of the jet. These particular features are the results of the dominance of the most unstable mode due to the inertial instability.

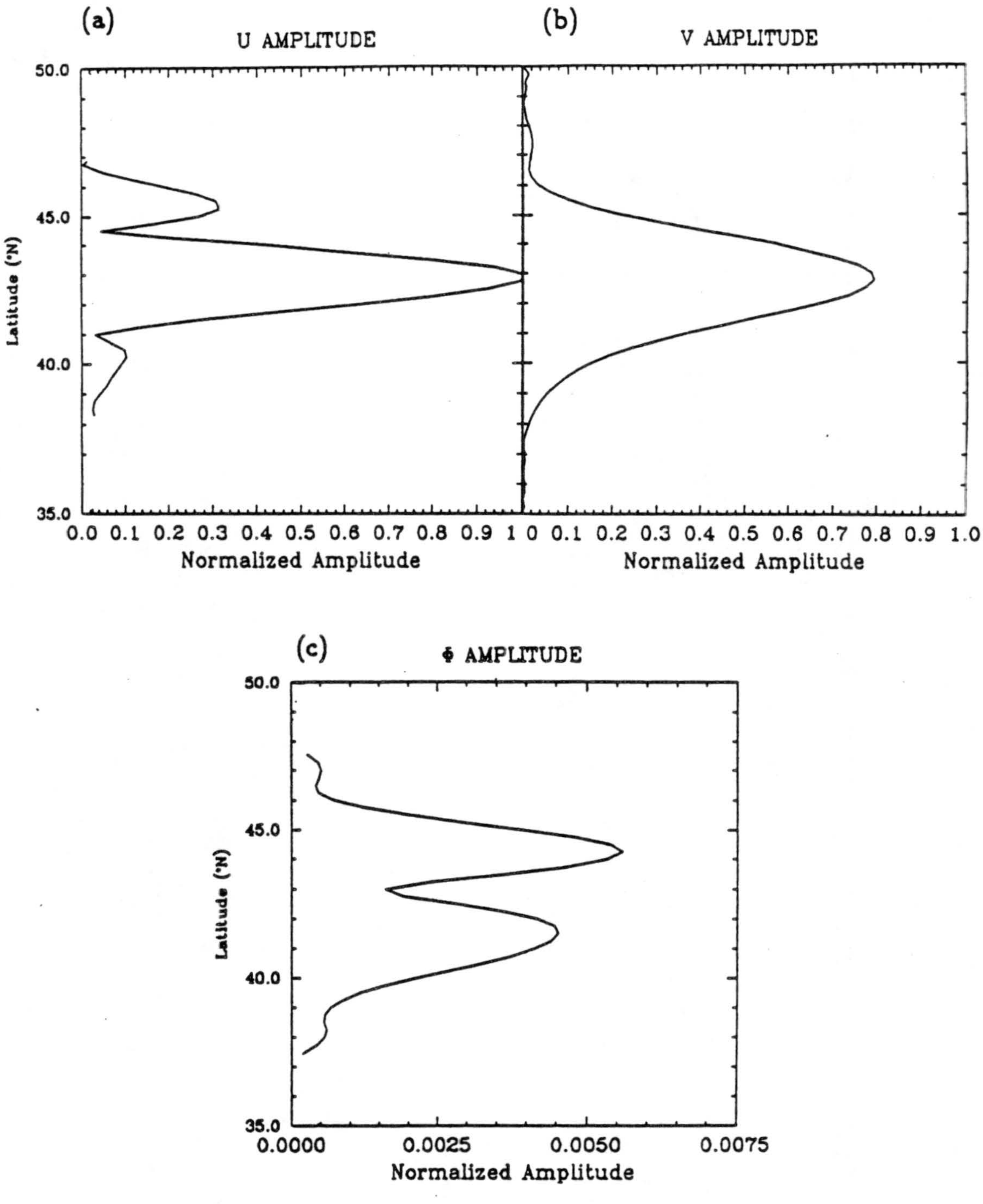

Figure 2.5: (a) Nondimensional amplitude for u' (in ms^{-1}) for most unstable mode at h = 10 m and s = 6 for jet profile in Fig. 2.2a. Normalized with v' and ϕ' amplitudes. t = 100,000 seconds. Nondimensional parameter is $1/(2\Omega a)$, where $\Omega = 7.292 \times 10^{-5}\ \mathrm{s}^{-1}$, $a = 6.37 \times 10^{-6}$ m. (b) Same as Fig. 2.5a except for v' in ms^{-1}. (c) Same as Fig. 2.5a Except for ϕ' in $\mathrm{m}^2\ \mathrm{s}^{-2}$, and nondimensional parameter is squared.

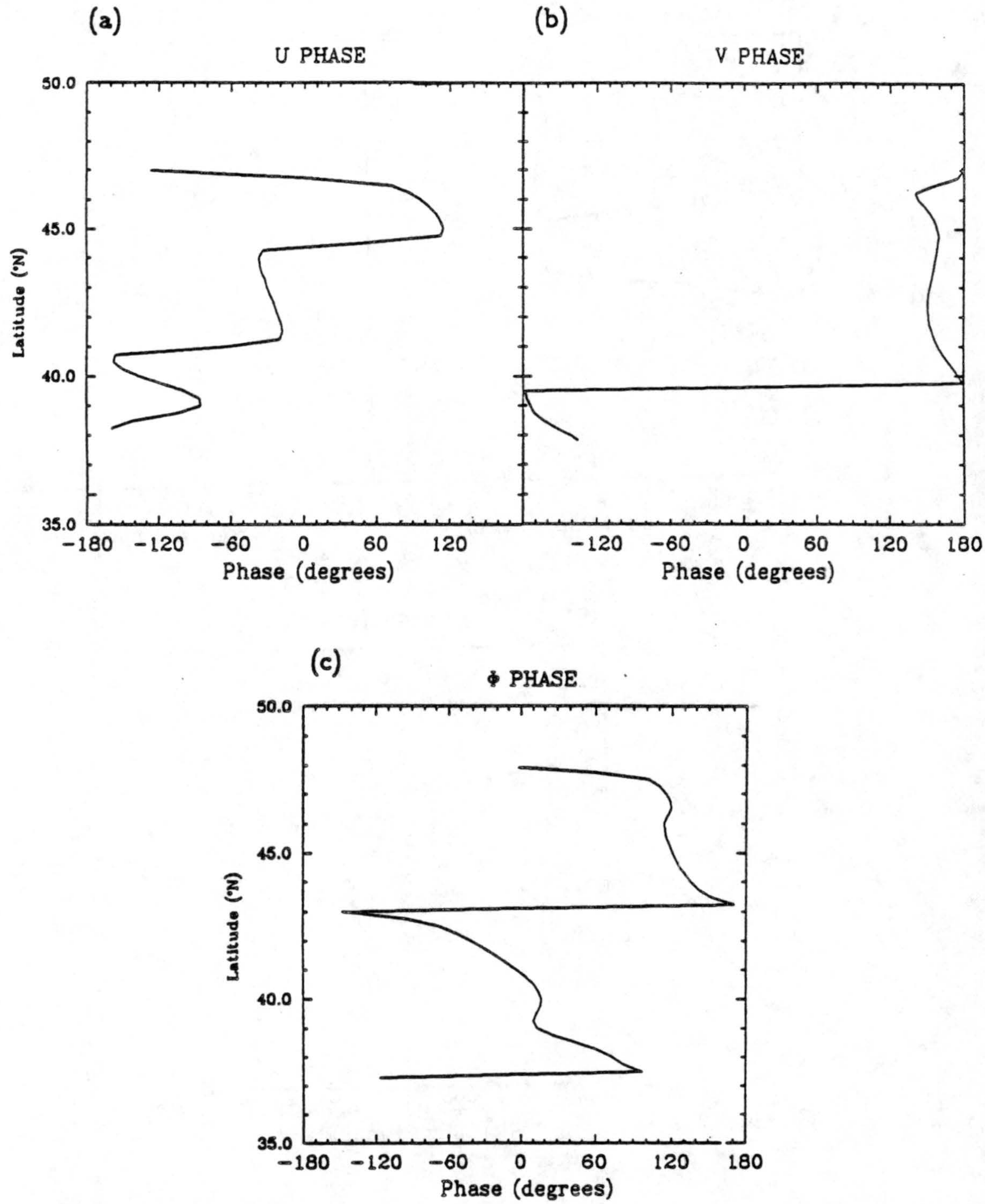

Figure 2.6: (a) Phase for u' for jet profile in Fig. 2.5a. (b) Same as Fig. 2.6a except for v'. (c) Same as Fig. 2.6a except for ϕ'.

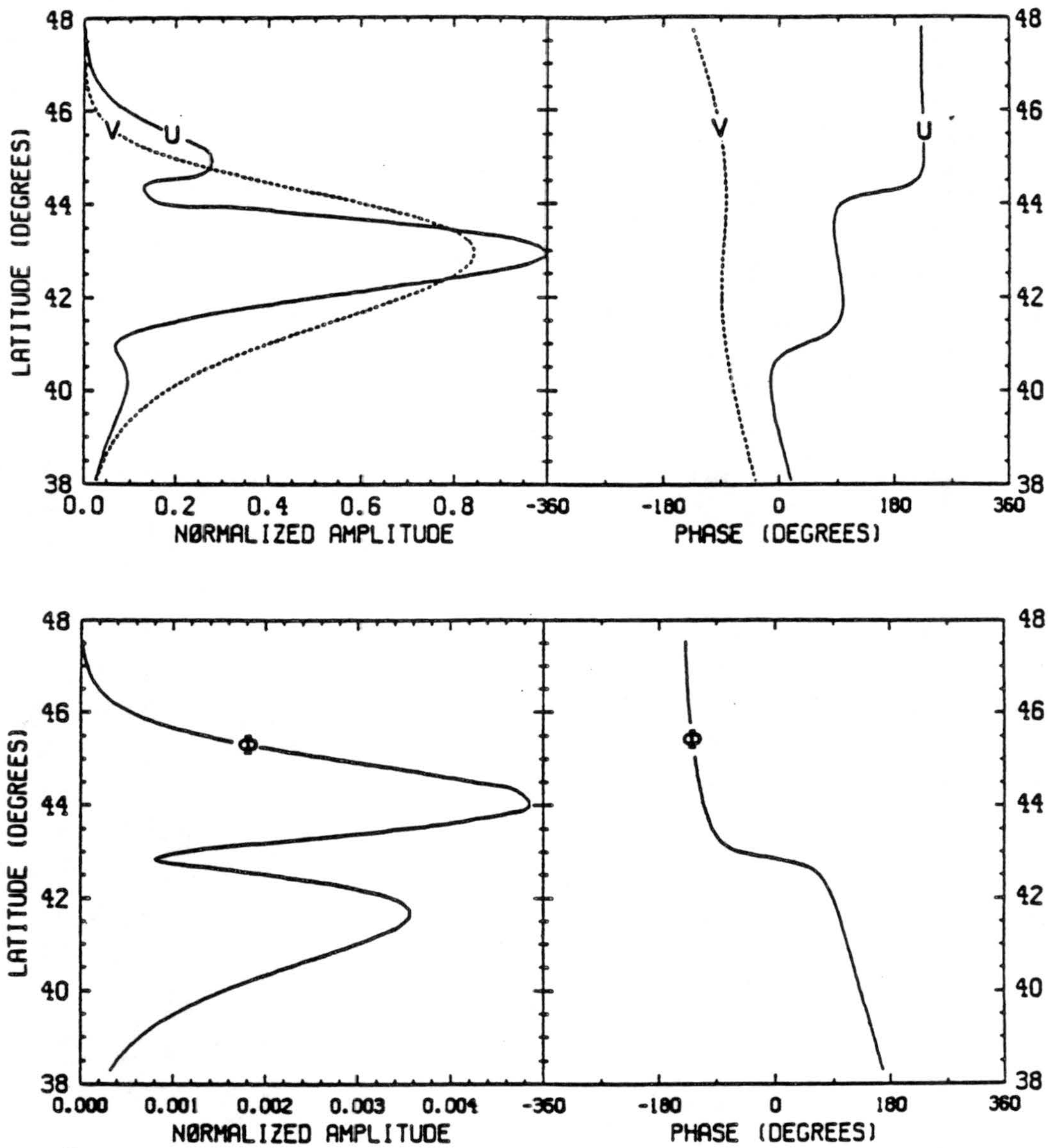

Figure 2.7: Nondimensional amplitude and phase for u', v' and ϕ' eigenfunctions for maximum instability at h = 10 m and s = 6 for jet profile u_o = 75 ms^{-1}, Y_A = 45°N, Y_B = 3°. Amplitudes have been divided by the maximum u eigenvector for plotting purposes. Taken from Stevens and Ciesielski, 1986.

Chapter 3

THE PRIMITIVE EQUATION MODEL DEVELOPMENT

Having produced and tested the necessary techniques for the shallow water equation model in the previous chapter, the development of the primitive equation model is now a relatively straightforward procedure. These techniques included the Chebyshev spectral transforms, the Runge-Kutta fourth order time difference scheme and the basic algorithm needed to solve the set of equations.

The main steps involved to accomplish this adaptation include adding the hydrostatic and thermodynamic equations, along with the variables w' and T', that is, vertical velocity and temperature, respectively. In addition the routines are changed from one-dimensional to two-dimensional in y, z and the extra terms that come from using $\bar{u}(y, z)$. Appendix B provides flow charts of the computer code needed to run the model described in this section.

3.1 The numerical model

3.1.1 Basic equations

The primitive equation set consists of three prognostic equations (for u, v, T) and two diagnostic equations (for w, ϕ). We begin with the nonlinear inviscid set on an f-plane (Holton, 1979) in isobaric coordinates:

$$\frac{\partial u}{\partial t} + u\frac{\partial u}{\partial x} + v\frac{\partial u}{\partial y} + w^*\frac{\partial u}{\partial z^*} - fv = -\frac{\partial \phi}{\partial x} \tag{3.1}$$

$$\frac{\partial v}{\partial t} + u\frac{\partial v}{\partial x} + v\frac{\partial v}{\partial y} + w^*\frac{\partial v}{\partial z^*} + fu = -\frac{\partial \phi}{\partial y} \tag{3.2}$$

$$\frac{\partial T}{\partial t} + u\frac{\partial T}{\partial x} + v\frac{\partial T}{\partial y} + w^*\left(\frac{\partial T}{\partial z^*} + \kappa T\right) = 0 \tag{3.3}$$

$$\frac{\partial \phi}{\partial z^*} = RT \tag{3.4}$$

$$\frac{\partial u}{\partial x} + \frac{\partial v}{\partial y} + \frac{\partial w^*}{\partial z^*} - w^* = 0 \tag{3.5}$$

where (3.1), (3.2) are the momentum equations, (3.3) is the thermodynamic energy equation, (3.4) is the hydrostatic equation, and (3.5) is the continuity equation. The heating function, $\dot{q}$, on the right hand side of the thermodynamic energy equation has been set to zero. We use the vertical 'log p' coordinate where $z^* \equiv \ell n(p_o/p)$ and $w^* = \frac{dz^*}{dt} = \frac{-1}{p}\frac{dp}{dt} = \frac{-\omega}{p}$; z^* is measured in scale heights which is nondimensional.

To simplify this set of equations, we linearize it by assuming the dependent variables have the form:

$$u = \bar{u}(y, z^*) + u'(x, y, z^*, t) \tag{3.6}$$

$$v = v'(x, y, z^*, t) \tag{3.7}$$

$$T = \bar{T}(y, z^*) + T'(x, y, z^*, t) \tag{3.8}$$

$$w^* = w'(x, y, z^*, t) \tag{3.9}$$

$$\phi = \bar{\phi}(y, z^*) + \phi'(x, y, z^*, t) \tag{3.10}$$

where the barred quantities are the basic states and the primed quantities are the perturbations. The x-direction in our model is set to be the zonal component since on an f-plane it is arbitrary. We use a zonal jet for this work so the mean wind field is included only through the zonal component $\bar{u}$; $\bar{v}$ is assumed to be zero and by continuity $\bar{w} = 0$. Neglecting the nonlinear products of perturbation quantities produces the following linear set of equations:

$$\frac{\partial u'}{\partial t} + \bar{u}\frac{\partial u'}{\partial x} + v'\frac{\partial \bar{u}}{\partial y} + w'\frac{\partial \bar{u}}{\partial z^*} - fv' = -\frac{\partial \phi'}{\partial x} \tag{3.11}$$

$$\frac{\partial v'}{\partial t} + \bar{u}\frac{\partial v'}{\partial x} + fu' = -\frac{\partial \phi'}{\partial y} \tag{3.12}$$

$$\frac{\partial T'}{\partial t} + \bar{u}\frac{\partial T'}{\partial x} + v'\frac{\partial \bar{T}}{\partial y} + w'\left(\frac{\partial \bar{T}}{\partial z^*} + \kappa\bar{T}\right) = 0 \tag{3.13}$$

$$\frac{\partial \phi'}{\partial z^*} = RT' \tag{3.14}$$

$$\frac{\partial u'}{\partial x} + \frac{\partial v'}{\partial y} + \frac{\partial w'}{\partial z^*} - w' = 0 \tag{3.15}$$

The independent spatial variables x, y, z^* are set within the following boundaries:

$$\begin{aligned} x &\in [0, L_1] \\ y &\in [0, L_2] \\ z^* &\in [0, D] \end{aligned} \tag{3.16}$$

For the purpose of making use of the spectral transforms the coordinate system is changed to:

$$\begin{aligned} &X \in [0, 2\pi] && \text{zonal} \\ &Y \in [-1, +1] && \text{meridional} \\ &Z \in [-1, +1] && \text{vertical} \end{aligned} \tag{3.17}$$

using the transformation equations:

$$\begin{aligned} X &= 2\pi\frac{x}{L_1} \\ Y &= \frac{y - \frac{L_2}{2}}{\frac{L_2}{2}} \\ Z &= \frac{z^* - \frac{D}{2}}{\frac{D}{2}} \end{aligned} \tag{3.18}$$

Now we use the chain rule on the above set of equations along with the transformation equations to get:

$$\frac{\partial u'}{\partial t} + \bar{u}\frac{\partial u'}{\partial X}\frac{2\pi}{L_1} + v'\frac{\partial \bar{u}}{\partial Y}\frac{2}{L_2} + w'\frac{\partial \bar{u}}{\partial Z}\frac{2}{D} - fv' = -\frac{\partial \phi'}{\partial X}\frac{2\pi}{L_1} \tag{3.19}$$

$$\frac{\partial v'}{\partial t} + \bar{u}\frac{\partial v'}{\partial X}\frac{2\pi}{L_1} + fu' = -\frac{\partial \phi'}{\partial Y}\frac{2}{L_2} \tag{3.20}$$

$$\frac{\partial T'}{\partial t} + \bar{u}\frac{\partial T'}{\partial X}\frac{2\pi}{L_1} + v'\frac{\partial \bar{T}}{\partial Y}\frac{2}{L_2} + w'\left(\frac{\partial \bar{T}}{\partial Z}\frac{2}{D} + \kappa\bar{T}\right) = 0 \tag{3.21}$$

$$\frac{\partial \phi'}{\partial Z}\frac{2}{D} = RT' \tag{3.22}$$

$$\frac{\partial u'}{\partial X}\frac{2\pi}{L_1} + \frac{\partial v'}{\partial Y}\frac{2}{L_2} + \frac{\partial w'}{\partial Z}\frac{2}{D} - w' = 0 \tag{3.23}$$

where the symbols in these equations have the following definitions:

u', v'	zonal and meridional velocity perturbations
T'	temperature perturbation
w'	vertical velocity perturbation
ϕ'	geopotential perturbation
f	Coriolis parameter, assumed f=constant (f-plane)
t	time
$\bar{u}$	basic state zonal jet
$\bar{T}$	basic state temperature
L_1	domain length in meters
L_2	domain width in meters
D	domain height in scale heights
$\kappa \equiv R/c_p$	constant = universal gas constant/specific heat

The coefficients within the set of equations are independent of x; therefore we fourier transform the equations in the x direction. Using fourier expansion, any perturbation quantity can be written as

$$\chi'(X,Y,Z,t) = Re\left\{\sum_{N_x=0}^{\infty} \chi'_k(Y,Z,t)e^{ik\frac{L_1}{2\pi}X}\right\} \tag{3.24}$$

where k is the assumed zonal wavenumber ($k = \frac{2\pi}{L_x}$ where L_x = zonal wavelength, $\frac{L}{N_x}$, L is distance around latitude circle, N_x represents number of waves around a circle of latitude). The perturbation coefficients, χ'_k, are all considered complex.

By applying all of the above assumptions we derive the following linearized primitive equation set for the perturbation of a mean x-independent flow.

$$\frac{\partial u'_k}{\partial t} + \bar{u}iku'_k + v'_k\frac{\partial \bar{u}}{\partial Y}\frac{2}{L_2} + w'_k\frac{\partial \bar{u}}{\partial Z}\frac{2}{D} - fv'_k + ik\phi'_k = 0 \tag{3.25}$$

$$\frac{\partial v'_k}{\partial t} + \bar{u}ikv'_k + fu'_k + \frac{\partial \phi'_k}{\partial Y}\frac{2}{L_2} = 0 \tag{3.26}$$

$$\frac{\partial T'_k}{\partial t} + \bar{u}ikT'_k + v'_k\frac{\partial \bar{T}}{\partial Y}\frac{2}{L_2} + w'_k\left(\frac{\partial \bar{T}}{\partial Z}\frac{2}{D} + \kappa\bar{T}\right) = 0 \tag{3.27}$$

$$\frac{\partial \phi'_k}{\partial Z}\frac{2}{D} = RT'_k \tag{3.28}$$

$$iku'_k + \frac{\partial v'_k}{\partial Y}\frac{2}{L_2} + \frac{\partial w'_k}{\partial Z}\frac{2}{D} - w'_k = 0 \tag{3.29}$$

The above equations now show the detailed differences *vis a vis* the set of equations (2.8), (2.9), (2.10) used in the shallow water model. Obviously, the metric coefficients of $\frac{2}{L_2}$ and $\frac{2}{D}$ in the primitive equations are from the transformed independent variable set, not produced in the shallow water set. The momentum equations are very similar except for the addition of $\left(w'_k\frac{\partial \bar{u}}{\partial Z}\frac{2}{D}\right)$ in the u-momentum equation. The shallow water mass equation changes from a prognostic equation for ϕ'_k to a diagnostic equation with the addition of the vertical direction, Z, and the vertical velocity, w'_k. To filter out short waves like sound waves, we have made the hydrostatic assumption, thus the addition of (3.28) containing ϕ'_k and T'_k. Finally, we have added the thermodynamic equation which contains advection terms such as $w'_k\left(\frac{\partial\bar{T}}{\partial Z}\frac{2}{D}+\kappa\bar{T}\right)$ and $\left(v'_k\frac{\partial\bar{T}}{\partial Y}\frac{2}{L_2}\right)$.

The model equations are applied within a limited area, 1665 kilometers wide (approximately 15° latitude) and 3 scale heights high (approximately 24 km). We assume a strong mid-latitude westerly jet. The anti-cyclonic side (the southern side) of the jet is the area of negative absolute vorticity in the shallow water model and we expect the same area (extended in the vertical) to possess negative potential vorticity; hence we expect the inertially unstable disturbance to grow in that region.

3.1.2 Dissipation

Finding the true "most unstable mode" with our model can be a problem if short wave features, such as computational instability, develop. Such instabilities can have large growth rates, making the computation of the most unstable mode of a larger wave feature very difficult. Therefore we need to apply damping to our prognostic equations on a scale able to dissipate this computational noise.

Normally frictional forces due to molecular viscosity and heating due to molecular diffusion are neglected in the primitive equations on the basis of scale analysis. However, near the ground strong vertical wind shears and surface heating continually lead to the development of turbulent eddies, which are more effective mixing agents than molecular diffusion. This region, called the planetary boundary layer, is typically confined to the lowest kilometer of the atmosphere. Therefore we parameterize this physical process with an internal dissipation, α, throughout the domain with largest values in the lowest kilometer. In the momentum equations we use Rayleigh friction, $\alpha_R(Z)$; in the thermodynamic equation, Newtonian cooling, $\alpha_N(Z)$, is assumed. With linear dissipation and our prognostic equations become

$$\frac{\partial u'_k}{\partial t}+\ldots=-\alpha_R u'_k \tag{3.30}$$

$$\frac{\partial v'_k}{\partial t}+\ldots=-\alpha_R v'_k \tag{3.31}$$

$$\frac{\partial T'_k}{\partial t} + \ldots = -\alpha_N T'_k \tag{3.32}$$

For simplicity, we set $\alpha_R = \alpha_N = \alpha$. The terms that involve α are included in the set of spectrally nonlinear terms and are calculated within the model during the "physical space" stage.

Our assumed $\alpha(Z)$ is a function on the order of $10^{-5}\mathrm{s}^{-1}$ ($\sim$ 1 day^{-1}), which is approximately the fastest growth rate expected from these short waves, and increases exponentially to an order of magnitude larger in the lowest kilometer, giving us a kind of "mixed layer". We also have included a "sponge layer" in the uppermost scale height. This also is an exponential increase by an order of magnitude larger to $10^{-4}\mathrm{s}^{-1}$ at $z^* = D$. We added this to achieve a steady oscillation due to our boundary condition of a lid at the top, $w' = 0$.

3.1.3 Space discretization: Spectral method

Whereas the first step in transforming the equations into spectral space is the fourier zonal transform described earlier, the next step is to transform this set into spectral space in the meridional direction (Y) and then the vertical direction (Z) using Chebyshev polynomials as the basis functions in both directions. The procedure followed in Section 2.1.2 for the most part applies here. The only difference is the addition of the vertical transform in which we are using the same steps as in the horizontal transforms.

The variables in the Chebyshev expansion are:

$$\chi'_k(Y, Z, t) = \sum_{m=0}^{N_Y} \sum_{n=0}^{N_Z} \hat{\chi}_{kmn}(t) G_m(Y) G_n(Z) \tag{3.33}$$

where $\hat{\chi}_{kmn}$ is the spectral coefficient and G_m, G_n are the mth, nth Chebyshev polynomials. Refer to Appendix A and Section 2.1.2 for more details of the Chebyshev spectral transforms.

Applying this transform to our set of equations, we get:

$$\frac{d\hat{u}_{kmn}}{dt} - f\hat{v}_{kmn} + ik\hat{\phi}_{kmn} = -(\bar{u}iku'_k)_{mn} - \left(\frac{2}{L_2}\frac{\partial \bar{u}}{\partial Y} v'_k\right)_{mn} - \left(\frac{2}{D}\frac{\partial \bar{u}}{\partial Z} w'_k\right)_{mn} - (\alpha_R u'_k)_{mn} \tag{3.34}$$

$$\frac{d\hat{v}_{kmn}}{dt} + f\hat{u}_{kmn} + \frac{2}{L_2}\frac{\partial \hat{\phi}_{kmn}}{\partial Y} = -(\bar{u}ikv'_k)_{mn} - (\alpha_R v'_k)_{mn} \tag{3.35}$$

$$\frac{d\hat{T}_{kmn}}{dt} = -(\bar{u}ikT'_k)_{mn} - \left(\frac{2}{L_2}\frac{\partial \bar{T}}{\partial Y}v'_k\right)_{mn} - \left[w'_k\left(\frac{2}{D}\frac{\partial \bar{T}}{\partial Z} + \kappa\bar{T}\right)\right]_{mn} - (\alpha_N T'_k)_{mn} \tag{3.36}$$

$$\frac{2}{D}\frac{\partial \hat{\phi}_{kmn}}{\partial Z} = R\hat{T}_{kmn} \tag{3.37}$$

$$\left(\frac{2}{D}\frac{\partial}{\partial Z} - 1\right)\hat{w}_{kmn} = -\left(ik\hat{u}_{kmn} + \frac{2}{L_2}\frac{\partial \hat{v}_{kmn}}{\partial Y}\right) \tag{3.38}$$

The terms on the right hand side of the prognostic set of equations look similar to non-linear terms of a non-linear set of equations since the coefficients are a function of y, z. In programming, we treat them as spectrally non-linear terms and calculate them before entering Chebyshev spectral space. The rest of the terms are calculated in Chebyshev spectral space.

The number of Chebyshev spectral coefficients presently used is $N = 16$ in both Y and Z. This enables us to have both a reasonable time step and sufficient resolution [the condition for resolution in spectral space is $L/(N/\pi)$ where L is the domain size; for $N = 16$ the cross–channel (meridional) resolution is approximately 326.9 km and the vertical resolution is approximately 0.59 scale heights]. Using $N = 32$ of course doubles the resolution, but sample runs with higher resolution did not significantly alter results. Therefore, $N = 16$ is a reasonable choice to use since the CFL condition (2.20) for this method is such that the time step is inversely proportional to the square of the number of spectral coefficients, increasing the computer time enormously by making the time step much smaller.

Equations (3.34) through (3.38) are the primitive equations as they are implemented within the numerical model itself. From here on, we will refer to the physical independent variables x, y, z^* when discussing conditions and quantities.

3.1.4 Time discretization: Time integration

We will use the Runge-Kutta fourth order method (Conti, 1965) as discussed in Section 2.1.3 with the equations (2.16) through (2.19). The only difference is that we replaced the prognostic equation for ϕ' (the continuity equation) with the prognostic equation for T' (the thermodynamic equation). In addition, we need to calculate w' and ϕ' at each step from the prognostic variables by solving the diagnostic equations (the hydrostatic and continuity equations).

Along with the CFL criterion where Δt is necessarily proportional to the domain size, Δy, and inversely proportional to the speed, c, for more complicated time difference schemes Δt is also proportional to the number of steps in a time scheme and inversely proportional to the square of the number of modes used, as shown in equation (2.20). We would like to use the smallest N possible so that we can use the largest possible Δt without creating numerical instability which will be discussed in Section 3.2.

3.1.5 Boundary conditions

It is assumed that there are no fluxes of any quantity across the horizontal boundaries of the model. Therefore, on the lateral borders the meridional wind perturbations, v', are constrained to be zero. The procedure for imposing the v' boundary condition is the same as in the shallow water equation set discussed in Section 2.1.4, with the added dimension of the vertical.

The top and bottom boundary conditions are applied to the continuity and hydrostatic diagnostic equations respectively, to obtain w' and ϕ'. The conditions are applied after new values of the variables, u', v', and T', have been computed.

At the upper boundary we use

$$a_1 \frac{\partial w'_k}{\partial z^*} + a_o w'_k = 0 \quad \text{at} \quad z^* = D \tag{3.39}$$

where a_1 and a_o are constants set for various upper boundary conditions. One choice is the rigid lid ($a_1 = 0, a_o = 1$) so $w'_k = 0$. The above form of the boundary condition will also allow a radiation condition at the top.

At the lower boundary we use $W = 0$ where W is the actual vertical wind (w' is vertical wind in 'log p' coordinates) and $gW = \left(\frac{d\phi'_k}{dt}\right)$ so

$$\frac{\partial \phi'_k}{\partial t} = gW - \left(\bar{u}ik\phi'_k + v'_k\frac{\partial \bar{\phi}}{\partial y} + w'_k\frac{\partial \bar{\phi}}{\partial z^*}\right) \quad \text{at } z^* = 0 \tag{3.40}$$

3.1.6 Basic state

The basic state field for the zonal jet is the main focus of this whole problem we are studying. We need a two-dimensional jet in the meridional and vertical directions. To achieve this, we can use any number of functions to describe the jet. For simplicity we use the Bickley jet structure described in Section 2.1.5. This gives us a jet cross section similar to a bull's eye. We can vary the magnitude or the horizontal/vertical shear easily by alterating the constants.

$$\bar{u}(y, z^*) = u_o sech^2\left(\frac{y - Y_A}{Y_B}\right) * sech^2\left(\frac{z^* - Z_A}{Z_B}\right) \tag{3.41}$$

where Y_A, Z_A, Y_B, Z_B are respectively the center point in the horizontal and vertical directions and the half-width horizontally and vertically (Y_A, Y_B in meters; Z_A, Z_B in scale heights). Figure 3.1a shows us a jet using (3.41). From this function we calculate the y and z^* derivatives of $\bar{u}$.

We also need the basic states of T and ϕ. We can write $\bar{T}$ and $\bar{\phi}$ as

$$\bar{T}(y, z^*) = T_o(z^*) + T_1(y, z^*)$$

$$\bar{\phi}(y, z^*) = \phi_o(z^*) + \phi_1(y, z^*) \tag{3.42}$$

where T_o is the vertical structure and T_1 is geostrophically related to $\bar{u}$ through the thermal wind balance.

We calculate T_1 by using the geostrophic wind balance relation (3.43) to get a relation between ϕ_1 from $\bar{u}$.

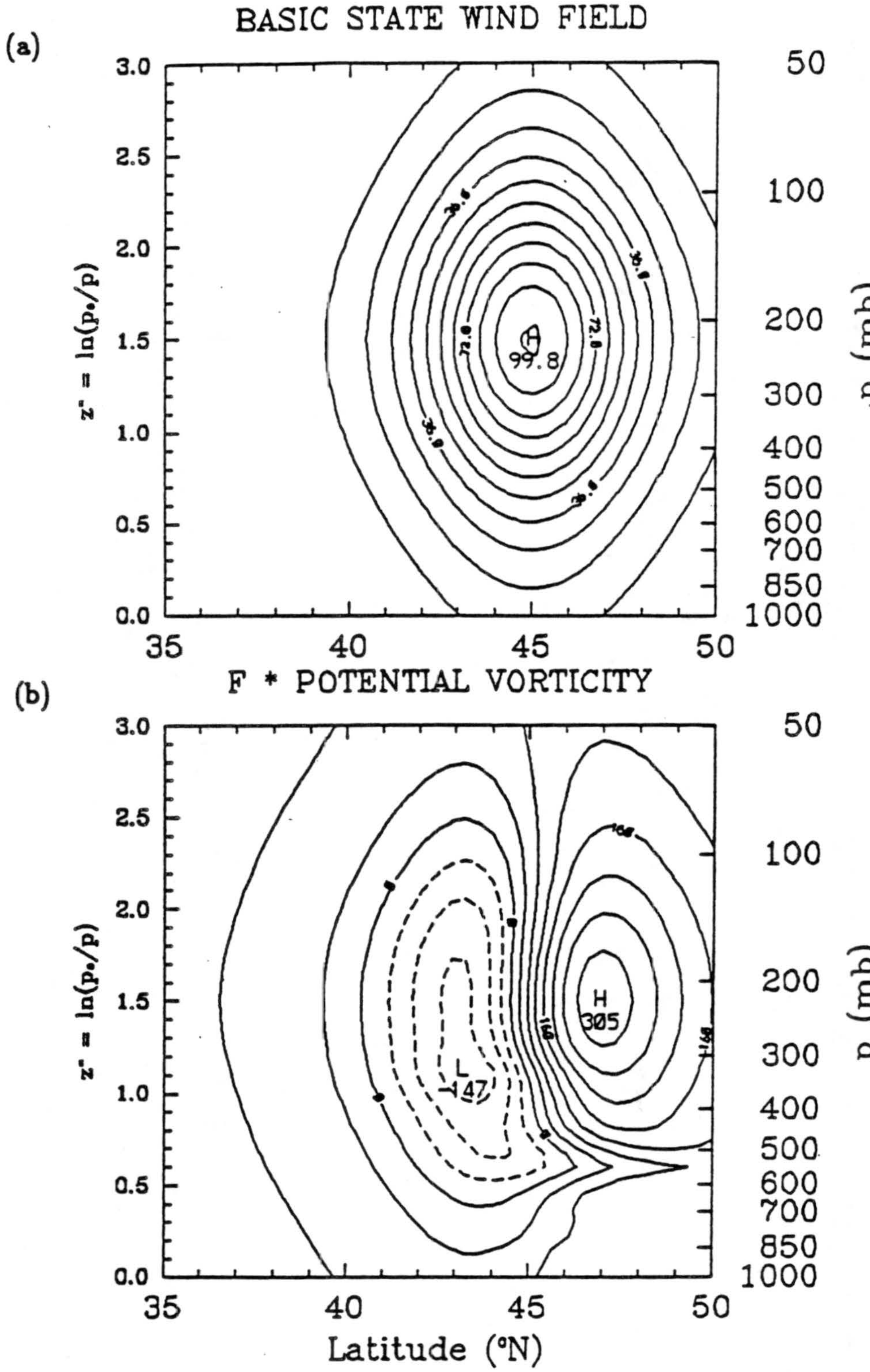

Figure 3.1: (a) Midlatitude Bickley jet (in ms^{-1}) for $u_o = 100\ ms^{-1}$. $Y_A = 45°N$, $Y_B = 3°$, $Z_A = 1.5$, $Z_B = 0.9$. Contour interval of 9.0. (b) Potential vorticity times Coriolis parameter, $f \cdot \bar{P}$, (in s^{-2}) for jet profile in Fig 3.1a. Here the condition for inertial instability is where $f \cdot \bar{P} < 0$. Contour interval of 0.4×10^{-8}. Labels scaled by 0.1×10^{11}. Negative values are dashed lines.

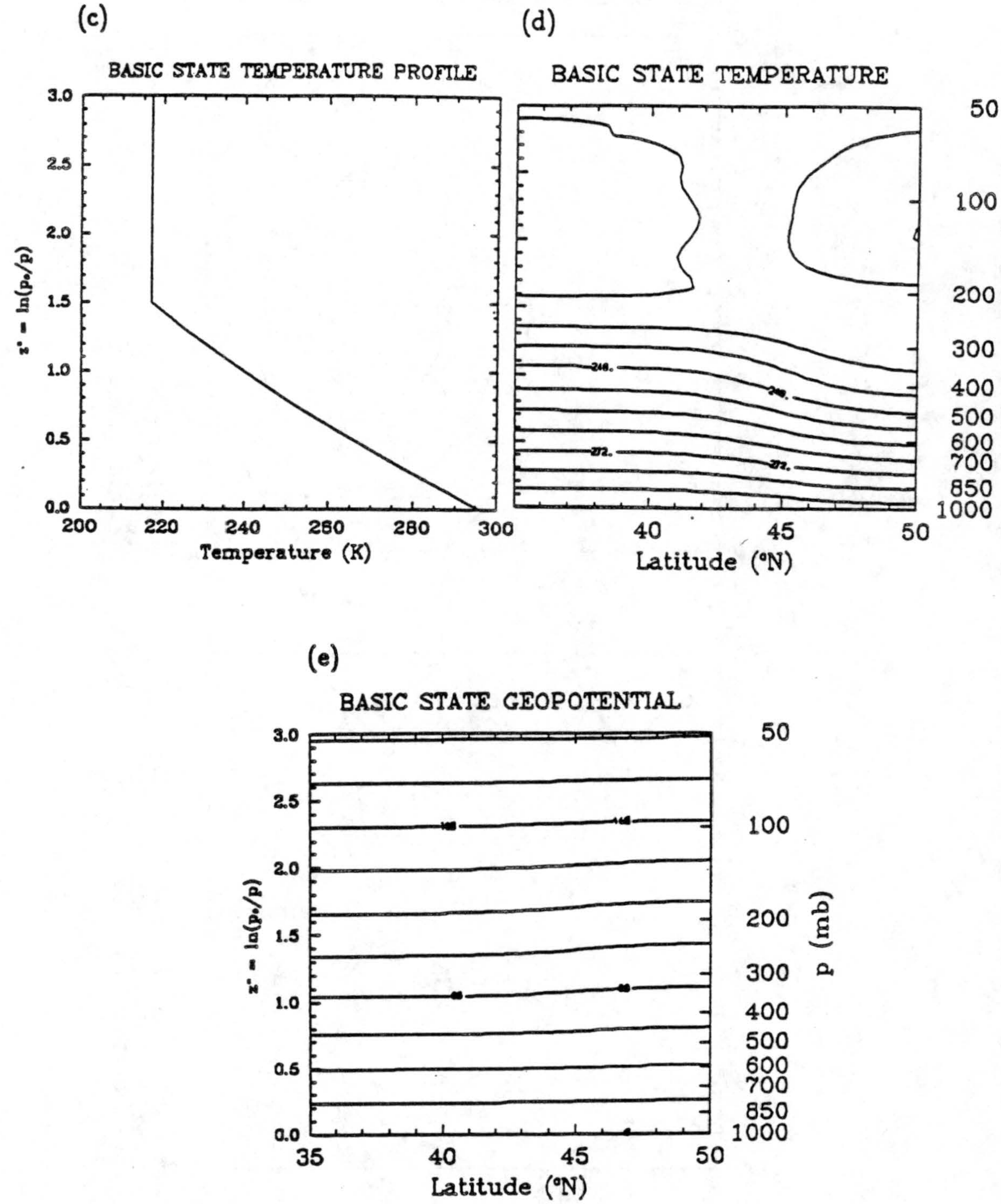

Figure 3.1: (c) Vertical stratification of basic state temperature (in K). Surface temperature = 296 K, stratospheric temperature ≅ 217 K Exponential decrease through the troposphere. Tropopause, $z^* = 1.5$. (d) Basic state temperature (in K) for jet profile Fig. 3.1a. $T_1(y, z^*) = 0$ at 45°N. Contour interval of 8.0. (e) Basic state geopotential (in m^2s^{-2} for jet profile in Fig 3.1a. Contour interval of 20,000. Labels scaled by 0.1×10^{-2}.

$$f\bar{u}(y,z^*) \quad = \quad -\frac{\partial\bar{\phi}}{\partial y} \tag{3.43}$$

$$\vdots$$

$$\bar{\phi}(y,z^*) \quad = \quad \bar{\phi}(y_o,z^*) - \int_{y_o}^{y} f\bar{u}(y,z^*)dy \tag{3.44}$$

where

$$\phi_o(z^*) = \bar{\phi}(y_o,z^*) \quad \text{and} \quad \phi_1(y,z^*) = -f\int_{y_o}^{y}\bar{u}(y,z^*)dy$$

Then using the hydrostatic relation we can get T_1 from ϕ_1.

$$T_1(y,z^*) = \frac{1}{R}\frac{\partial\phi_1}{\partial z^*} \tag{3.45}$$

Next we need $T_o(z^*)$ and $\phi_o(z^*)$. $T_o(z^*)$ is the vertical temperature profile and we have set up a function which gives us a profile similar to the U.S. Standard Atmospheric temperature profile for 45°N in July (U.S. Standard Atmospheric Supplements, 1966). We use an exponential decaying function from the surface (T_o = 296 K) to the tropopause and set T_o to be constant above that point (Fig. 3.1c). With our vertical domain of three scale heights (approximately 24 km), we have set $z^* = 1.5$ (approximately 220 mb) to be the tropopause. This profile gives us a static stability of $\Gamma_1 = 20$ K in the troposphere and $\Gamma_2 \simeq 62$ K in the stratosphere. Again using the hydrostatic relation, we can now calculate $\phi_o(z^*)$.

We therefore have set up the entire basic state fields by analytically computing all the various parts. We can view the final products in Figs. 3.1d and 3.1e. Also, we derive the vertical derivative of $\bar{T}$ from $\bar{T}$ while the meridional derivative of $\bar{T}$ we get from the thermal wind relation $\frac{d\bar{T}}{dy} = -\frac{f}{R}\frac{\partial\bar{u}}{\partial z^*}$.

The preceding description is for the two-dimensional jet in the primitive equation model. Other cases, such as simplified jets $\bar{u}(y)$ and $\bar{u}(z^*)$, can easily be set up with minor alterations to the preceding equations.

Now from the basic state quantities we have just set up, we can calculate the potential vorticity as stated in equation (1.1). To determine if the condition for negative potential vorticity exists it can be written approximately as two components, one with horizontal wind shear and the other with vertical shear. We have ignored the coefficient of potential vorticity, $\frac{\bar{\theta}N^2}{\beta g}$, since it is positive. Therefore the quantity we are plotting, as seen in the example given by Fig. 3.1b, is proportional to the potential vorticity,

$$f \cdot \bar{P} \propto \left(f\bar{\eta} - \frac{f^2}{Ri} \right) \tag{3.46}$$

where

$$\begin{aligned}
f &= \text{constant}, && \text{Coriolis parameter} \\
\bar{\eta} &= \left(f - \frac{\partial \bar{u}}{\partial y} \right), && \text{absolute vorticity} \\
Ri &= \frac{N^2}{\frac{1}{H^2}\left(\frac{\partial \bar{u}}{\partial z^*}\right)^2}, && \text{Richardson number} \\
H &= \frac{R\bar{T}}{g}, && \text{scale height} \\
N^2 &= \frac{g^2}{R\bar{T}^2}\Gamma, && \text{Brunt Väisällä frequency} \\
\Gamma &= \left(\frac{\partial \bar{T}}{\partial z^*} + \kappa \bar{T} \right), && \text{static stability}
\end{aligned}$$

3.1.7 Initialization

In order to insure against biased conditions initially, we set the perturbation momentum fields as 'white noise' (random values between 0 and 1 ms^{-1}) and let the unstable modes grow from this white noise forcing.

We initially do this for the real and imaginary parts of u' and v' and set $T' = w' = \phi' = 0$. We adjust the v' values to satisfy the north/south boundary conditions. Next we adjust the values of w' and ϕ' to be consistent with u', v' and T'. For the results to be shown, we set $w' = 0$ at the top and $\phi' = 0$ at the bottom at time zero.

Along with what we mentioned above, we have incorporated a restart feature which allows the model to start at a previously finished run time using the mass storage capabilities included when using the facilities at NCAR.

3.1.8 Modeling procedure

For each physically distinct simulation attempt, a sufficient number of model runs of varying zonal wavenumber are made to define the wavenumber at which the growth rate of total energy is greatest. Beginning with an initially small ($0.0 < |u'|, |v'| < 1.0$ ms^{-1}) perturbation, the model is run until the solution converges to a single normal mode.

The procedure to find the maximum growth rate and phase speed is similar to that described in Section 2.1.7. The main difference involves the calculation of total energy. The kinetic energy portion is the same as before (using the momentum equation) but for the available potential energy we now use the thermodynamic equation. So we again use a quantity (TE) related to the total energy as found from the energetics of the prognostic equation: $TE \propto \frac{u^2}{2} + \frac{v^2}{2} + \frac{1}{2}\frac{R}{\Gamma}T^2$ where it is averaged meridionally and vertically, $\Gamma = \frac{\partial \bar{T}}{\partial z^*} + \kappa \bar{T}$, and $R =$ universal gas constant.

3.2 Testing the Numerical Model

In this section, we test the primitive equation model we discussed in the previous section. Our primary concern is that the structural alterations we made going from the shallow water equations to the primitive equations function properly. The importance of mentioning this section, though, is due to certain features of numerical modeling that we came upon while completing this task. To accomplish this in a straightforward manner we simplify the model's parameters while keeping the primitive equation model structure. The plan is to put in a known or analytical forcing term, Q, then we should see a steady oscillating pattern in all variables after a short period.

The simplification consists of setting $\bar{u} = 0$, thus all the terms containing $\bar{u}$ and derivatives of $\bar{u}$ including $\frac{d\bar{T}}{dy}$ (due to the thermal wind relation) are zero. Therefore the equations (3.25) through (3.29) (including the dissipation terms as constant in height) become:

$$\frac{\partial u'_k}{\partial t} - f v'_k = -ik\phi'_k - \alpha_R u'_k \tag{3.47}$$

$$\frac{\partial v_k'}{\partial t} + f u_k' = -\frac{\partial \phi_k'}{\partial y} - \alpha_R v_k' \tag{3.48}$$

$$\frac{\partial T_k'}{\partial t} + w_k' \left(\frac{\partial \bar{T}}{\partial z^*} + \kappa \bar{T} \right) = Q - \alpha_N T_k' \tag{3.49}$$

$$\frac{\partial \phi_k'}{\partial z^*} = R T_k' \tag{3.50}$$

$$\left(\frac{\partial}{\partial z^*} - 1 \right) w_k' = - \left(i k u_k' + \frac{\partial v_k'}{\partial y} \right) \tag{3.51}$$

The boundary conditions are

$$v_k' = 0 \quad \text{at} \quad y = 0, L_2$$

$$w_k' = 0 \quad \text{at} \quad z^* = D$$

$$W = 0 \quad \text{at} \quad z^* = 0$$

where $gW = \left(\frac{d\phi_k}{dt}\right)' = \frac{\partial \phi_k'}{\partial t} + w_k' \frac{\partial \bar{\phi}}{\partial z^*}$ therefore $\frac{\partial \phi_k'}{\partial t} = -w_k' R\bar{T}$ at $z^* = 0$.

We have included a heating (forcing) term, Q, in the thermodynamic equation and we also set all initial conditions to zero. We have $\bar{T}$ exponentially decaying with height until the tropopause (midpoint in z^*), then it's isothermal to the top boundary. This enables us to view the effect of the forcing term on this system. The Q is set up to be an analytical forcing, one that we are able to discern the results. Thus allowing us to check the time integration scheme, the routines of the prognostic and diagnostic equations, how the variables interact with each other, and the routines for the boundary conditions. Proceeding with this study, we came upon some of the problems associated with high frequency waves (i.e. Lamb waves).

The heating was chosen to have maximum values at the boundaries allowing compatibility between the forcing on v_k' and the north/south boundary conditions on v_k'. The meridional forcing, $Q(y)$, was chosen to excite a single horizontal mode; with v_k' having an analytic solution, $\propto \sin\left(\frac{n\pi}{L_2} y\right)$. The heating function defined below satisfies these conditions:

$$Q = Q_o \cdot Q_x \cdot Q_y \cdot Q_z \cdot Q_t \tag{3.52}$$

$$Q_o = 1K/\text{day}$$

$$Q_x = e^{ikx}$$

$$Q_y = \cos\theta - A\sin\theta$$

$$Q_z = \sin\left(\frac{\pi}{D}z^*\right)e^{\frac{z^*}{2}}$$

$$Q_t = e^{-i\sigma t} = e^{-i\frac{2\pi}{\tau}t}$$

with $A = \frac{f}{\sigma + i\alpha_R}\frac{k}{\ell}$ and $\theta = \frac{n\pi}{L_2}y$ and $\tau = \frac{2\pi}{\sigma} = \frac{1}{\alpha}$ where τ is the period, σ is the frequency and α is the constant dissipation. Q_o is a constant representing an average heating rate; Q_x is the zonal structure of the forcing, which corresponds to a single propagating wave; Q_y is the meridional structure, with two cosine waves using $n = 4$; Q_z is the vertical structure, with a half sine wave; Q_t is the time scale of the forcing which causes the perturbations to oscillate in time and settle into a steady oscillation corresponding to the period, τ.

Numerical instability is a problem that can arise when using a numerical prediction model. It usually is the side effect of violating the CFL condition, $c\frac{\Delta t}{\Delta y} < 1$; either the time step is too large or the spatial resolution is too small. In this case using a heating function, as part of our simplifying measures to view the analytic solution we had set the meridional domain relatively small without adjusting the time step accordingly. This resulted in the numerical mode dominating as seen in Figs. 3.2a and 3.2b, the amplitude of u'_k and v'_k respectively. These figures were made after a very short period of integration, showing how volatile numerical instability can be.

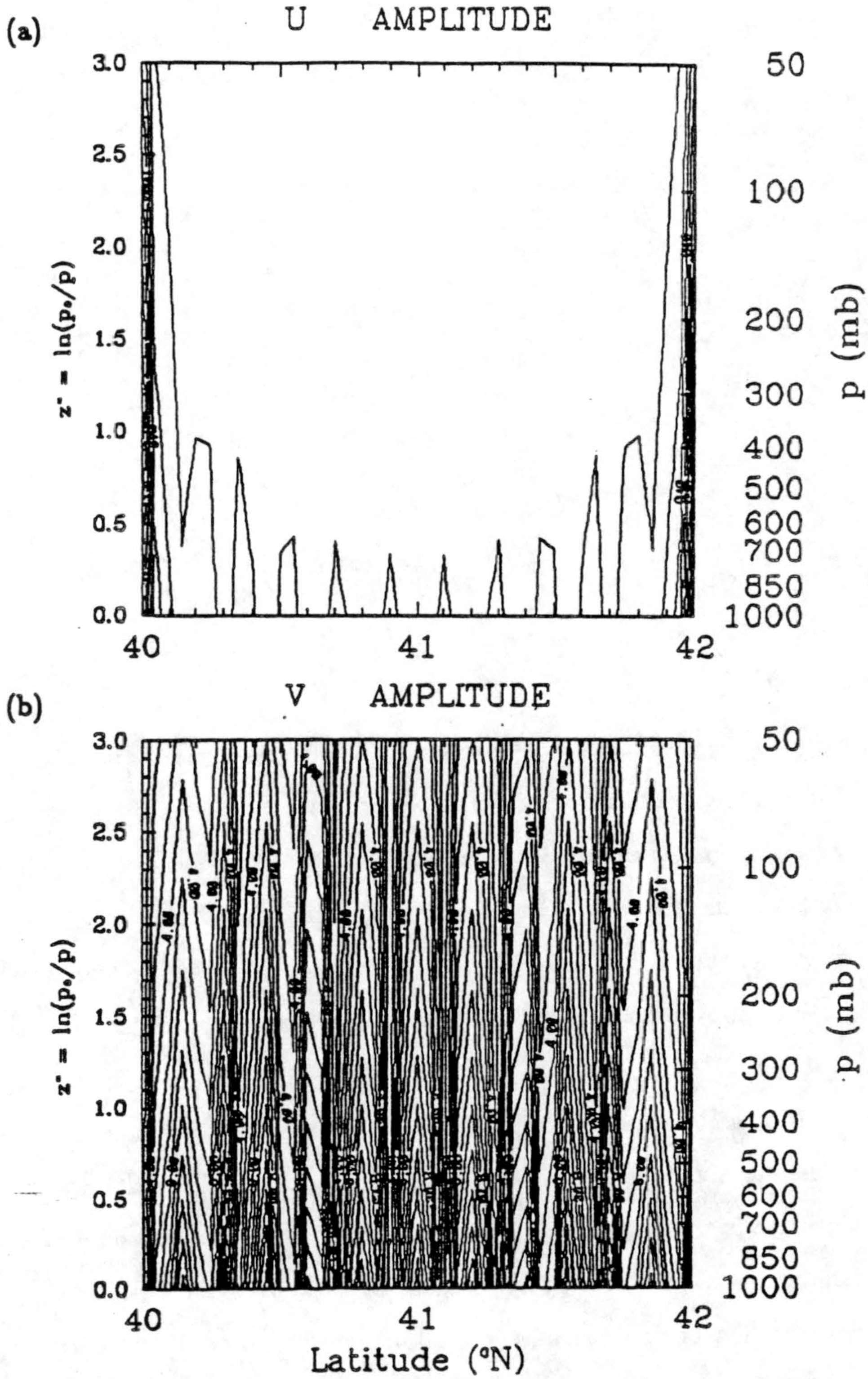

Figure 3.2: (a) Amplitude for u' (in ms^{-1}) for case where $\bar{u} = 0$ in primitive equations. Uses heating function, Q, described in Section 3.2. This shows numerical instability, Lamb waves; the time step is too large, $\Delta t = 10$ seconds. $t = 100$ seconds. Domain size = 200 km ($\sim 2°$ latitude). Contour interval of 0.1×10^{-1}. (b) Same as Fig. 3.2a except for v'. Contour interval of 1.0.

As seen in Fig. 3.2b, the characteristics of v'_k seem to be that of "Lamb" waves. Lamb waves are horizontally propagating acoustic waves with their maximum amplitude at the lower boundary and decay away from the boundary (Holton, 1979). Also, we looked closely at the actual spectral coefficients during this run and found the largest values to be at the highest horizontal modes; this told us that very small (fastest) waves were dominating the model calculation, since higher order coefficients resolve higher frequency waves. Another reason why they are Lamb waves is that we are knowingly not filtering them out. The normal procedure to filter out Lamb waves is to set $\omega = 0$ (equivalent to $w'_k = 0$) at the lower boundary (vertically propogating sound waves are already filtered out due to the hydrostatic equation). In our model, we have avoided this form of the lower boundary condition in order to set a condition on the geopotential; this allows us to solve the diagnostic hydrostatic equation for ϕ'_k, so we have set the actual vertical velocity, $W = 0$ at $z^* = 0$.

This brings us back to the fact that we need to adjust our time step and domain resolution to meet the CFL condition. Calculation of the external (corresponds to short unstable waves) and the 1st internal mode shows the former mode to be five times faster than the 1st internal mode. With this in mind, by decreasing Δt by a factor of five, the spurious numerical external mode is removed. Now we are able to stay numerically stable and not worry about numerical Lamb waves interfering.

Now we proceed with the simplified model run by making Δt smaller to work with the small domain, L_2, we have set. Figures 3.4a through 3.4e show the results of running the model using $\Delta t = 2$ seconds, $L_2 = 200$km, $L_x = 600$km , $L_y = 100$ km, $\tau = 1500$ seconds for 3000 steps to get approximately 4 heating cycles in a total time of 6000 seconds. Figure 3.3 shows the $y - z$ structure of the amplitude of the heating function, Q, at the time of 6000 seconds. It complies with equation (3.52), set up as two full wavelengths in the horizontal direction along with a half sine wave in the vertical (the plots are of the amplitudes so the values are all positive).

Figures 3.5a and 3.5b show "z *vs* time" plots of the amplitude and phase of u'_k respectively at a particular latitude. We see from the phase diagram, Fig. 3.5b, a steady

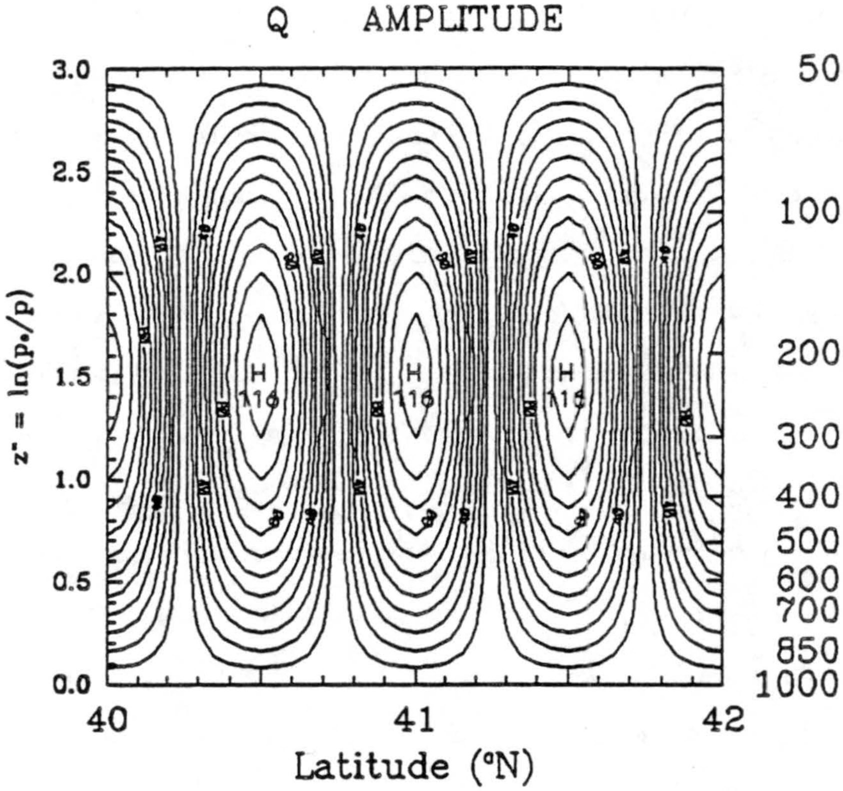

Figure 3.3: Amplitude for the heating function, Q, for case given in Fig. 3.2a (in K/seconds). Shows 2 cosine waves in y and 1/2 sine wave in z^*. Contour interval of 0.1×10^{-5}. Labels scaled by 0.1×10^{8}.

(a)

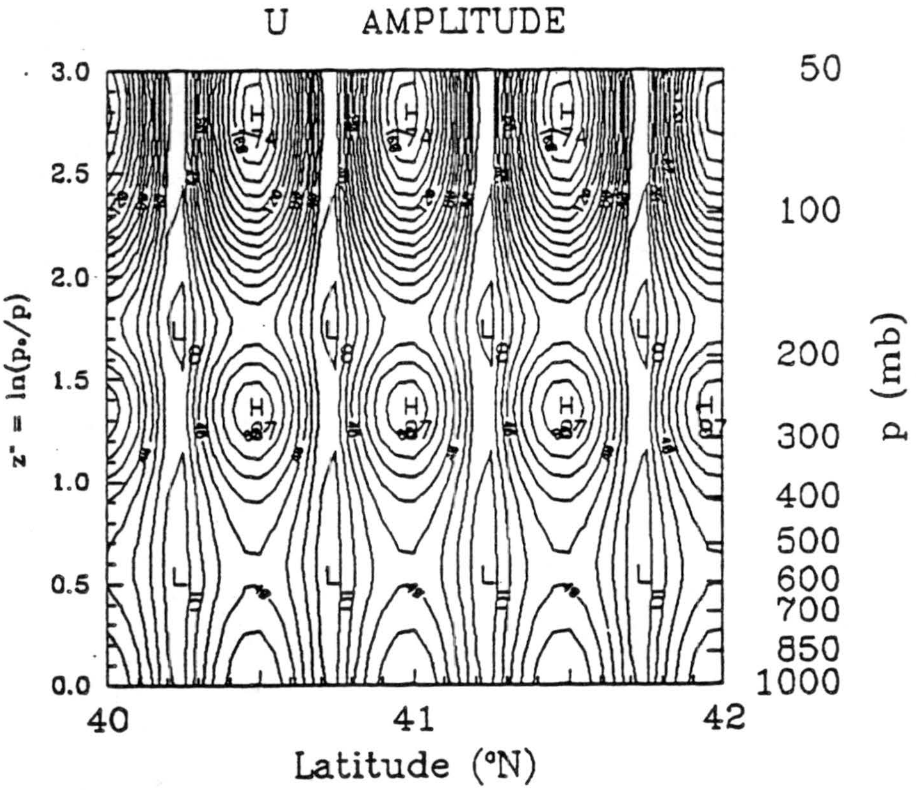

Figure 3.4: (a) Amplitude for u' (in ms^{-1}). Same as Fig. 3.2a except the time step in now numerically stable. $\Delta t = 2$ seconds. $t = 6000$ seconds. Contour interval of 0.1×10^{-3}. Labels scaled by 0.1×10^{6}.

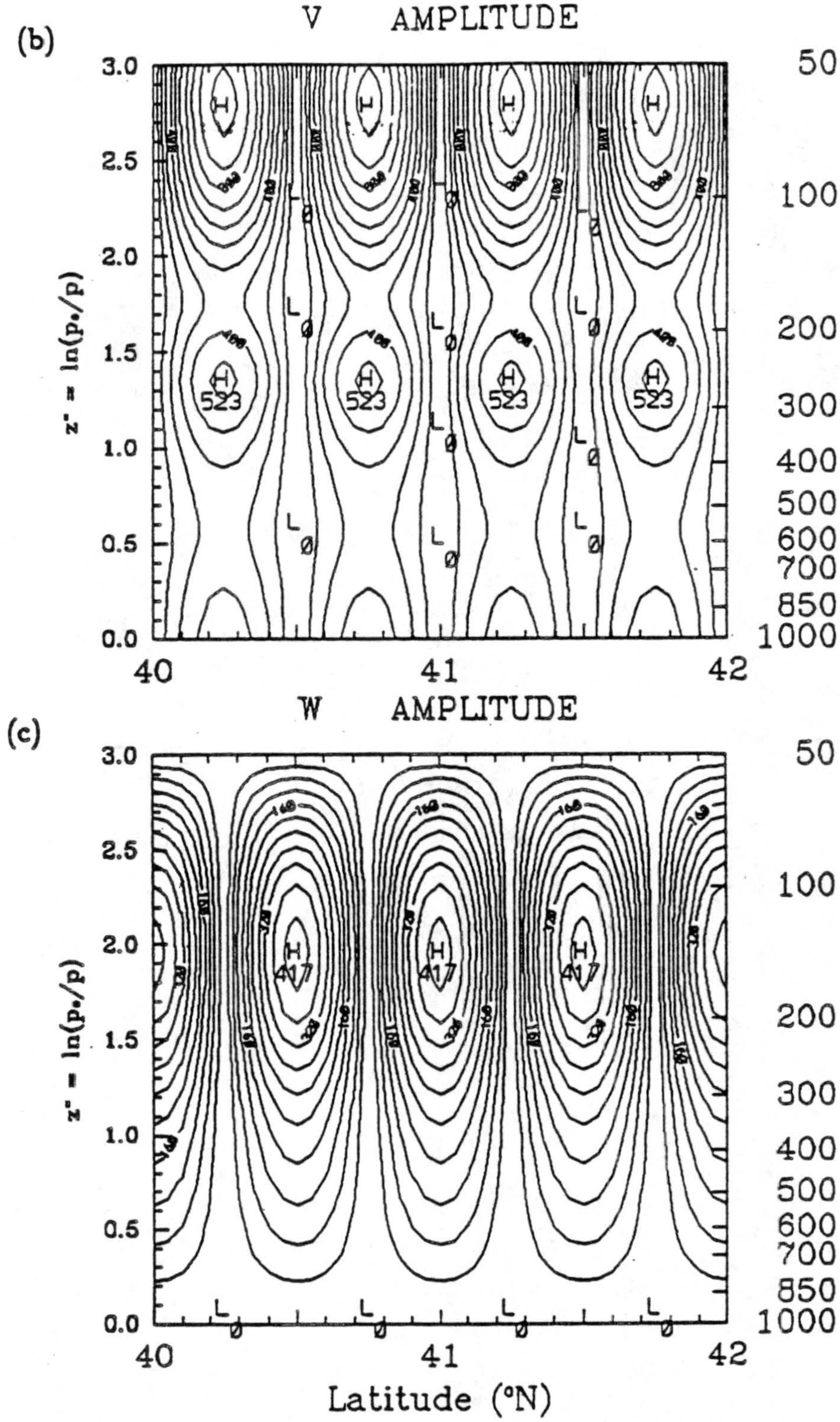

Figure 3.4: (b) Same as Fig. 3.4a except for v' (in ms^{-1}). Contour interval of 0.1×10^{-2}. Labels scaled by 0.1×10^{6}. (c) Same as Fig. 3.4a except for w' (in s^{-1}). Contour interval of 0.4×10^{-7}. Labels scaled by 0.1×10^{10}.

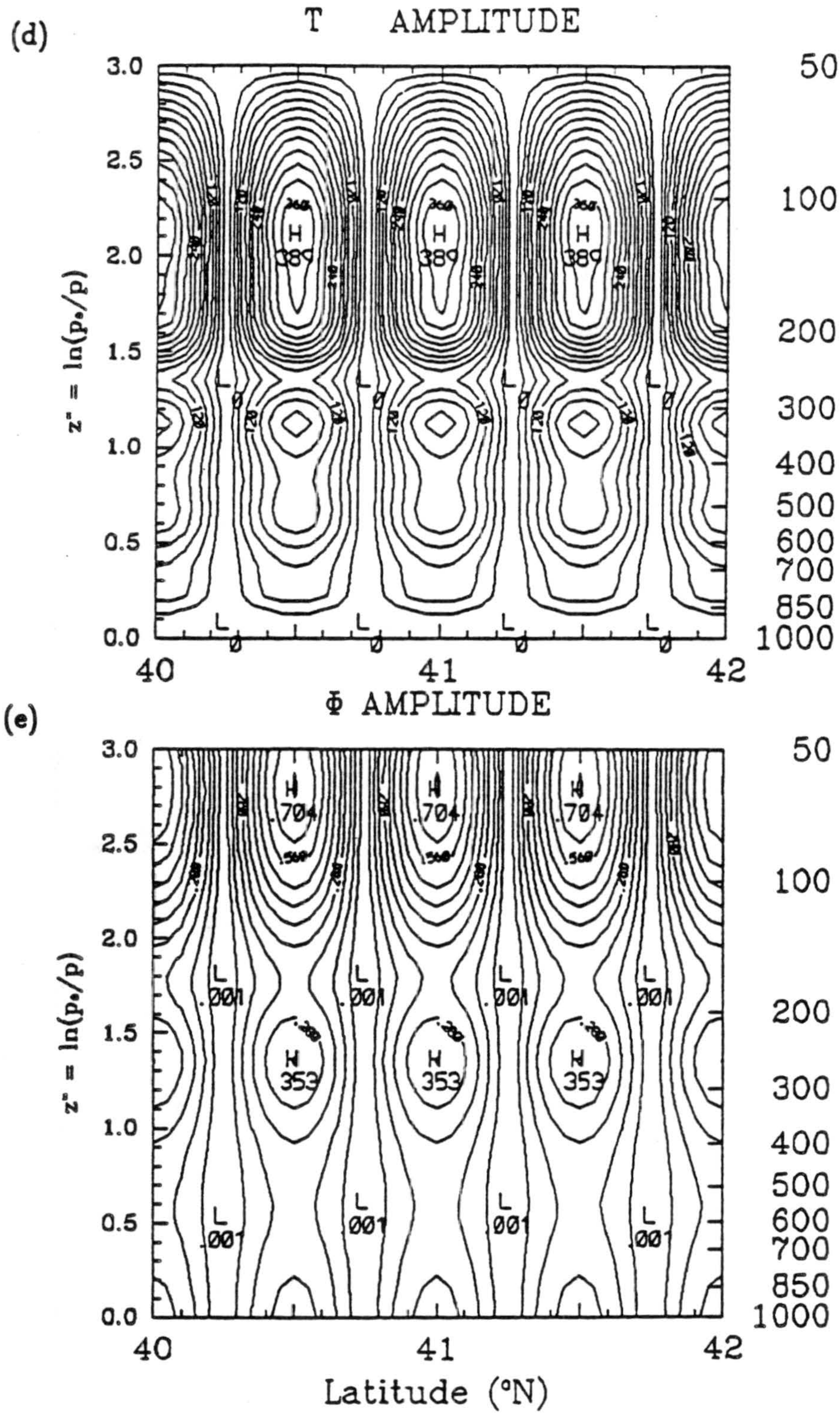

Figure 3.4: (d) Same as Fig. 3.4a except for T' (in K). Contour interval of 0.3×10^{-3}. Labels scaled by 0.1×10^{6}. (e) Same as Fig. 3.4a except for ϕ' (in m^2s^{-2}). Contour interval of 0.7×10^{-1}.

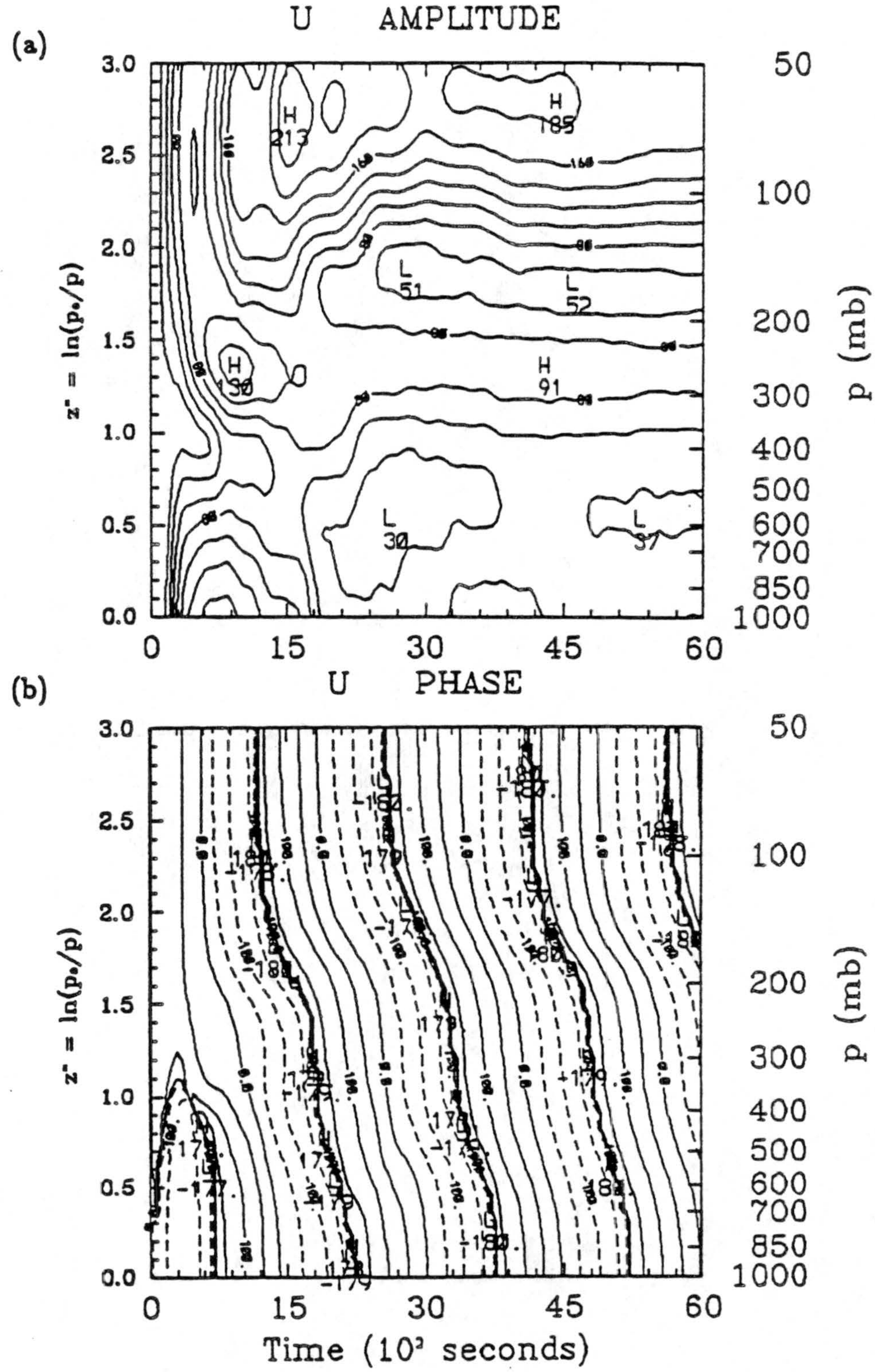

Figure 3.5: (a) Amplitude for u' (in ms^{-1}). The vertical profile of u' at $y = 3/4 * L_2$, an antinode for u, at specified time intervals from $t = 0$ to 6000 seconds. For case given in Fig. 3.4a. Contour interval of 0.2×10^{-3}. Labels scaled by 0.1×10^{6}. (b) Same as Fig. 3.5a except for the phase of u' at the same antinode. Contour interval of 50°.

oscillating pattern take shape after a short time with a period, $\tau = 1500$ seconds, which is what we originally expected. From the amplitude plot, Fig. 3.5a, we see how, in this case u'_k, starts from zero and grows from the heating function then adjusting to the other variables in its prognostic equation. And after the variable settles into a steady oscillation, the amplitude values straighten out over time as expected, happening over approximately $1\frac{1}{2}$ periods of heating. All the other variables have similar actions as u'_k. Figure 3.5b also shows how u'_k changes sign from the upper to lower domain.

Figures 3.4a through 3.4e are the "$y - z$" plots of the five perturbation variables at the final time of 6000 seconds. These are made after the variables have been given time to settle into their steady oscillations. Now we can compare these diagrams according to how the variables should be interact to each other with consideration to the conditions we set. By comparing the magnitudes of the terms in the momentum equations, we see that the term involving ϕ'_k is the dominating term for both u'_k and v'_k thus we expect u'_k and v'_k to look the similar to ϕ'_k, except v'_k contains the horizontal derivative of ϕ'_k so we see the horizontal maximum correspond to the largest gradients in ϕ'_k. We get two complete waves in y for v'_k and we get $v'_k(y = 0, L_2) = 0$. The hydrostatic equation gives us ϕ'_k from temperature so we expect ϕ'_k to resemble the vertical derivative of the T' field. We see ϕ'_k having the same horizontal structure as T'_k while vertically, ϕ'_k maxima coorespond to the temperature's largest vertical gradient. Plus we see the lower boundary of ϕ'_k to be very small as the lower boundary condition goes. The controlling term in the thermodynamic equation which dominates the heating term above the tropopause after a short time is $w'_k\Gamma(z^*)$ (vertical velocity and static stability). The two maxima in the vertical for T'_k come from the relationship of w'_k to Γ above the tropopause and from Q below. We see the large gradient at the tropopause cooresponding to the large change in Γ there, while the horizontal structure is similar to Q. Looking at w'_k, we see the top boundary condition of $w'_k = 0$ and the lower boundary condition, $W = 0$, we expect to cause w'_k to approximate zero in time, which it does. Its vertical structure comes from it being a vertical derivative of the convergence while its horizontal structure is like the convergence horizontal structure. We also see the two terms of the convergence equation, iku'_k and $\frac{\partial v'_k}{\partial y}$, are the same order of magnitude.

In this section, we observed how the variables interact to changes in the other variables and learned of the major problems we need to deal with to make a successful model run. This of course was a simplified set of primitive equations; our next cases will have more terms in the equations thus making similar comparisons as above more difficult.

Chapter 4

RESULTS

In this section we use our model to show how perturbations to a two-dimensional basic state consisting of different jet configerations respond to inertially unstable conditions. For these basic states, the growth rates (σ_i) and phase speeds (c_r) as functions of zonal wavenumber (s) are computed and compared. The first case we consider a jet with horizontal wind shear but no vertical shear. This case is similar to the work shown earlier in this paper and by SC using the shallow water equations. The second case uses a jet with vertical shear but no horizontal shear. This basic state is similar to those used by Stone (1966), Emanuel (1979), and Nehrkorn (1986), except theirs had constant vertical shear while ours varies with height. The third case involves a jet with variable horizontal and vertical wind shear.

4.1 Horizontal Wind Shear Only

We first consider our two-dimensional jet to have variable horizontal wind shear but no vertical shear, as shown in Fig. 4.1a. We use the same parameters as used in the shallow water model Section 2.3 and in SC, a Bickley jet profile with magnitude $u_o = 75$ ms^{-1}, a half-width $Y_B = 3°$, and the jet centered at $Y_A = 45°$N. The condition for inertial instability is seen in Fig. 4.1b, where the potential vorticity is negative. For this case with $\bar{u}(y)$, the horizontal shear term $(f\bar{\eta})$ of the potential vorticity is the only term used from equation (1.1). This unstable region follows exactly that of the shallow water model case in Chapter 2 (Fig. 2.2b). The basic state temperature field, Fig. 4.1c, is only dependent on z^* since without vertical wind shear the thermal wind relation implies no y dependence for T.

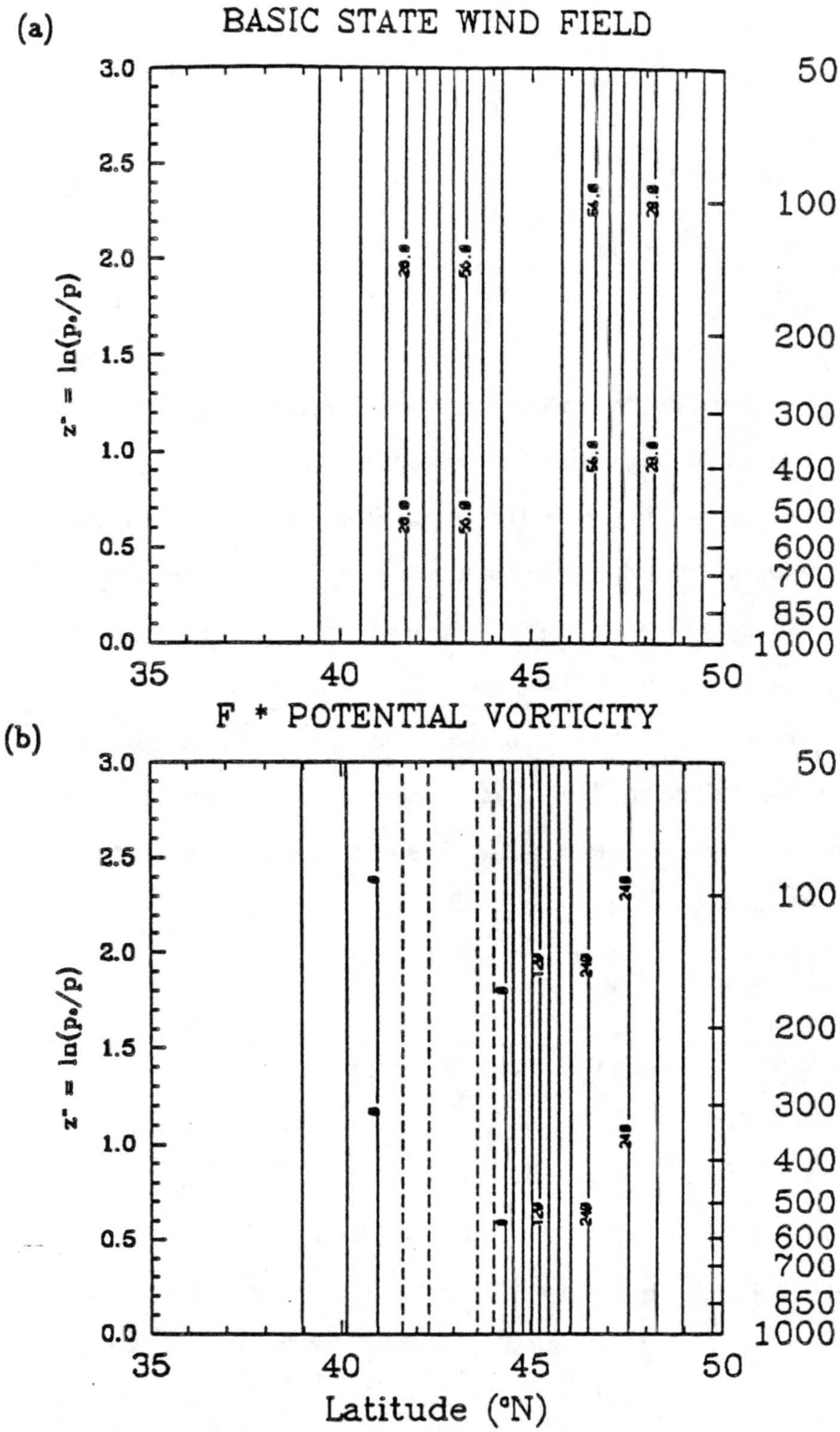

Figure 4.1: (a) Midlatitude Bickley jet (in ms^{-1}) in the meridional direction only. $u_o = 75$ ms^{-1}, $Y_A = 45°N$, $Y_B = 3°$. Contour interval of 7.0. (b) Potential vorticity times Coriolis parameter, $f \cdot \bar{P}$, (in s^{-2}). Here the condition for inertial instability is where $f \cdot \bar{P} < 0$. For jet profile in Fig. 4.1a. Maximum value of $-f\bar{P}$ = -0.8 $\times$ 10^{-8}. Contour interval of 0.3 $\times$ 10^{-8}. Labels scaled by 0.1 $\times$ 10^{11}.

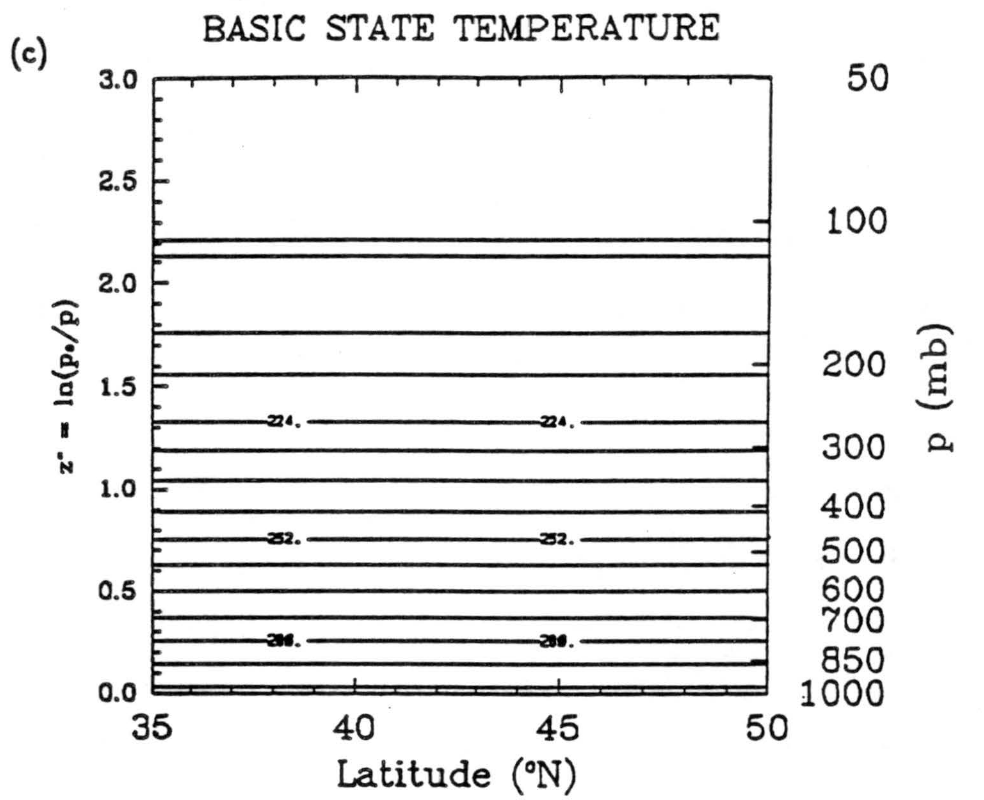

Figure 4.1: (c) Basic state temperature (in K), for jet profile in Fig. 4.1a, using $T_o(z^*)$ in Fig. 3.1b. Contour interval of 7.0.

In order to compare these results to those of SC, we need to find a relationship between this set of primitive equations and the shallow water equations. We use the separation of variables technique on the linearized primitive equations with $\bar{u}(y)$. Assuming normal mode solutions, $u' = u_1(y, z)e^{i(kx-\sigma t)}$, we come up with the horizontal and vertical structure equations equal to a separation constant. This horizontal structure equation along with the momentum equations give us a direct comparison to the shallow water equations and we get a value for the separation constant, $K = \frac{1}{gH}$, where H is the equivalent depth of the shallow water system. From the solution to the vertical structure equation using our upper and lower boundary conditions along with the values for the separation constant, we get a relation between the vertical scale of the primitive equation to the equivalent depth of the shallow water system,

$$\frac{1}{H} = \frac{g}{R\Gamma}\left(\frac{n^2\pi^2}{D^2} + \frac{1}{4}\right) \tag{4.1}$$

where n is the number of nodes in the vertical scale for the primitive equations.

The results for this case are very similar to those from the shallow water model runs. We see in Fig. 4.2, for $s = 6$, the time it takes for the most unstable mode to become dominant is on the order of 70,000 seconds which is approximately the same as in Fig. 2.1a. Figures 4.3a and 4.3b show growth rates and phase speeds respectively over a range of wavenumbers from $s = 0$ to 14. From these figures one can note a decline in the growth rates as the wavenumber increases, after being relatively constant over the first couple wavenumbers. One might expect such results in the growth rates since the vertical scale of this system corresponds to an equivalent depth of approximately 3.1 meters. These results are consistent with those of SC for similar values of H, as shown in Fig. 2.4 (SC figure). The phase speed diagram also follows the SC results; in looking at Fig. 4.3b, we note that the phase speeds increase with s and the magnitudes are similar. From Fig. 4.3a, the growth rates of asymmetric modes are comparable to that of the symmetric mode. Assuming inertial instability is symmetric is thus a poor assumption with horizontal wind shear in a stratified atmosphere.

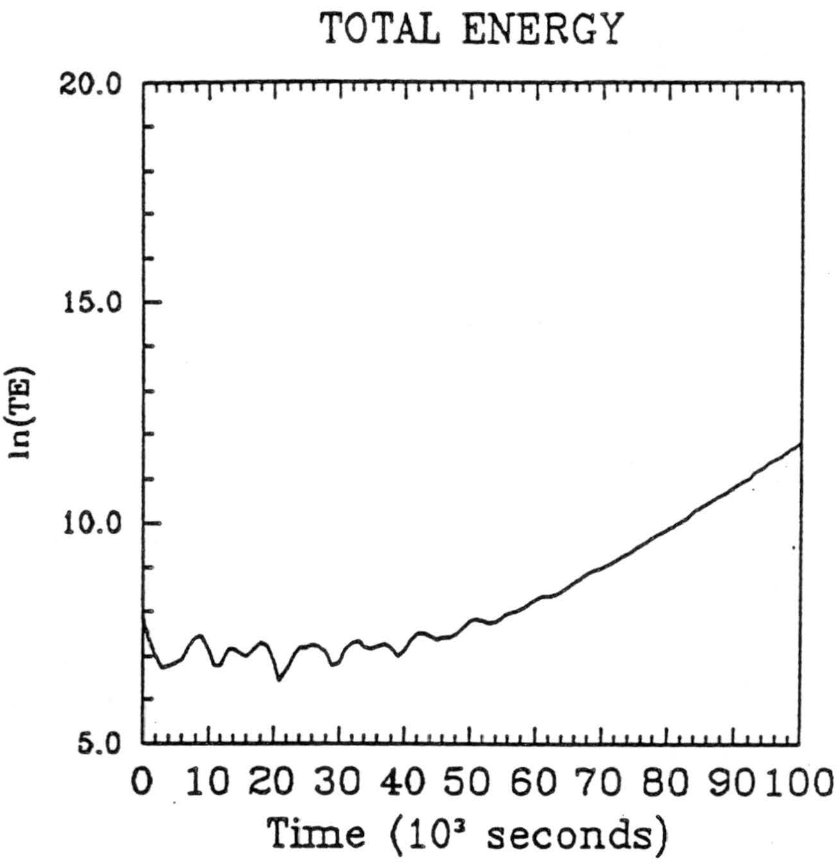

Figure 4.2: Growth of log of total energy from $t = 0$ to 100,000 seconds. For jet profile in Fig. 4.1a. Meridional and vertical average of total energy. For $s = 6$.

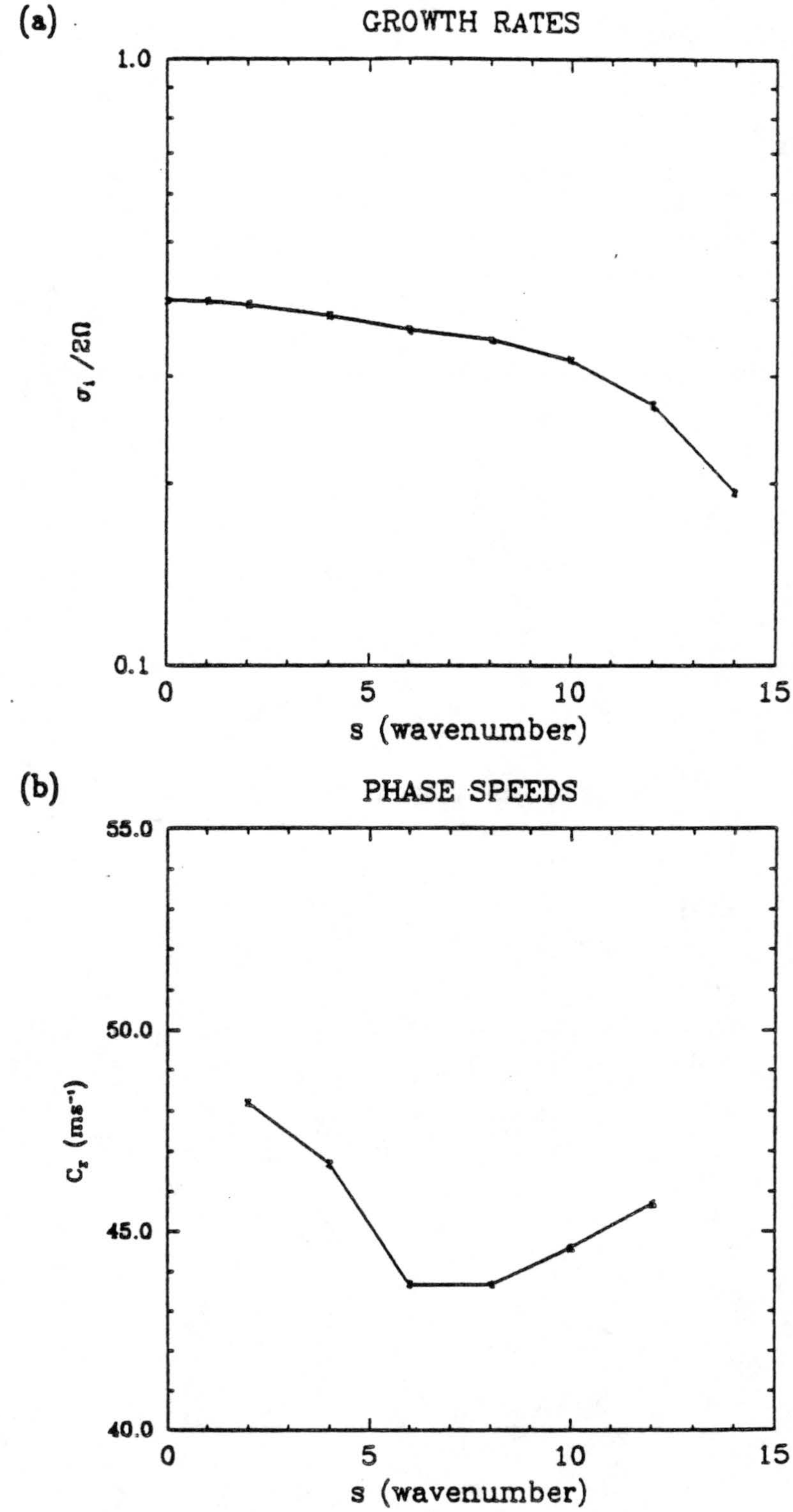

Figure 4.3: (a) Growth rates (σ_i) versus s, same as Fig. 2.3a except for jet profile in Fig. 4.1a. For various wavenumbers. Corresponds to shallow water equivalent depth of $h =$ 3.15 meters. (b) Phase speeds c_r in (in ms^{-1}) versus s, same as Fig. 2.3b except for jet profile in Fig. 4.1a. For various wavenumbers.

(a)

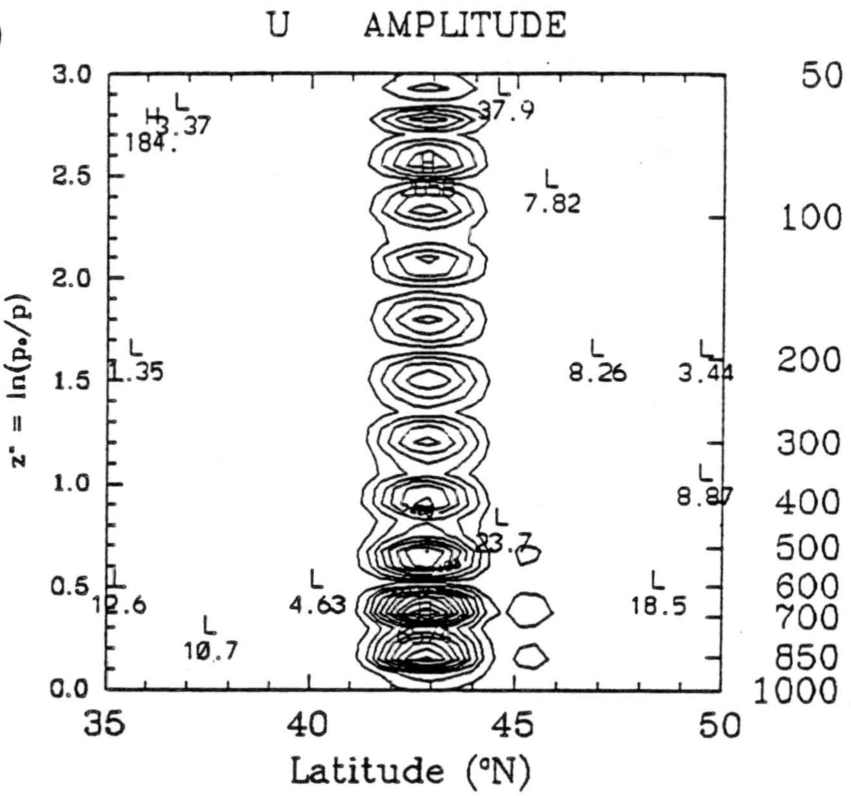

Figure 4.4: (a) Amplitude for u' (in ms^{-1}) at t = 200,000 seconds. For jet profile in Fig. 4.1a, $s = 6$. Contour interval of 600.

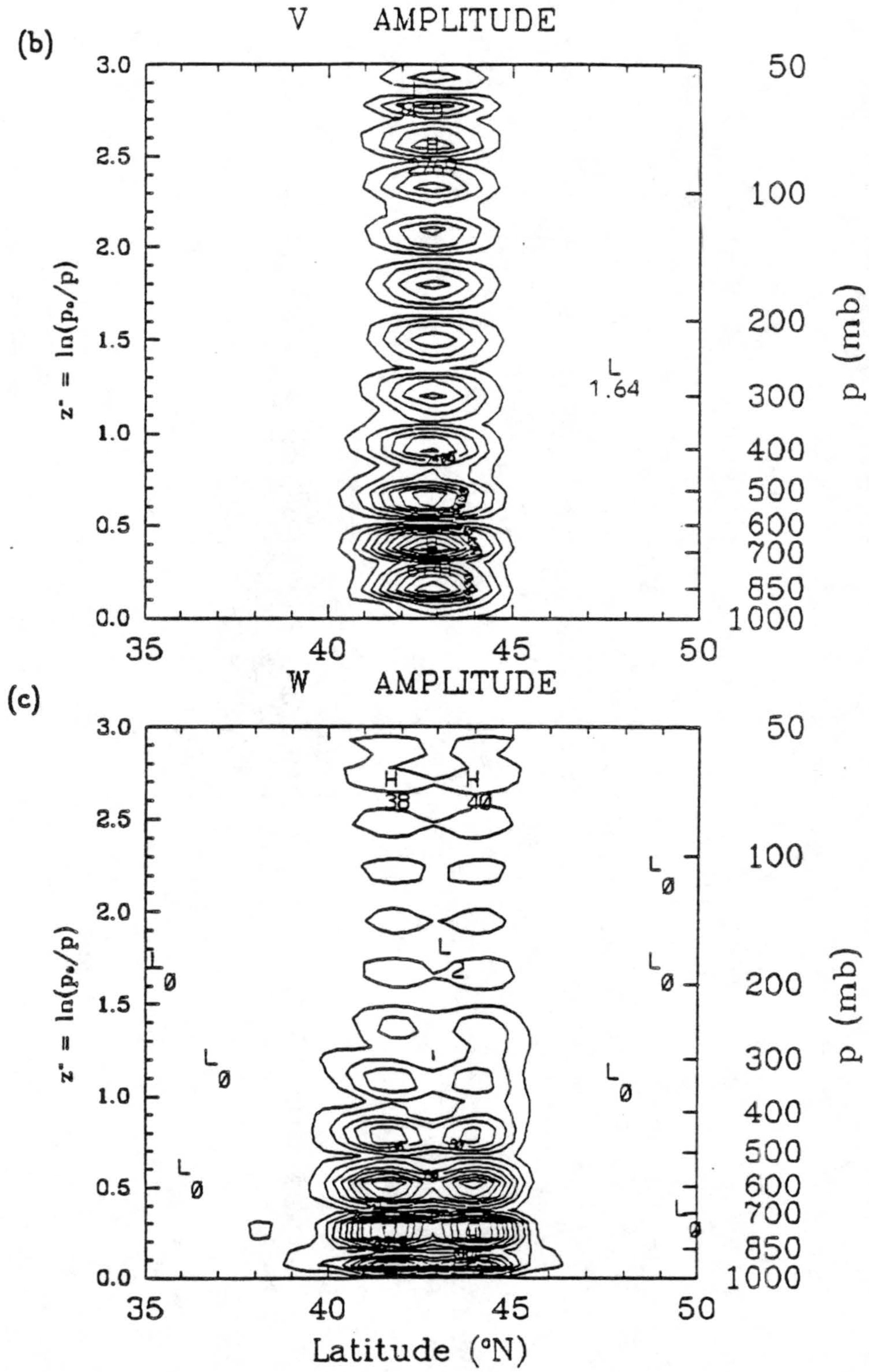

Figure 4.4: (b) Same as Fig. 4.4a except for v' (in ms^{-1}). Contour interval of 600. (c) Same as Fig. 4.4a except for w' (in s^{-1}). Contour interval of 0.2×10^{-3}. Labels scaled by 0.1×10^{6}.

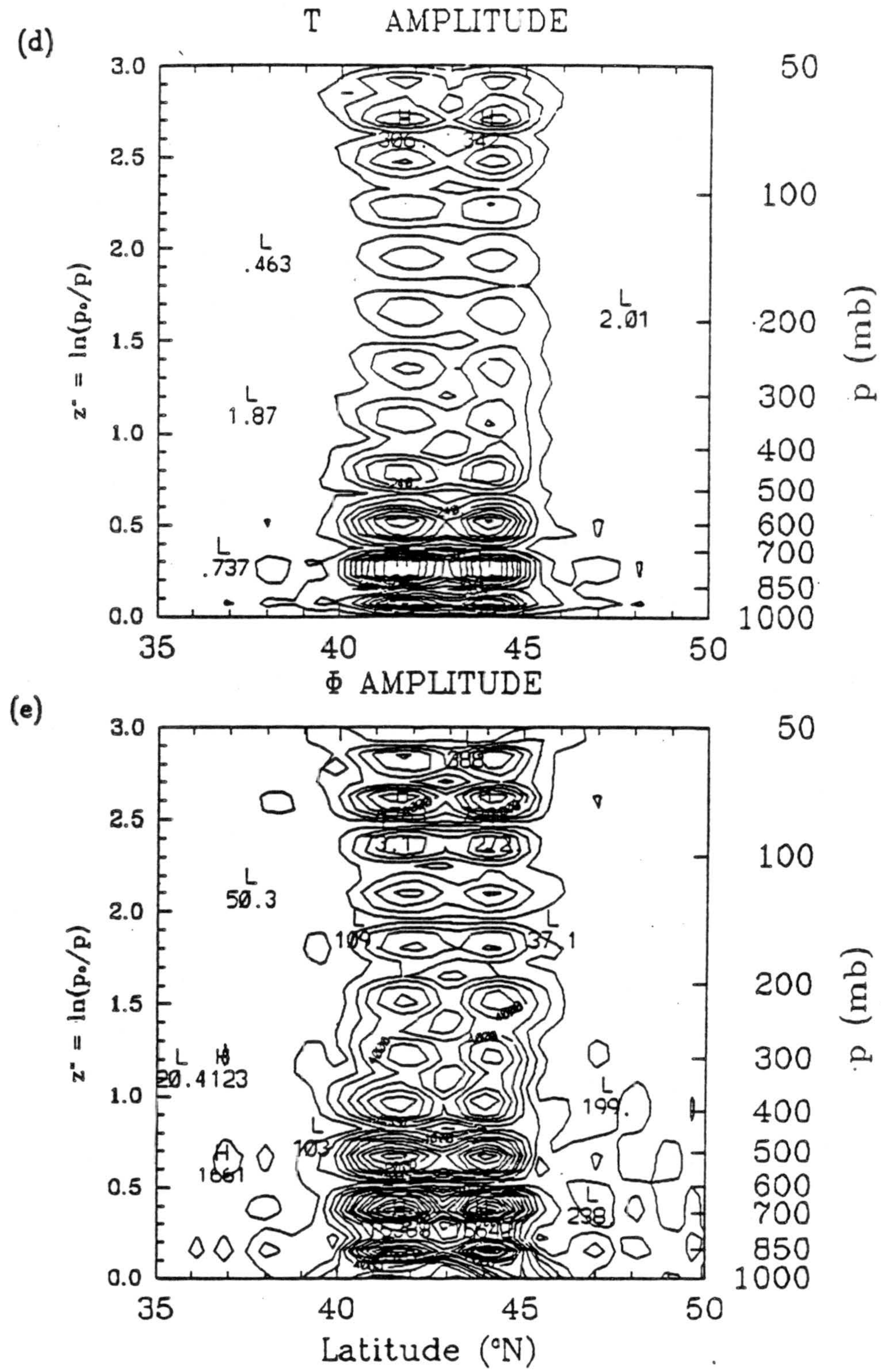

Figure 4.4: (d) Same as Fig. 4.4a except for T' (in K). Contour interval of 60. (e) Same as Fig. 4.4a except for ϕ' (in m^2s^{-2}). Contour interval of 1000.

The resulting perturbation variables for $s = 6$ at $t = 200{,}000$ seconds can be seen in Figs. 4.4a through 4.4e. Horizontal cross sections of u', v', ϕ' are similar to those for the shallow water system (Figs. 2.5a - 2.5c). We see the momentum perturbation fields develop within the unstable region of the jet. The u' maximum has developed at just less than 43°N and same for v', with v' having a larger y scale as expected from the shallow water results; ϕ' follows as it shows two maxima in the horizontal direction located at 41°N and 44°N, as in SC. We see that T' has its maxima in height at the nodes of ϕ' as the hydrostatic equation requires. Finally we note that w' is zero at the top and has become zero at the bottom but the upper boundary condition on w' doesn't matter since w' is small there.

4.2 Vertical Wind Shear Only

Now we set up our two-dimensional jet to have vertical wind shear and no horizontal shear. We again use similar parameters as in the horizontal shear case; the magnitude of the jet, $u_o = 75$ ms^{-1}, and the Bickley jet profile in the vertical direction. We set the jet center to $Z_A = 1.5$ (~220mb). With this configuration, we alter the vertical half-width, Z_B, of the jet to set up a region of negative potential vorticity according to the vertical wind shear. This turns out to be a difficult task if we require stable stratification throughout the domain we have been using. We find that two areas within our domain are especially sensitive to the different wind shears we try, one area being near $z^* = 1.2$ at the left (southern) end of our domain and the second around $z^* = 0.7$ at the right (northern) end of our domain. What happens is that the Brunt Väisälä frequency (N^2) due to the horizontally varying ($T_1(y, z)$) part of $\bar{T}$ approaches a negative value of the same magnitude of N^2 due to the $T_o(z)$ part of $\bar{T}$. Therefore, N^2 gets very small on either side of zero in these regions causing the vertical shear term of the potential vorticity (f^2/Ri) to become very large. This results in static instability which is not the focus of our current problem. The cause of this comes from our original assumption of the basic state temperature field. In many studies, (e.g. Stone, 1966, Emanuel, 1979, Fulton and Schubert, 1985) the static stability is considered constant in height with no horizontal variation. Now, what we have found is that when we have static stability that not only depends on height but also varies horizontally, inertially unstable regions due to the vertical wind shear are limited by the size of the horizontal domain because of static instability. Using our current domain size, 1665 km ($\sim 15°$ latitude), we were not able to set up an inertially usntable region large enough, or strong enough to be condusive for anything to develop. It is our contention that using the geostrophic balance assumption in computing $\bar{T}$, makes the static stability variable in the horizontal direction, so that the vertical wind shear can never be large enough to be the dominant cause of inertial instability because it will go statically unstable first. We find out later in the case with $\bar{u}(y, z^*)$ that the curvature of the jet makes the two sensitive areas mentioned above less sensitive as the vertical shear is greatest in a small region directly above and below the jet core. So in that case, the vertical shear term can have an effect on the inertial instability.

To see if we could get a vertical shear case, we assumed $\bar{T}$ to be only a function of z^* in the static stability term. The derivative of $\bar{T}$ with respect to y is derived from the thermal wind balance. The system is now statically stable, $\Gamma(z^*)$, and we are able to set up the jet parameters to achieve a region of negative potential vorticity with the domain 1665 km. The jet, with a half-width of $Z_B = 0.6$, is shown in Fig. 4.5a. And the region that is inertially unstable is shown in Fig. 4.5b as negative potential vorticity. What we get with these results are very slow developing perturbations in the unstable region as seen in Fig. 4.6, approximately twice as long for the most unstable mode to become dominant (approximately 150,000 seconds) as compared with the case of horizontal shear. The growth rates we get are very small (approximately one fifth) compared to that due to the horizontal shear term showing the dominance of the horizontal part over the vertical part. And we get larger wave numbers to have larger growth rates affirming that for vertical shear, inertial instability is asymmetric, not symmetric.

From Figs. 4.7a through 4.7e, we see the perturbation fields that have developed due to the vertical shear term. We see that they have grown in the inertially unstable region below the jet center with some overlap. We see on u' and v', large horizontal scales for the disturbances and especially in v', a tilt on the maxima. And notice that after t

(a)

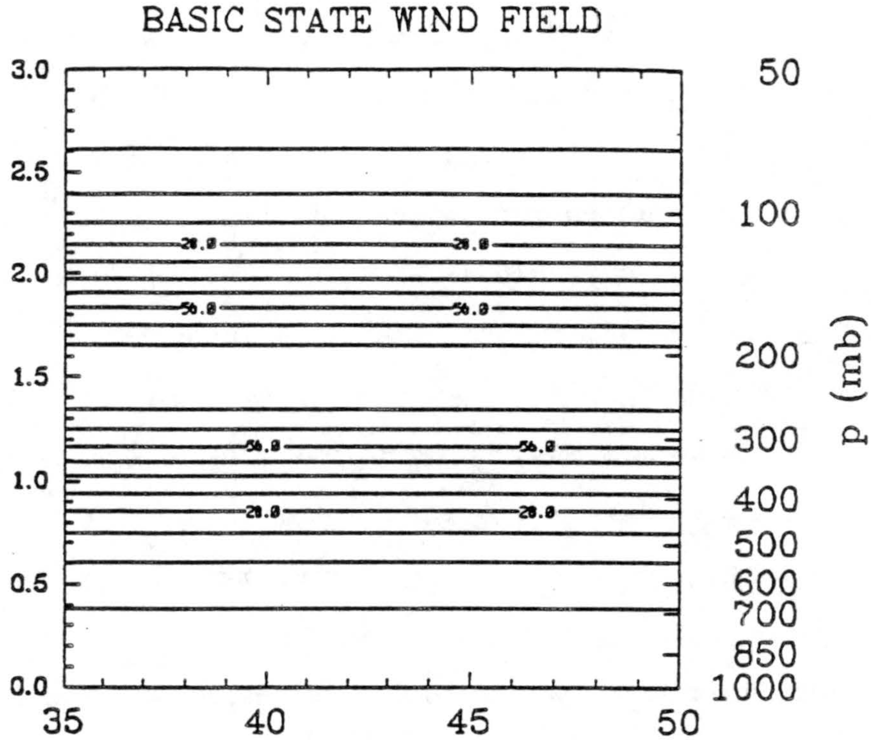

(b)

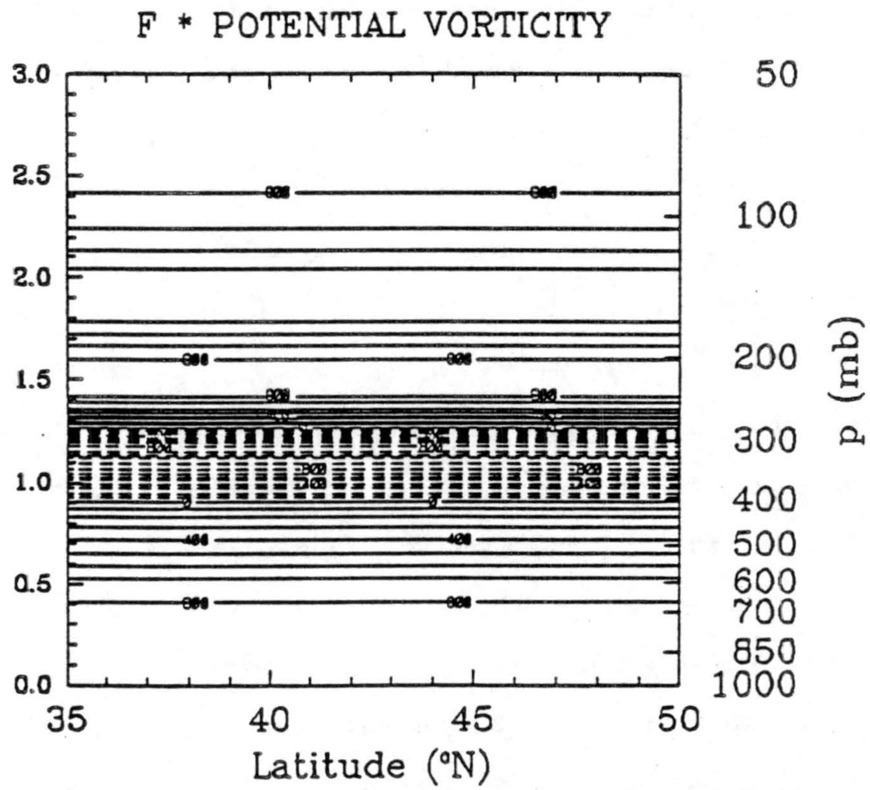

Figure 4.5: (a) Midlatitude Bickley jet (in ms^{-1}) in the vertical direction only. $u_o = 75$ ms^{-1}, $Z_A = 1.5$, $Z_B = 0.6$. Contour interval of 7.0. (b) Potential vorticity times Coriolis parameter, $f \cdot \bar{P}$, (in s^{-2}). Condition for inertial instability is where $f \cdot \bar{P} < 0$. For jet profile in Fig. 4.5a. Static stability is a function of only $z^*, \Gamma(z^*)$. Contour interval of 0.1 $\times 10^{-8}$. Labels scaled by 0.1×10^{12}.

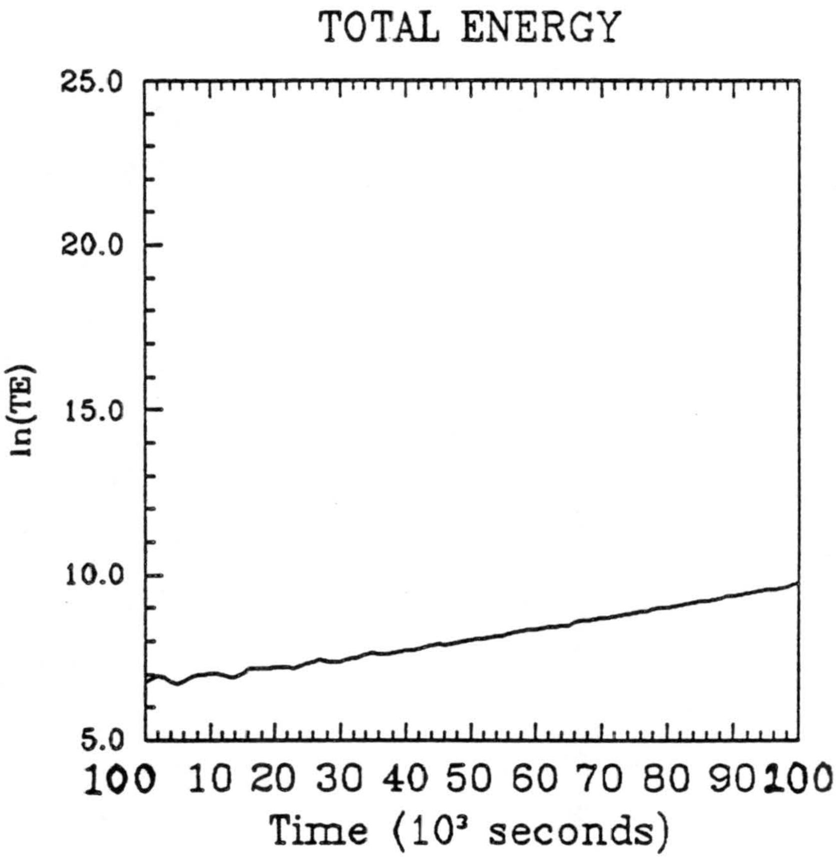

Figure 4.6: Same as Fig. 4.2 except for jet profile in Fig. 4.5a. From t = 100,000 to 200,000 seconds.

(a)

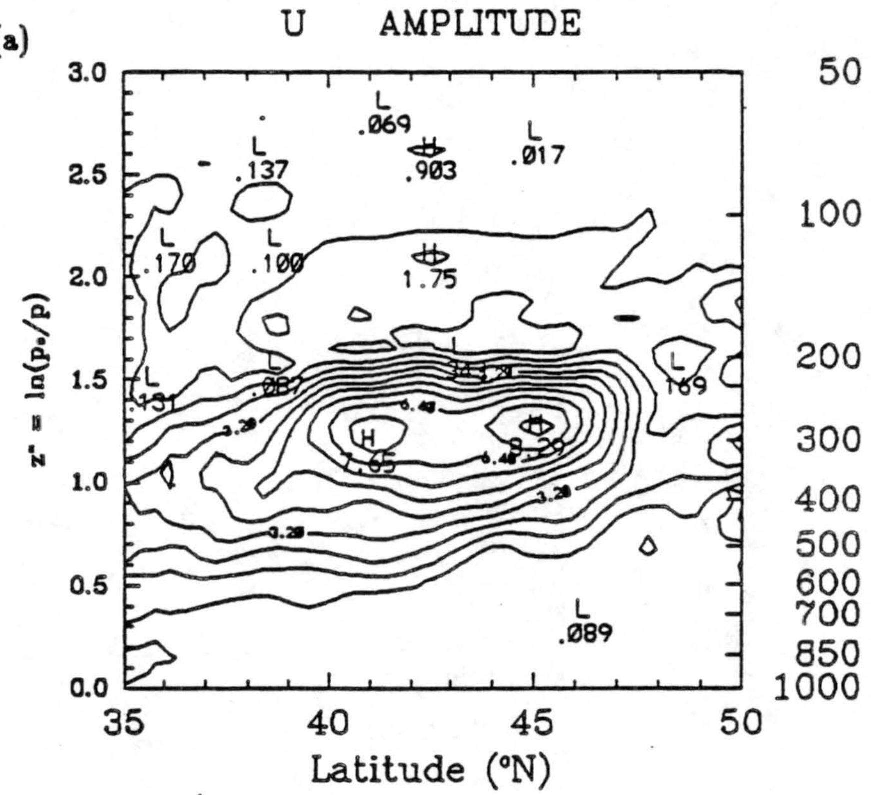

Figure 4.7: (a) Amplitude for u' (in ms^{-1}) at t = 200,000 seconds. For jet profile in Fig. 4.5a, $s = 6$. Contour interval of 0.8.

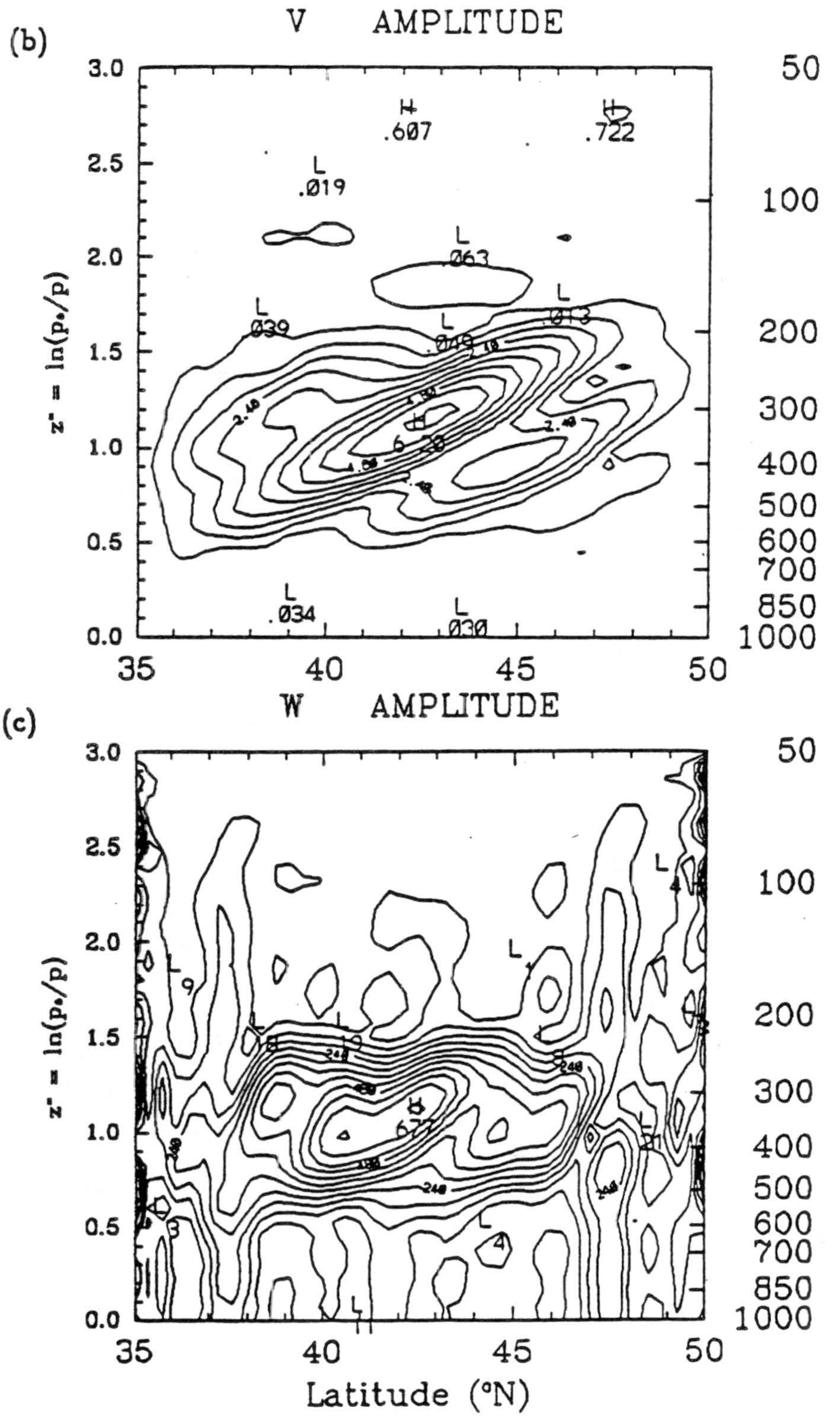

Figure 4.7: (b) Same as Fig. 4.7a except for v' (in ms^{-1}). Contour interval of 0.6. (c) Same as Fig. 4.7a except for w' (in s^{-1}). Contour interval of 0.6×10^{-6}. Labels scaled by 0.1×10^9.

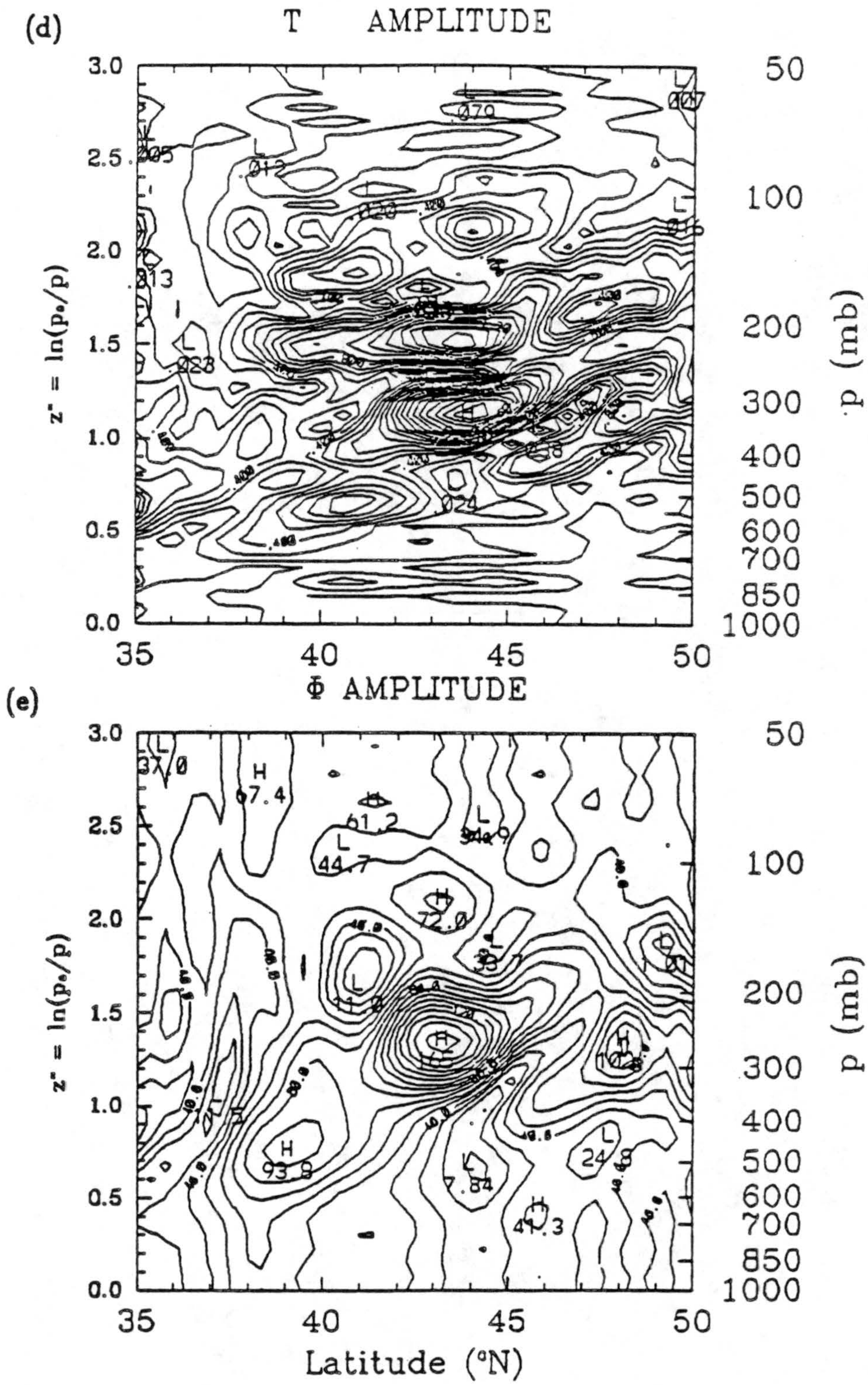

Figure 4.7: (d) Same as Fig. 4.7a except for T' (in K). Contour interval of 0.1. (e) Same as Fig. 4.7a except for ϕ' (in m^2s^{-2}). Contour interval of 10.

= 200,000 seconds, the magnitudes are still very small, again telling us the difficulty the vertical shear term has in causing inertial instability.

We tried a smaller domain 333 km ($\sim 3°$ latitude) using the same parameters of the vertical sheared jet case with the horizontal variation in $\Gamma(y, z^*)$ in order to avoid the two sensitive regions described above. We are able to get a region of negative potential vorticity, seen in Fig. 4.8, that would seem to be able to excite an unstable mode but we found no modes developed after 85 hours in time. We also tried this size domain using $\Gamma(z^*)$ only and found nothing developed. Therefore the smaller scale disturbances show no discernable growth due to inertial instability.

4.3 Two-Dimensional Wind Shear

In this section we consider a jet that has variable wind shear in both the horizontal and vertical directions. We want to simulate the observational case studied by Ciesielski, *et al.* (1988; hereafter refered to as PC). We specify a "bull's eye" jet, Fig. 4.9a, using the Bickley jet profile again which simulates the average physical jet. The jet is centered at $Y_A = 45°$N and $Z_A = 1.5$ (~220mb) with a magnitude of $u_o = 105$ ms^{-1} and we have set the half- widths to be $Y_B = 3°$, $Z_B = 0.7$ in order to resemble the jet observed by PC (horizontal shear = 10 ms^{-1}(100km)$^{-1}$, vertical shear = 40 ms^{-1}(100mb)$^{-1}$). We actually have more horizontal shear than PC found but that will not significantly change our results. The $\bar{T}$ we use is shown in Fig. 4.9b where we use a static stability of $\Gamma_1 = 25K$. The potential vorticity associated with this case (Fig. 4.10a) shows a large region of negative potential vorticity on the anticyclonic side of the jet. The potential vorticity separated into its contributions from horizontal and vertical shear, Figs. 4.10b, 4.10c, respectively, seems to show that the vertical shear component does add significantly to the area of negative potential vorticity but the horizontal shear part still dominates. The vertical shear component actually has a larger value than the horizontal shear term though it is directly below the jet core where the horizontal shear term has large positive values (namely, f^2). Comparing our region of negative potential vorticity with that of PC, Fig. 4.10d, we see them to be qualitatively similar. Ours is slightly different as we see a tilt

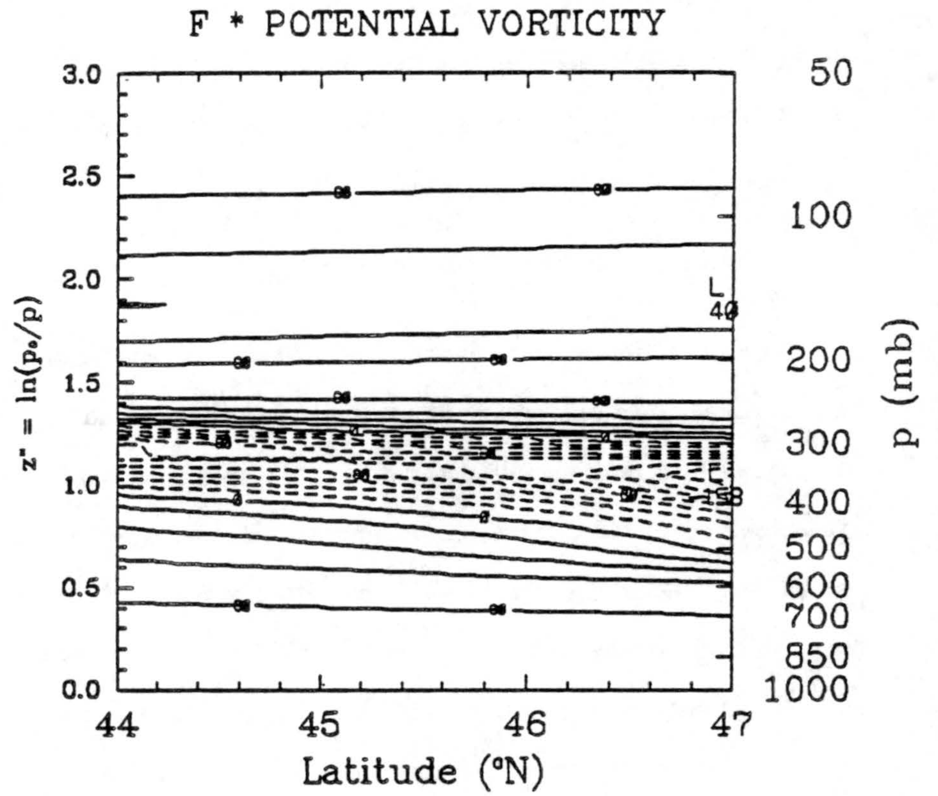

Figure 4.8: Potential vorticity times Coriolis parameter (in s^{-2}) for jet profile $u_o = 75$ ms^{-1}, $Z_A = 1.5, Z_B = 0.6$, static stability has horizontal variation, $\Gamma(y, z^*)$. For domain size 333 km. Contour interval of 0.2×10^{-8}. Labels scaled by 0.1×10^{11}.

(a)

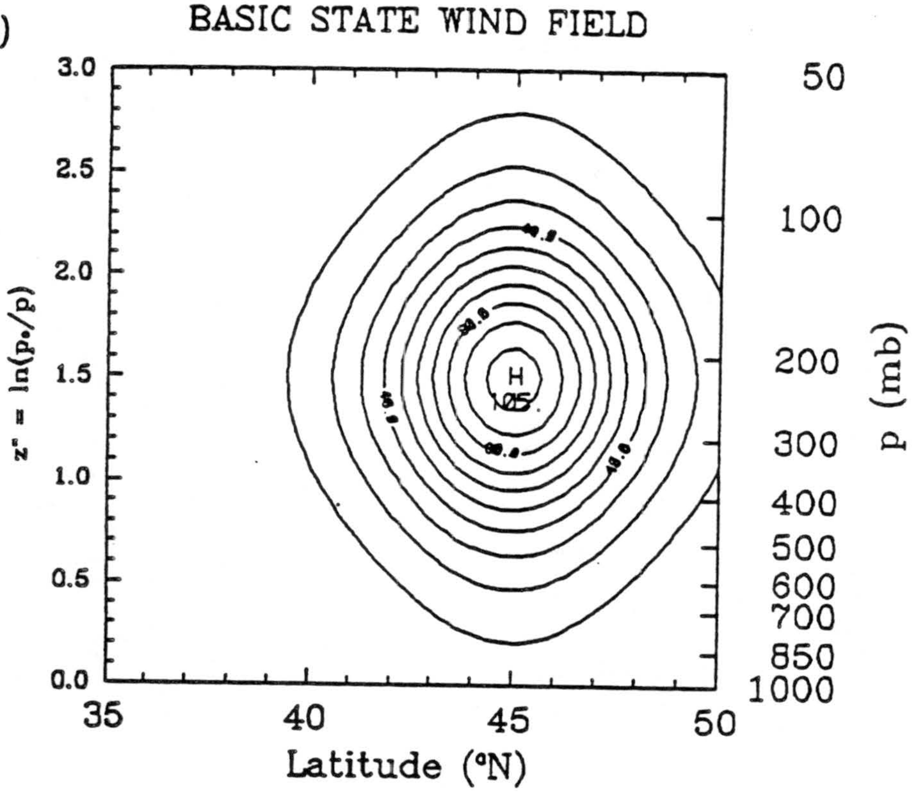

Figure 4.9: (a) Midlatitude Bickley jet (in ms^{-1}) in horiztonal and vertical directions. For jet profile $u_o = 105\ ms^{-1}$, $Y_A = 45°N$, $Y_B = 3°$, $Z_A = 1.5$, $Z_B = 0.7$. Domain size is 1665 km ($\sim 15°$ latitude). Contour interval of 10.

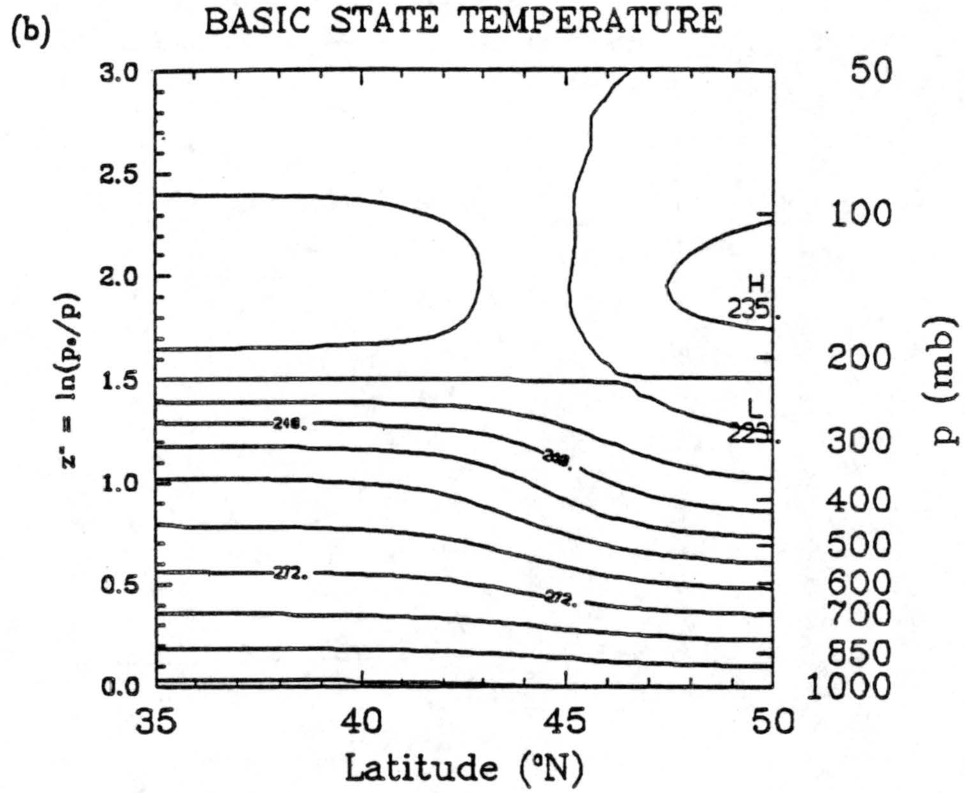

Figure 4.9: (b) Basic state temperature field (in K) for jet profile in Fig. 4.9a, uses $T_o(z^*)$ in Fig. 3.1b at 45°N. contour interval of 8.0.

(a)

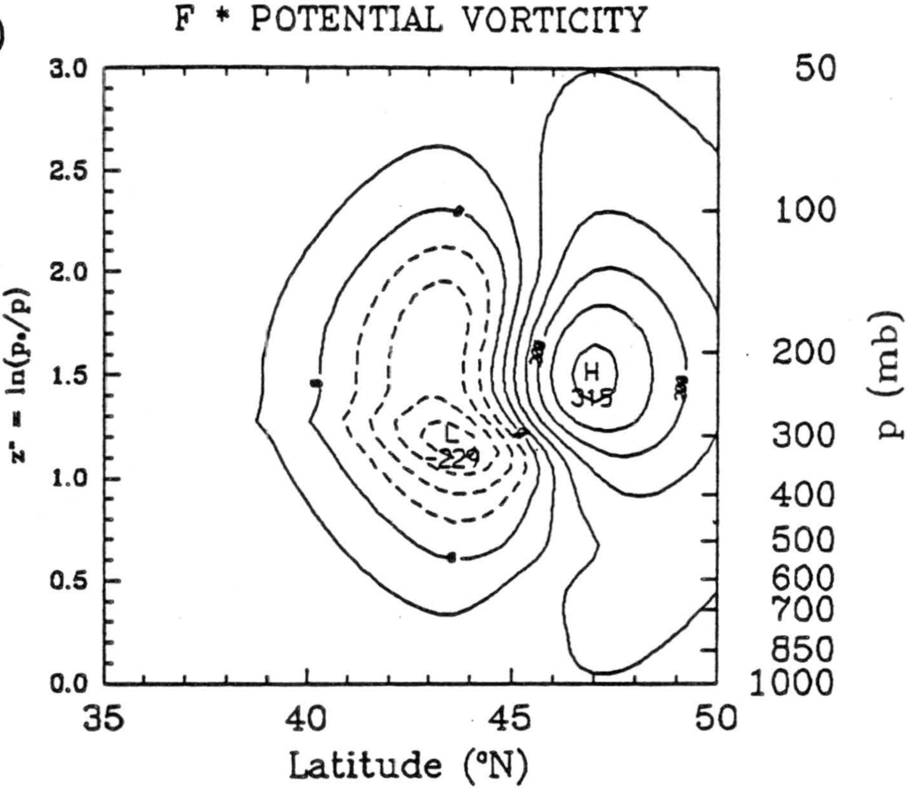

Figure 4.10: (a) Potential vorticity times Coriolis parameter (in s^{-2}) for jet profile in Fig. 4.9a. Where $f \cdot \bar{P} = f\bar{\eta} - f^2/Ri$. Contour interval of 0.5×10^{-8}. Labels scaled by 0.1×10^{11}.

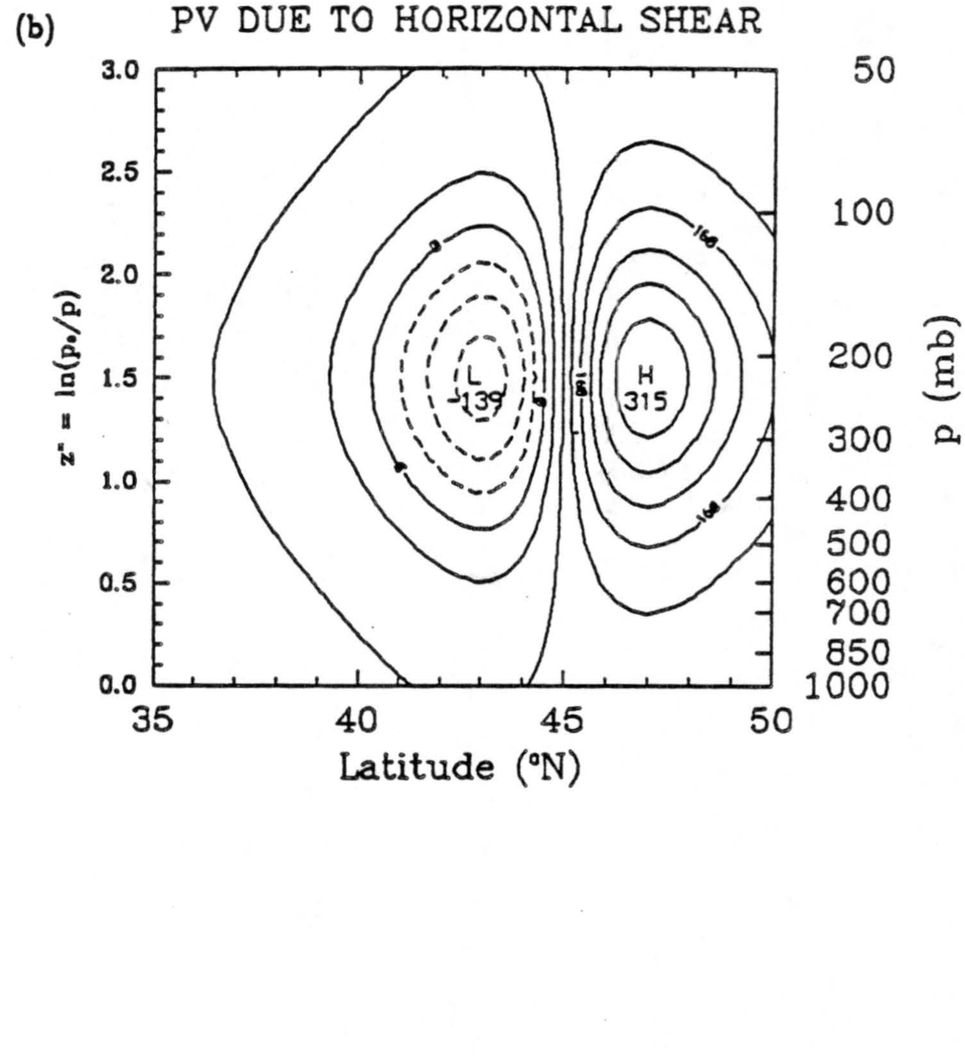

Figure 4.10: (b) Component of $f\bar{P}$ due to horizontal wind shear (in s^{-2}). This is $f\bar{\eta}$. Contour interval of 0.4×10^{-8}, labels scled by 0.1×10^{11}.

(c)

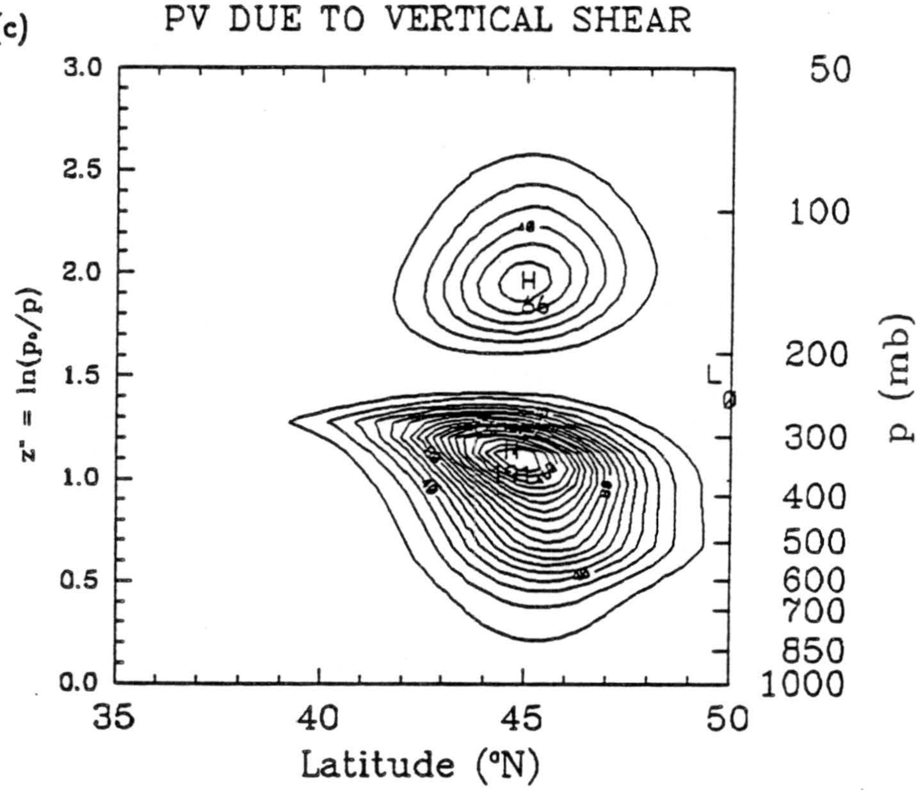

Figure 4.10: (c) Component of $f\bar{P}$ due to vertical wind shear (in s^{-2}). This is $\left(\frac{f^2}{Ri}\right)$. Contour interval of 0.1×10^{-8}. Labels scaled by 0.1×10^{11}.

(d)

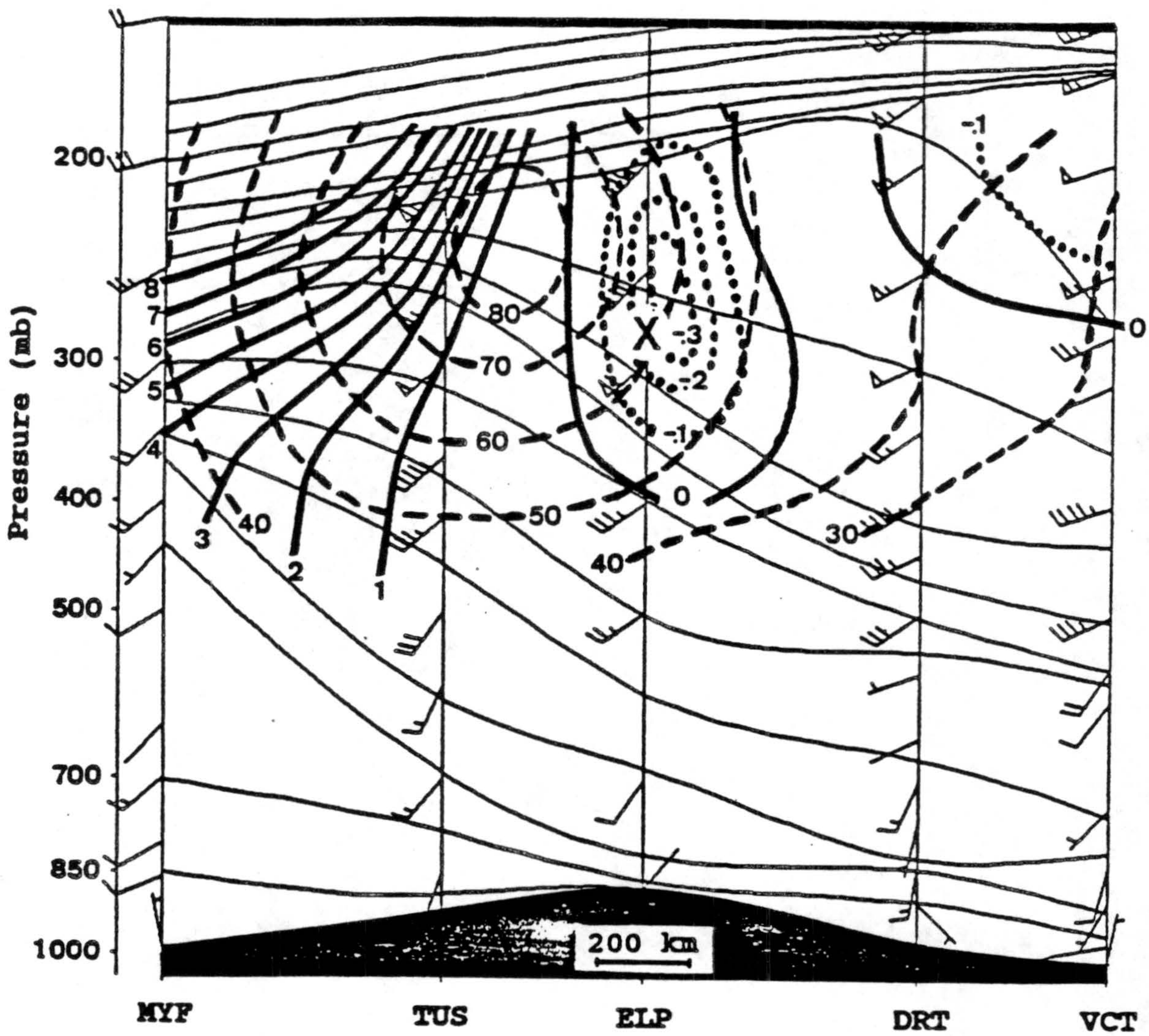

Figure 4.10: (d) Cross-section analysis of geostrophic wind speed (ms^{-1}, heavy dashed lines) at intervals of 10 ms^{-1} and potential temperature (K, thin solid lines) at intervals of 5 K for 1200 GMT, 25 February 1987. Plotted wind barbs show observed wind (ms^{-1}) for comparison to geostrophic wind speed. Analysis of potential vorticity (m^2 KKg^{-1} s^{-1}, heavy solid line for positive values at intervals of 10^6 and dotted lines for negative values at intervals of 10^5). Position of wavelets at 1800 GMT on the 25th are denoted with an 'X'. Rawinsonde soundings are from San Diego, California (MYF), Tucson, Arizona (TUS), El Paso, Texas (ELP), Del Rio, Texas (DRT), Victoria, Texas (VCT). Taken from Ciesielski, *et al.*, 1988.

in the maxima of the negative potential vorticity due to the vertical shear term. Even with our larger horizontal shear term than PC, we get more contribution from the vertical shear term than the PC study shows. Also our vertical shear reaches farther down than that of PC which deepens our negative potential vorticity region below 500 mb, lower than that of PC. As talked about in Section 4.2, if we try to increase the vertical shear term, it will still go statically unstable in the two areas mentioned earlier in this chapter. So the vertical shear contribution cannot approach the size of the horizontal shear term as far as causing inertial instability.

Initializing the model using white noise we note from Fig. 4.11 that the most unstable mode starts to dominate after 60,000 seconds. Once again the growth rate curve, Fig. 4.12a resembles that of a small equivalent depth case, since the σ_i are relatively constant through small s and decrease with larger s. The values of the growth rates are comparable to SC and what we found in Section 4.1. The phase speed plot Fig. 4.12b shows a steady increase as s increases which follow that of SC. These growth rates give us an e-folding time of around 3.5 - 5 hours. This compares to PC where they found the wavelets grew and decayed in a time frame of 4 - 5 hours.

Figures 4.13a through 4.13e show the perturbation variables at t = 100,000 seconds, well after the most unstable mode has taken over. We see in Fig. 4.13a, the values of u'. It develops within the unstable region with two main maxima, one located where the $(-f\bar{P})$ has its maxima and the other located in the upper region of $(-f\bar{P})$. The lower maximum is slightly offset from the upper one, this is due to the influence of the vertical shear term on the unstable region. The smaller maximum above the two large maxima is also offset to the north probably for the same reason. The v' response follows a similar pattern except for its broader horizontal scale, the same as in Section 4.1. The structure of T' has two maxima in the horizontal direction corresponding to u' and v' maxima yet it shows more vertical structure. And w' follows suit with two large maxima, the one at 44° forming a diagonal maximum to the lower south. Finally, ϕ' still has large values outside of the $(-f\bar{P})$ region but its largest values are within the unstable area. The overall structure of the response seems to follow that shown in Section 4.1, except now the maxima have a

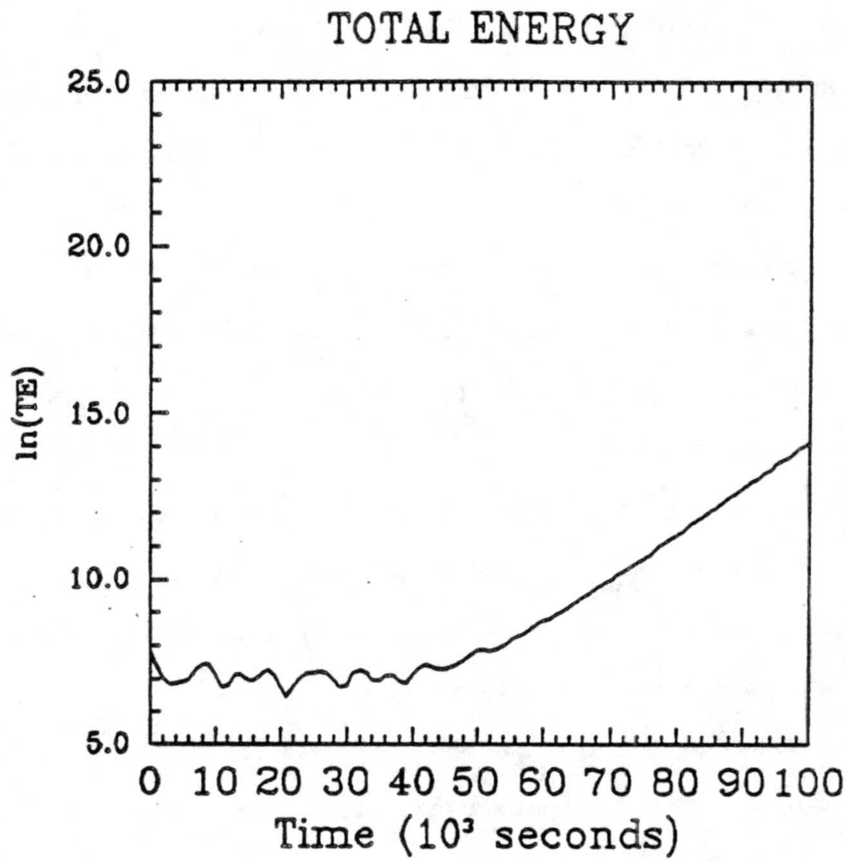

Figure 4.11: Same as Fig. 4.2 except for jet profile in Fig. 4.9a and $s = 6$.

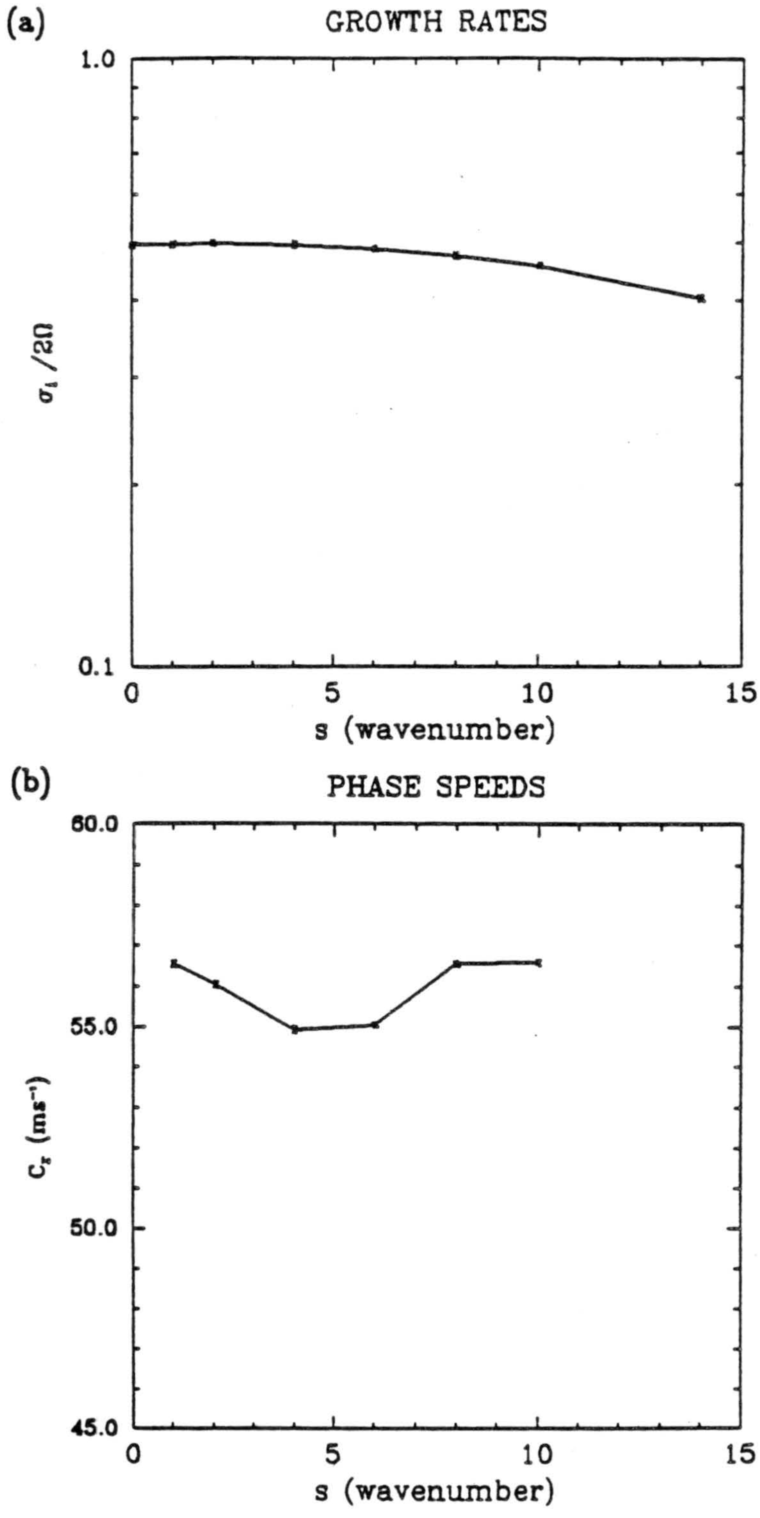

Figure 4.12: (a) Growth rates (σ_i) versus wavenumber (s). Same as Fig. 2.3a except for jet profile in Fig. 4.9a. (b) Phase speeds (c_r in ms^{-1}) versus wavenumber (s). Same as Fig. 2.3b except for jet profile in Fig. 4.9a.

(a)

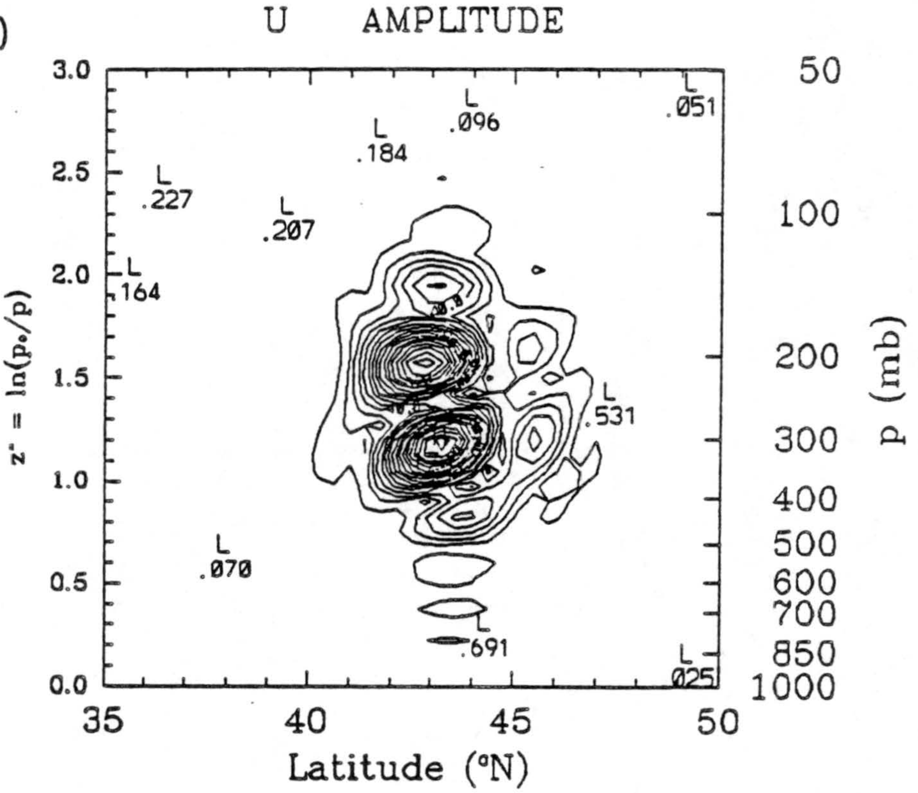

Figure 4.13: (a) Amplitude of u' (in ms^{-1}) at t = 100,000 seconds for jet profile in Fig. 4.9a and s = 6. Contour interval of 10.

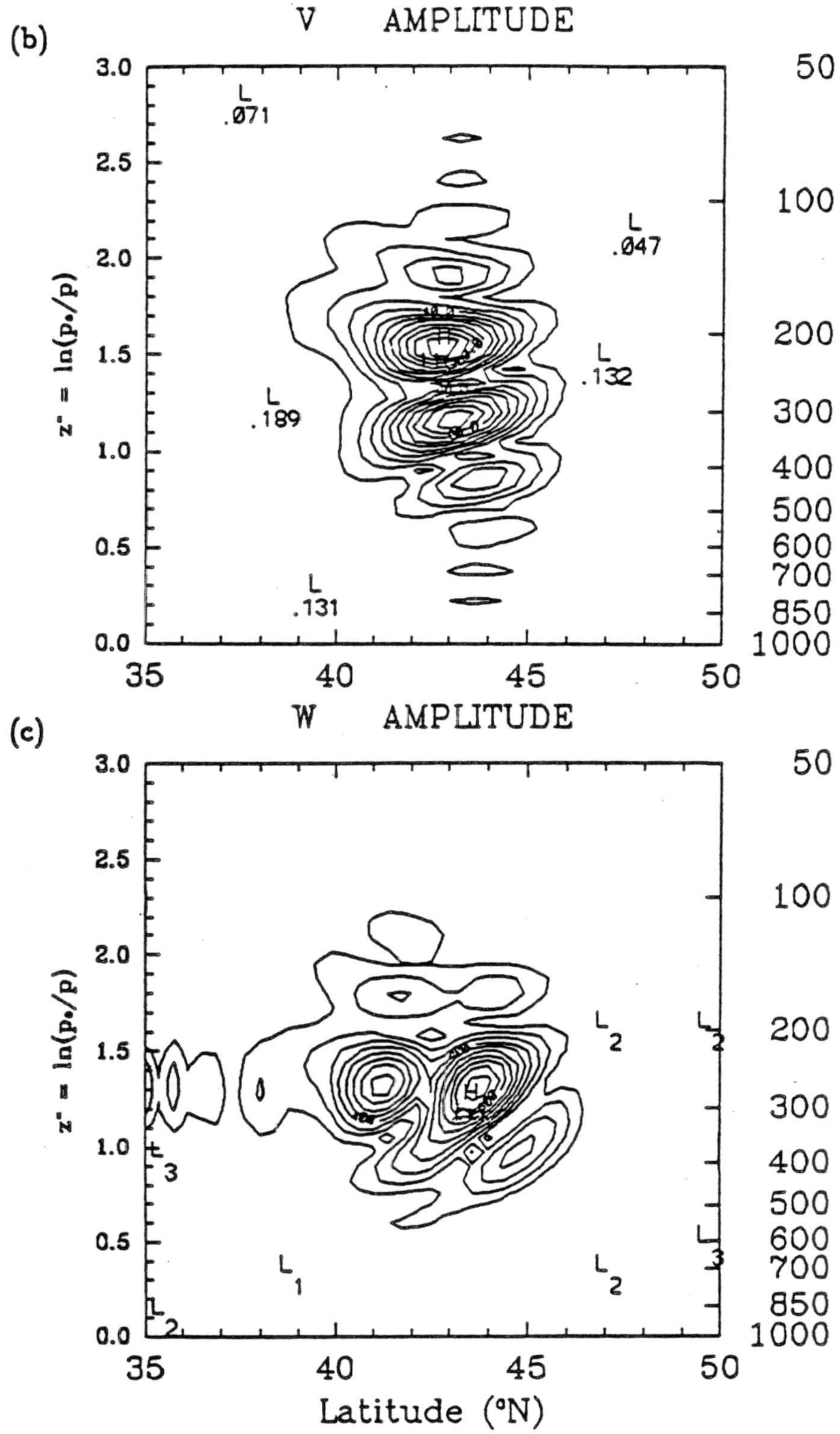

Figure 4.13: (b) Same as Fig. 4.13a except for v' (in ms^{-1}). Contour interval of 10. (c) Same as Fig. 4.13a except for w' (in s^{-1}). Contour interval of 0.1×10^{-4}. Labels scaled by 0.1×10^{8}.

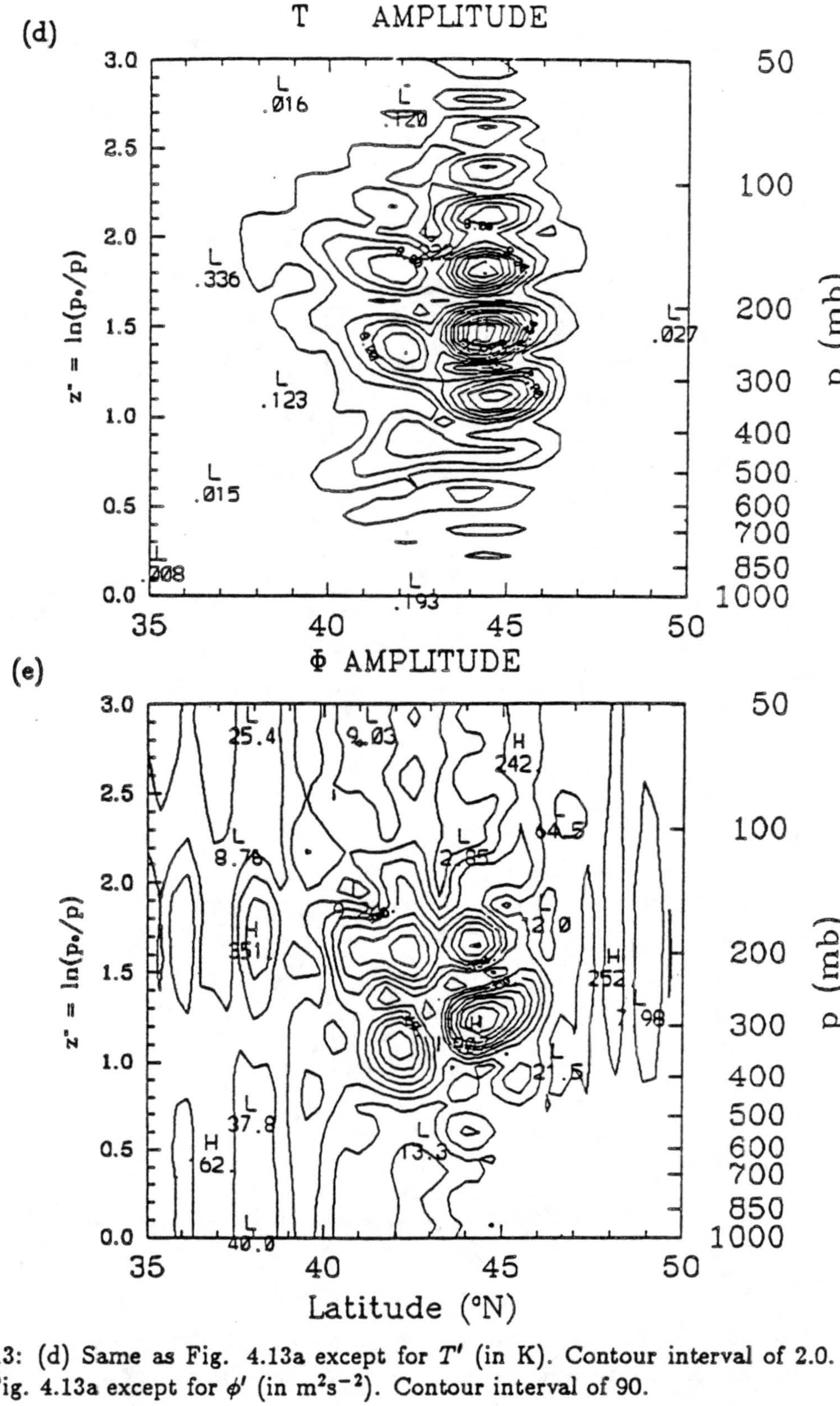

Figure 4.13: (d) Same as Fig. 4.13a except for T' (in K). Contour interval of 2.0. (e) Same as Fig. 4.13a except for ϕ' (in m^2s^{-2}). Contour interval of 90.

greater vertical scale yet are confined vertically, and the tilt in the lower portion due to the effects of vertical shear.

Chapter 5

SUMMARY AND CONCLUSIONS

In this paper we have studied the effects of various wind shears on perturbation growths within inertially unstable regions. This kind of study is meant to shed some light on the contrasting ideas surrounding what type of instability is preferred, symmetric or asymmetric. A necessary condition for inertial instability is when the basic state potential vorticity, $f\bar{P} < 0$. The potential vorticity can be divided into two parts, the part due to the horizontal shear and the part due to the vertical shear. With this in mind, we examine the relationships between the shears and the concept of symmetric versus asymmetric.

We have accomplished several things in this paper. First we developed a shallow water equation model utilizing time integration and the spectral method. We verified the results of SC with this model where asymmetric modes have larger growth rates than symmetric modes in a 1-D jet with only horizontal wind shear. In order to study inertial instability for jets with variable horizontal and vertical wind shear, we built from the shallow water model a primitive equation model containing two-dimensions y and z^*. After the model development, we ran a test case without the basic state jet and inserted an analytic heating function where we could discern the expected results. We found that with the lower boundary condition (the actual vertical velocity, $W = 0$) we considered, the external mode we resolved explicitly in our system; and since we are not interested in this mode we found we could ignore this mode by carefully choosing our time step.

Our model has been written, using the spectral method, so we can employ different boundary conditions to simulate various situations such as topography or a radiation condition. Also with this model we have "semi-nonlinear " terms already in the model which allows us the ability to generalize it to a full-spectral non-linear model with wave-mean flow interactions.

Three different cases with two-dimensional jets were examined. When the jet contained only horizontal shear the results matched those of the shallow water results. For the jet case with only vertical wind shear, we found a close relationship between vertical shear and static instability. When the static stability function is set up to contain horizontal variability along with the basic vertical stratification, an increase in the vertical shear causes the Brunt Väisälä frequency to become very small. This in turn causes the vertical shear term in the potential vorticity to become very large, statically unstable. We set the basic state temperature to be only a function of z^* in the static stability term and found the growth rates to be much less than those due to horizontal shear and the horizontal scale of the disturbances to be quite large. Finally we looked at a jet with both horizontal and vertical variable wind shear. Here we found the interaction of the two shears allows the vertical shear term to have more influence yet the horizontal shear term is still the dominant part. We found the perturbation to grow in the unstable region as expected with a structure similar to the horizontal shear case along with some influence from the vertical shear, a tilt in the lower maximum and larger vertical scale of the maxima.

Stone (1966) went about finding a range of conditions under which symmetric instabities have the largest growth rates. But in the process, he made assumptions which were critical in his results. First, he had no dissipation within the model. Dissipation acts as a stabilizing factor for symmetric modes of smallest vertical scale. Our model contains a vertical dissipation so as to stablize the smallest vertical scale modes. Second, only a constant vertical wind shear was considered in his basic state. We have found that horizontal wind shear is more effective than vertical shear for causing inertially unstable conditions. In our cases with $\bar{u}(y, z^*)$, we have found the equivalent depth to be small thus larger wavenumbers show a decrease in the growth rates. Yet the relatively constant growth rates over the smallest wavenumbers tell us that assuming inertial instability as strictly symmetric is not correct since asymmetric modes have as large an influence. Thus in all the cases we examined, we found that the preferred instability is in the asymmetric modes.

REFERENCES

Boyd, J.P., and Z.D. Christidis, 1982: Low wavenumber instability on the equatorial beta-plane. *Geophys. Res. Lett.*, 769-772.

Charney, J.G., 1973: Planetary fluid dynamics. Dynamic Meteorology, P. Morel, Ed., D. Reidel, 622pp.

Charney, J.G., and M.E. Stern, 1962: On the stability of internal baroclinc jets in a rotating atmosphere. *J. Atmos. Sci.*, **19**, 159-264.

Ciesielski, P.E., Stevens, D.E., Johnson, R.H., and Dean, K.R., 1988: Observational evidence for asymmetric inertial instability. J.Atmos. Sci. (submitted).

Conte, S.D., 1965: Elementary Numerical Analysis. McGraw-Hill, p. 223.

Dunkerton, T.J., 1981: On the inertial stability of the equatorial middle atmosphere. *J. Atmos. Sci.*, **38**, 2354-2365.

Dunkerton, T.J.,1982: Curvature diminution in equatorial wave, mean-flow interaction. *J. Atmos. Sci.*, **39**, 182-186.

Dunkerton, T.J.,1983: A nonsymmetric equatorial inertial instability. *J. Atmos. Sci.*, **40**, 807-813.

Eady, E.T., 1949: Long waves and cyclonic waves. *Tellus*, **1**, 33-52.

Eliassen, A., 1983: The Charney-Stern theorem on barotropic-baroclinc instability. *Pageoph*, **121**, 562-572.

Emanuel, K.A., 1979: Inertial instability and mesoscale convective systems. Part I: Linear theory of inertial instability in rotating viscous fluids. *J. Atmos. Sci.*, **36**, 2425-2499.

Emanuel, K.A., 1982: Inertial instability and mesoscale convective sy;stems. Part II: Symmetric CISK in a baroclinic flow. *J. Atmos. Sci.*, **39**,1080-1097.

Emanuel, K.A., 1983: Symmetric instability. Mesoscale Meteorology- Theories, Observations, and Models, 217-229. D. Reidel Publishing Company .

Fulton, S.R., 1984: Spectral methods for limited area models. Ph.D. dissertation, Colorado State University, 149 pp.

Fulton, S.R., and Schubert, W.H., 1985: Vertical normal mode transforms: theory and application. *Mon. Wea. Rev.*, **113**, 647-658.

Haltiner, G.J., and R.T. Williams, 1980: Numerical Prediction and Dynamic Meteorology. John Wiley and Sons, 477 pp.

Holton, J.R., 1979: An Introduction to Dynamic Meteorology, second edition. Academic Press, 391 pp.

Mass, C., 1979: A linear primitive equation model of African wave disturbances. *J. Atmos. Sci.*, **36**, 2075-2092.

Nehrkorn, T., 1986: Wave-CISK in a baroclinic basic State. *J. Atmos. Sci.*, **43**, 2773-2791.

Stevens, D.E., 1983: On symmetric stability and instability of zonal mean flows near the equator. *J. Atmos. Sci.*, **40**, 882-893.

Stevens, D.E., and Ciesielski, P.E., 1986: Inertial instability of horizontally sheared flow away from the equator. *J. Atmos. Sci.*, **43**, 2845-2856.

Stevens, D.E., and Crum, F.X., 1987: Dynamic Meteorology. Encycl. Phy. Sci. and Tech., **8**, 227-260. Academic Press.

Stone, P.H., 1966: On non-geostrophic baroclinic stability. *J. Atmos. Sci.*, **23**, 390-400.

Stone, P.H., 1970: On non-geostrophic baroclinic stability. Part II. *J. Atmos. Sci.*, **27**, 721-726.

United States Standard Atmospheric Supplements, 1966: Superintendent of Documents, U.S. Government Printing Office, Washington, D.C. 20402 (289 pp.)

Young, J.A., 1968: Comparative properties of some time differencing schemes for linear and nonlinear oscillations. *Mon. Wea. Rev.*, **96**, 357-364.

APPENDIX A

Chebyshev Polynomials

Spectral discretizations can provide highly accurate approximations with far fewer degrees of freedom then required by finite difference methods. Chebyshev polynomials are usually preferred basis functions since they give somewhat better approximations for the same number of terms compared to other polynomials. Chebyshev series converge faster and can be evaluated very efficiently using the Fast Fourier Transform (FFT) algorithm (Fulton, 1984).

Chebyshev polynomials, $T_n(x)$ are defined on the interval $-1 \leq x \leq 1$ by

$$T_n(\cos\theta) = \cos(n\theta) \qquad (A.1)$$

where $x = \cos\theta$. From (A.1) we have $T_o(x) = 1$ and $T_1(x) = x$, and the trigonometric identity $\cos(n\theta) = 2\cos\theta\cos[(n-1)\theta] - \cos[(n-2)\theta]$ yields the recurrence relation

$$T_n(x) = 2xT_{n-1}(x) - T_{n-2}(x) \qquad (A.2)$$

The extrema of $T_n(x)$ all have absolute value 1. From (A.1), the zeros of $T_n(x)$ occur at

$$\tilde{x}_j^{(n)} = \cos[(j+1/2)\frac{\pi}{n}] \quad (j = 0, \ldots, n-1) \qquad (A.3)$$

and the extreme at

$$\bar{x}_j^{(n)} = \cos\left(\frac{j\pi}{n}\right) \quad (j = 0, \ldots, n) \qquad (A.4)$$

with $T_n(\bar{x}_j^{(n)}) = (-1)^j$. In particular, $T_n(1) = 1$ and $T_n(-1) = (-1)^n$ for $n = 0, 1, 2, \ldots$

The Chebyshev polynomials are orthogonal (but not normalized) in the Chebyshev inner product

$$\langle f, g\rangle = \int_{-1}^{1} \frac{f(x)g(x)}{(1-x^2)^{\frac{1}{2}}}dx \tag{A.5}$$

with

$$\langle T_m, T_n\rangle = \frac{\pi}{2}c_n\delta_{mn}, \quad c_n = \{2 \quad n=0; 1 \quad n>0\} \tag{A.6}$$

Thus the coefficients in the Chebyshev series

$$u(x) = \sum_{n=0}^{\infty} \hat{u}_n T_n(x) \tag{A.7a}$$

are

$$\hat{u}_n = \frac{2}{\pi c_n}\langle u, T_n\rangle \tag{A.7b}$$

Equations (A.7) constitute the continuous Chebyshev transform pair.

For the truncated series

$$u_N(x) = \sum_{n=0}^{N} \hat{u}_n T_n(x) \tag{A.8}$$

the transform pair (A.7) has the discrete analogue

$$\bar{u}_j = \sum_{n=0}^{N} \hat{u}_n T_n(\bar{x}_j) \tag{A.9a}$$

$$\hat{u}_n = \frac{2}{N\bar{c}_n}\sum_{j=0}^{N} \frac{1}{\bar{c}_j}\bar{u}_j T_n(\bar{x}_j) \tag{A.9b}$$

Here $\bar{x}_j = \bar{x}_j^{(N)} (j = 0, \ldots, N)$ are the points at which $T_N(x)$ has extrema, $\bar{u}_j = \bar{u}_N(x_j)$, and $\bar{c}_n = 2$ for $n = 0$ and $n = N$ and 1 otherwise.

Many common operations on functions represented by Chebyshev series can be calculated easily in terms of the spectral coefficients. For example, if $u(x)$ is given by (A.7a) then the derivative is

$$u'(x) = \sum_{n=0}^{\infty} \hat{u}_n^{(1)} T_n'(x) \tag{A.10}$$

where

$$\hat{u}_n^{(1)} = \frac{2}{c_n} \sum_{m=n+1}^{\infty} m\hat{u}_m, \quad m+n \text{ odd} \tag{A.11}$$

Similarly,

$$xu'(x) = -\sum_{n=0}^{\infty} [n\hat{u}_n + \hat{u}_n^{(1,x)}] T_n(x) \tag{A.12}$$

where

$$\hat{u}_n^{(1,x)} = \frac{2}{c_n} \sum_{m=n+2}^{N} m\hat{u}_m, \quad m+n \text{ even} \tag{A.13}$$

For the truncated series (A.8), (A.11) and (A.13) yield the recurrence formula

$$c_{n-1}\hat{u}_{n-1}^{(1)} - \hat{u}_{n+1}^{(1)} = 2n\hat{u}_n \tag{A.14}$$

and

$$c_{n-1}\hat{u}_{n-1}^{(1,x)} - \hat{u}_{n+1}^{(1,x)} = 2(n+1)\hat{u}_{n+1} \tag{A.15}$$

for $n = 1, \ldots, N-1$ with the starting values $\hat{u}_{N+1}^{(1)} = \hat{u}_N^{(1)} = \hat{u}_{N+1}^{(1,x)} = \hat{u}_N^{(1,x)} = 0$. Thus the spectral coefficients for $u_N'(x)$ and $xu_N'(x)$ may be obtained from those for $u_N(x)$.

APPENDIX B

Flow Charts of the Fortran-coded Algorithms

This appendix provides flow charts of the computer code needed to run the primitive equation model described in Section 3 of this paper. The flow charts shown on the following pages describe in respective order:

1. a main program which contains the Runge-Kutta fourth order time integration scheme,
2. the initialization of the model variables and parameters,
3. the computation of w' and ϕ' from the diagnostic equations,
4. the computation of the right-hand side of the prognostic equations,
5. the computation of u', v' and T' which involves the time integration of the prognostic equations.

Primitive Equation Model

Note: Dependent variable subscripts:
p - physical space volumes
s - spectral space coefficients
$\mathbf{u}_p^{(n)} = \left(u_p^{(n)}, v_p^{(n)}, T_p^{(n)}, w_p^{(n)}, \phi_p^{(n)}\right)$
The primes have been dropped from the perturbation variables
ITIME = time increment counter
ITO = time increment interval for data
ITMAX = total number of time increments

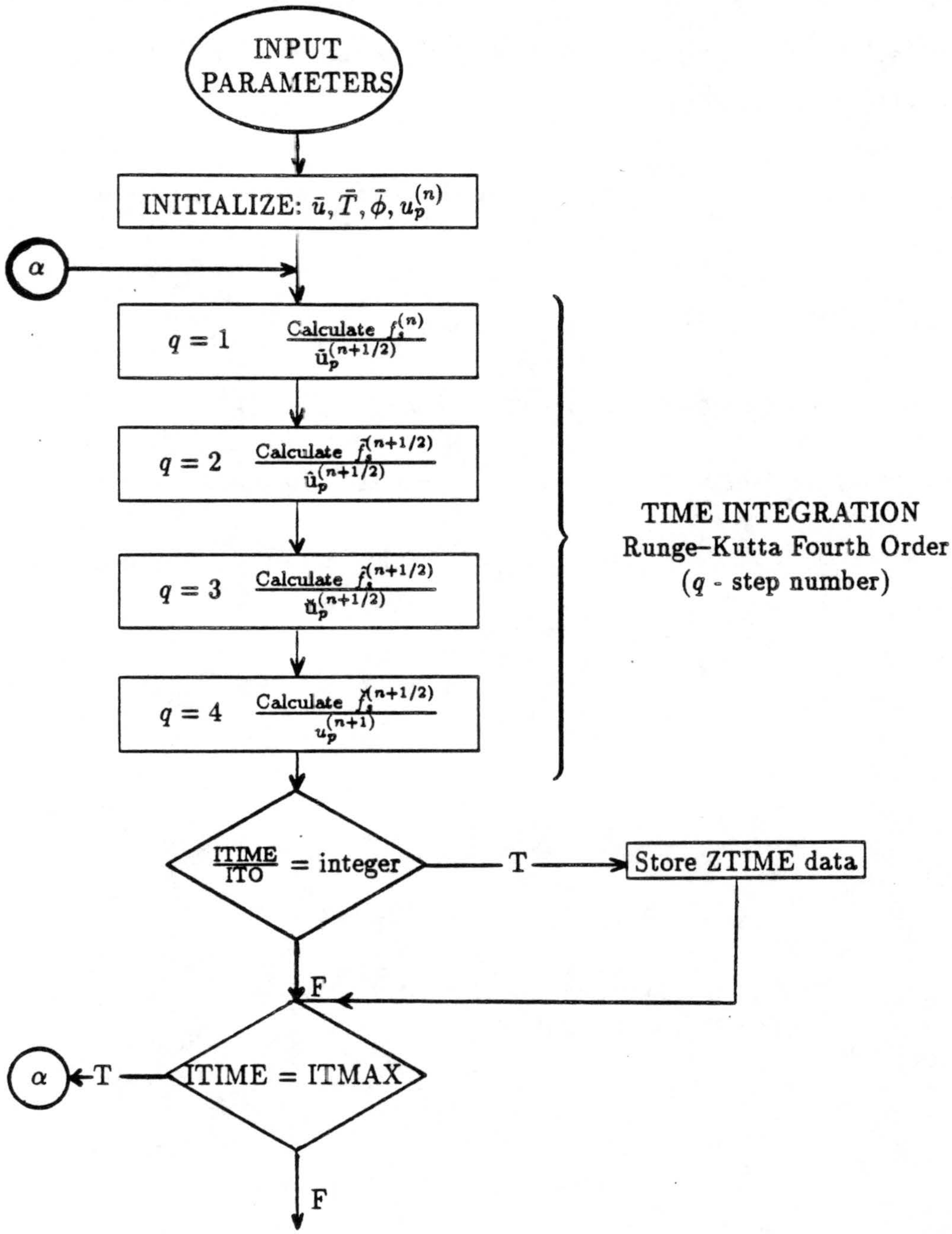

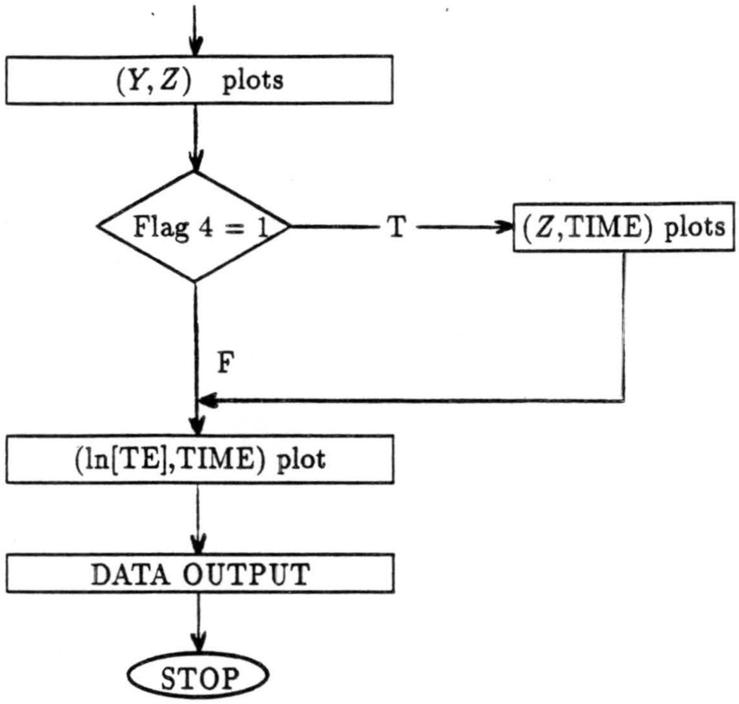
(Y, Z) plots
Flag 4 = 1
T
(Z,TIME) plots
F
(ln[TE],TIME) plot
DATA OUTPUT
STOP

Initialization

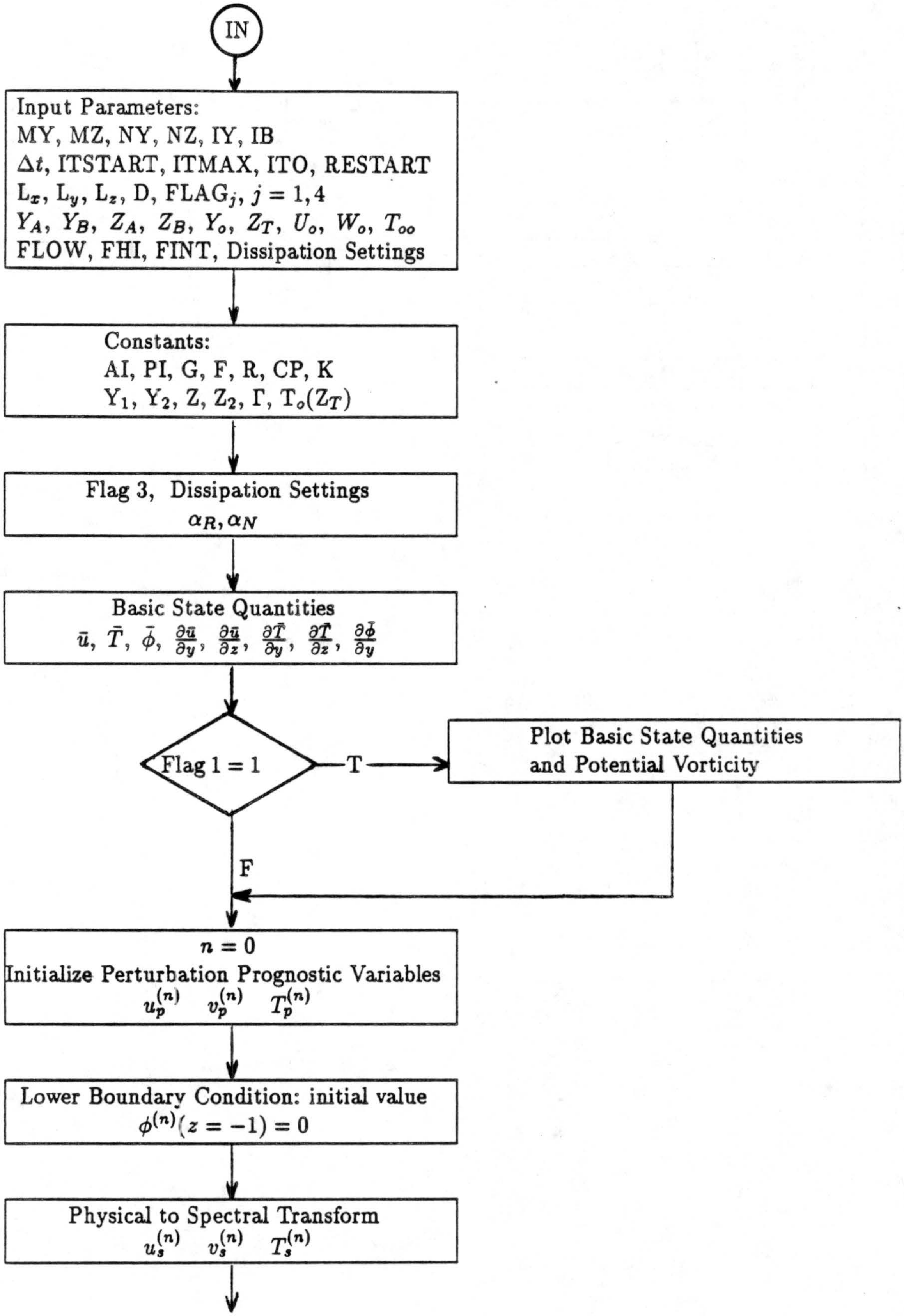

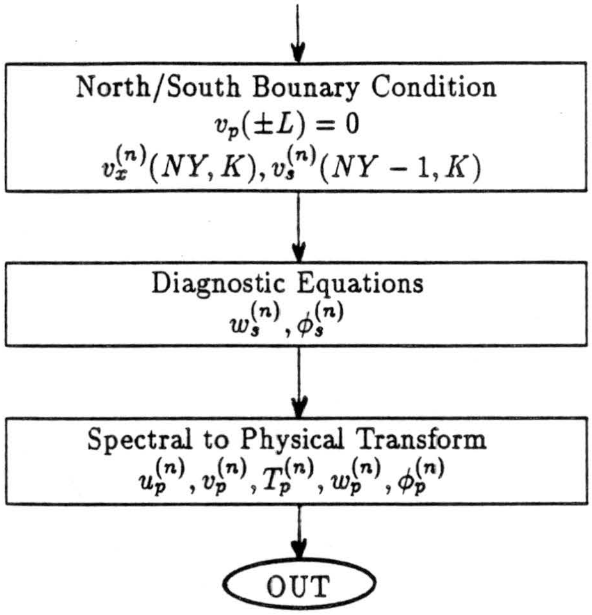
North/South Bounary Condition
$v_p(\pm L) = 0$
$v_x^{(n)}(NY, K), v_s^{(n)}(NY - 1, K)$
Diagnostic Equations
$w_s^{(n)}, \phi_s^{(n)}$
Spectral to Physical Transform
$u_p^{(n)}, v_p^{(n)}, T_p^{(n)}, w_p^{(n)}, \phi_p^{(n)}$
OUT

Diagnostic Equations

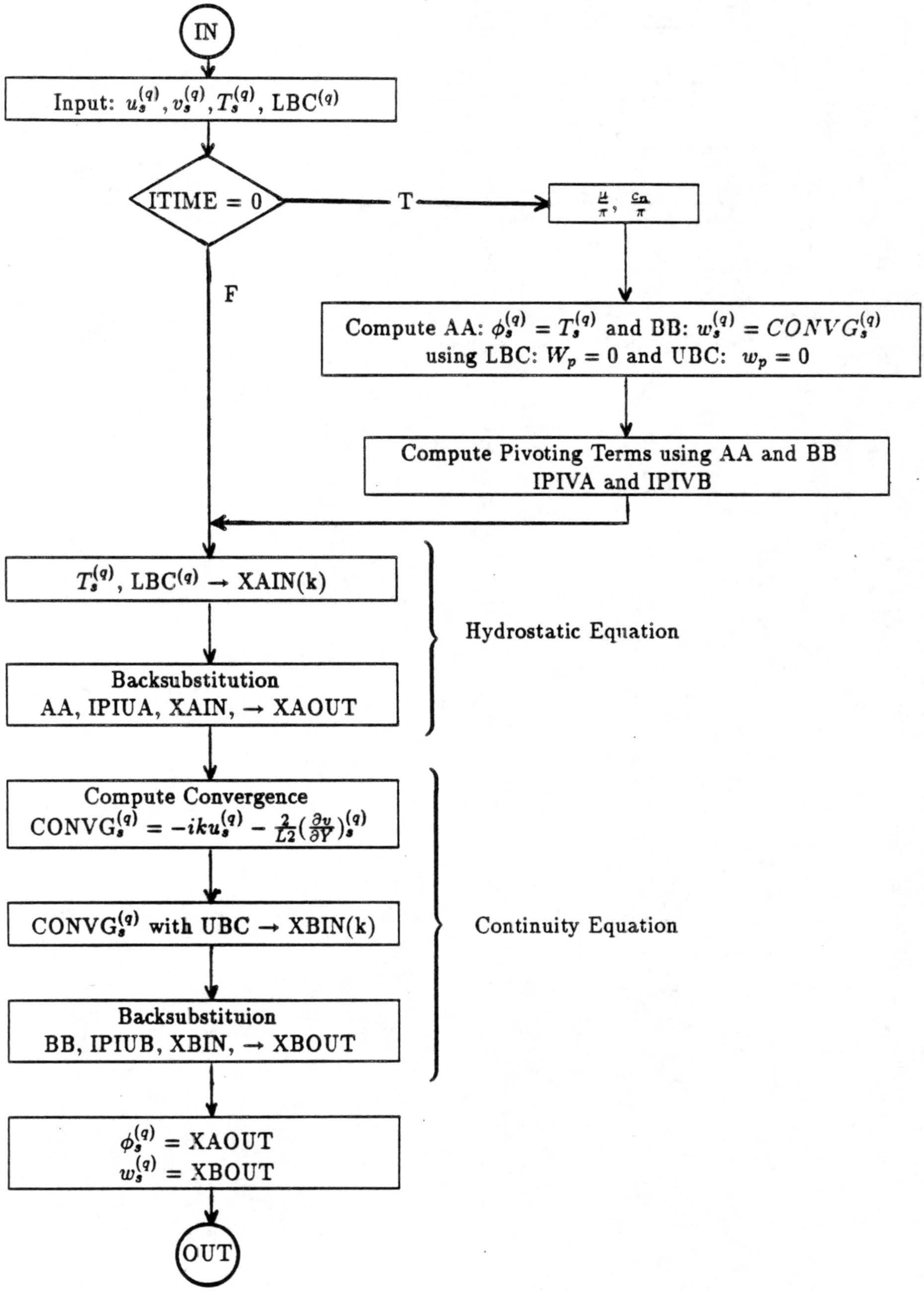

Right Hand Side of Prognostic Equation

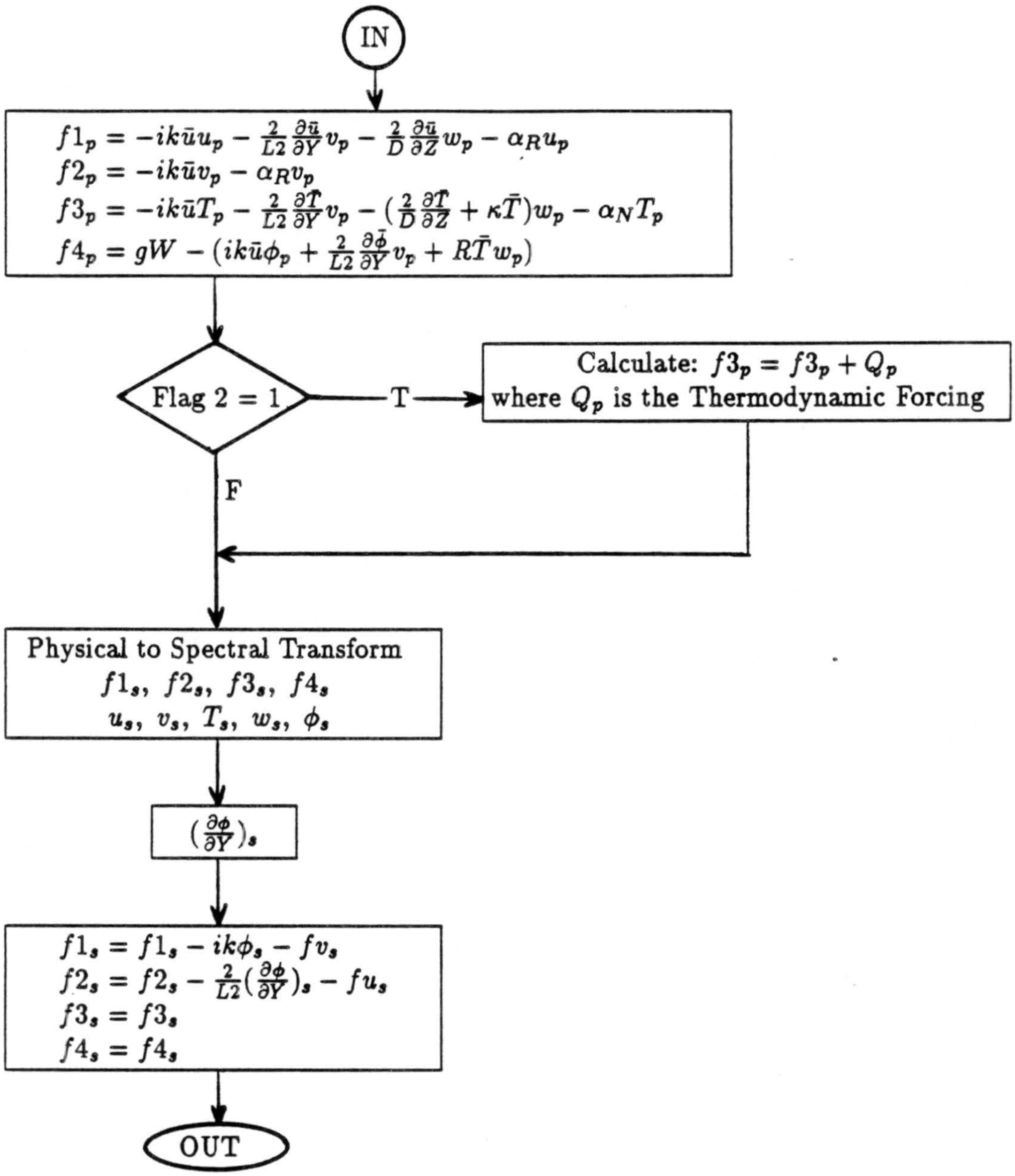

Time Integration

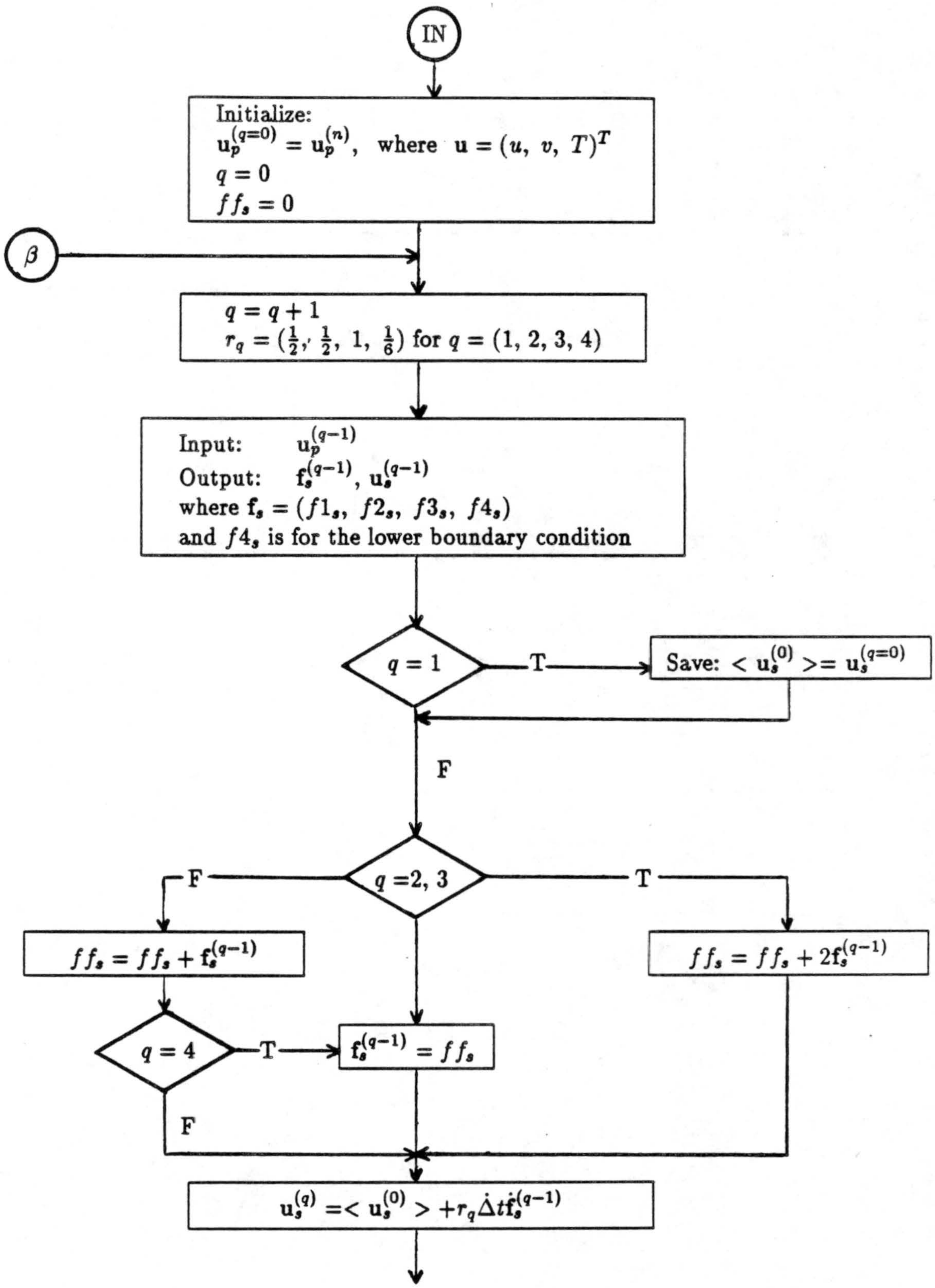

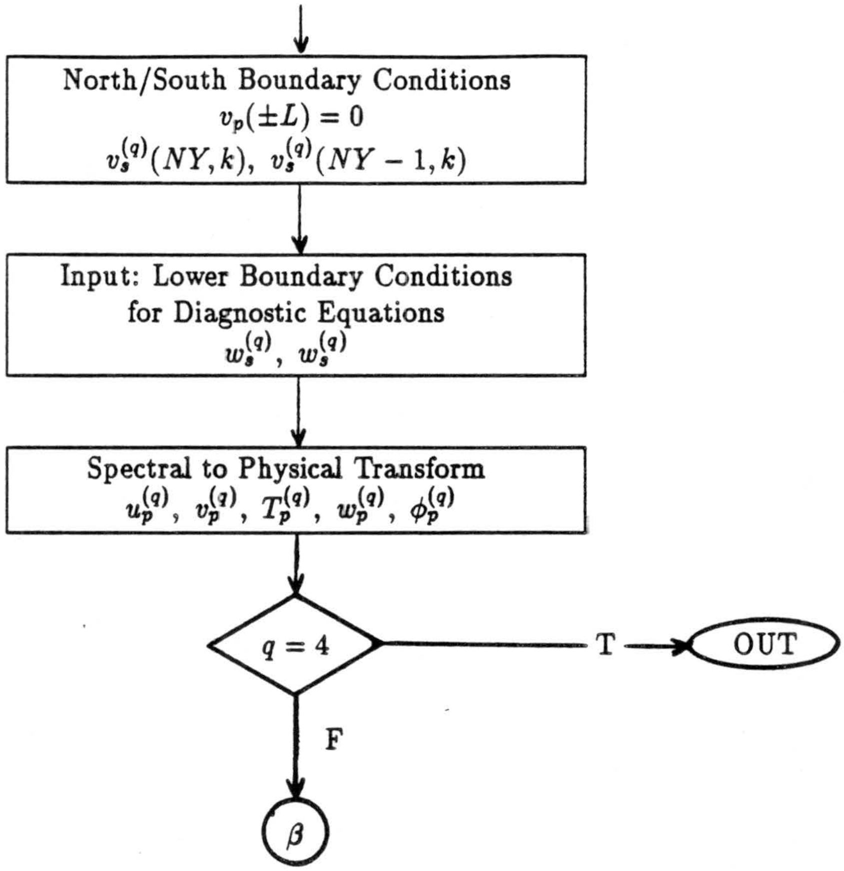
North/South Boundary Conditions
$v_p(\pm L) = 0$
$v_s^{(q)}(NY, k),\ v_s^{(q)}(NY-1, k)$
Input: Lower Boundary Conditions
for Diagnostic Equations
$w_s^{(q)},\ w_s^{(q)}$
Spectral to Physical Transform
$u_p^{(q)},\ v_p^{(q)},\ T_p^{(q)},\ w_p^{(q)},\ \phi_p^{(q)}$
$q = 4$
T
OUT
F
β

951163 EM